CAPACITY AND POWER FADE IN LITHIUM-ION BATTERIES

A Dissertation
Presented to
The Academic Faculty

by

Tapesh Joshi

In Partial Fulfillment
of the Requirements for the Degree
Doctor of Philosophy in the
School of Chemical & Biomolecular Engineering

Georgia Institute of Technology
May 2016

CAPACITY AND POWER FADE IN LITHIUM-ION BATTERIES

Approved by:

Dr. Thomas F. Fuller, Advisor
School of Chemical & Biomolecular
Engineering
Georgia Institute of Technology

Dr. Paul A. Kohl
School of Chemical & Biomolecular
Engineering
Georgia Institute of Technology

Dr. Martha Grover
School of Chemical & Biomolecular
Engineering
Georgia Institute of Technology

Dr. Gleb Yushin, Co-advisor
School of Materials Science &
Engineering
Georgia Institute of Technology

Dr. Dennis W. Hess
School of Materials Science &
Engineering
Georgia Institute of Technology

Date Approved: January 13, 2016

ACKNOWLEDGEMENTS

TABLE OF CONTENTS

LIST OF TABLES

LIST OF FIGURES

LIST OF ABBREVIATIONS

CB	Carbon black
CC	Constant current
CC-CV	Constant current-constant voltage protocol
DEC	Diethyl carbonate
DMC	Dimethyl carbonate
DOE	Department of energy
EC	Ethylene carbonate
EIS	Electrochemical impedance spectroscopy
EOC	End of charge
EOD	End of discharge
EV	Electric vehicle
FIB	Focused ion beam
FWHM	Full-width-half-max
GHG	Greenhouse gas
HEV	Hybrid electric vehicle
HPPC	Hybrid pulse power characterization
HR-SEM	High resolution scanning electron microscopy
LTO	Lithium titanium oxide
NCM	Nickel cobalt manganese (LiNiaCobMncO2) electrode
NMP	N-methyl-2-pyrrolidinone
OCV	Open-circuit voltage
PEO	Plolyethylene oxide
PHEV	Plug-in hybrid vehicle

PVDF	Polyvinylidene fluoride
SEI	Solid electrolyte interphase
SOC	State-of-charge
TEM	Transmission electron microscopy
TOF-SIMS	Time of flight secondary ion mass spectroscopy
VC	vinylene carbonate
XPS	X-ray photoelectron spectroscopy

LIST OF SYMBOLS

a	specific surface area of the porous electrode, m^2/m^3
c	lithium concentration in solution phase, mol/ m^3
c_s	lithium concentration in the solid phase, mol/m^3
C_s	specific capacity of the electrode, mAh/g
c_S	concentration of solvent in the SEI, mol/m^3
c_{max}	maximum Li concentration inside the active material, mol/m^3
D	lithium diffusion coefficient in the solution phase, m^2/s
D_{eff}	effective lithium diffusion coefficient in the solution phase, m^2/s
D_s	lithium diffusion coefficient inside the active material, m^2/s
D_{sol}	solvent diffusivity inside the SEI, m^2/s
F	Faraday's constant, 96487 C/mol
i_{int}	intercalation current density, A/m^2
i_s	side reaction current density, A/m^2
I	total current density, A/m^2
j_n	pore-wall flux of lithium ions, $mol/(m^2s)$
k	rate constant for intercalation reaction, $mol/(m^2s(mol/m^3)^{1.5})$
M	molecular weight, kg/mol
n	number of moles of lithium ions
$n_{Li,p}$	number of moles of lithium in the positive electrode
P	product of side reaction
r	radial distance from the center of the particle, m
R_s	particle radius, m
R_{SEI}	resistance of the SEI, $\Omega.m^2$

S	solvent
U	equilibrium potential for intercalation reaction, V
V_{max}	maximum charging potential of the battery, 4.2 V
V_{min}	minimum discharge potential of the battery, 2.4 V
V_{OCV}	Open-circuit voltage of the cell, V
x	distance from the end of the negative electrode, m
x	dimensionless Li concentration in the negative electrode
y	dimensionless Li concentration in the negative electrode
ε	volume fraction
α_a	anodic charge transfer coefficient
α_c	cathodic charge transfer coefficient
δ	SEI thickness, m
η	overpotential for intercalation reaction, V
κ	conductivity in the electrolyte phase, S/m
ρ	density, kg/m^3
σ	conductivity in the solid phase, S/m
Φ_1	potential of solid phase, V
Φ_2	potential of solution phase, V

Subscripts/superscripts

1	solid phase
2	solution phase
c	charge
d	discharge
n	negative electrode

p	positive electrode
SEI	solid electrolyte interphase
in	inner SEI layer
out	outer SEI layer
tot	total lithium in the cell

SUMMARY

Lithium-ion batteries are known to have performance degradation as repeated use and age of the batteries increase. It is essential to qualify these batteries to meet the performance goals for their intended applications. For batteries requiring long-term use, such as transportation applications in electrified vehicles, experimental testing for extended periods is generally not viable due to high costs associated with long-term testing. To minimize qualification times, accelerated experimental testing and mathematical modeling can be combined to elucidate long-term battery performance.

In this work, we have investigated the long-term performance of lithium-ion batteries using both accelerated experimental tests and supported observed degradation phenomena through mathematical modeling. Experimentally, electrode degradation was accelerated to quantify performance losses. To understand the effects of transition metal dissolution in full cells, accelerated testing was accomplished by introducing transition metal salts in the electrolyte. We found that the dissolution of transition metals cause a reduction in cell capacity and cycle stability in full cells. Reduction of transition metal species in the negative electrode facilitated the growth of the solid electrolyte interphase (SEI) by increasing the rate of solvent diffusion through the SEI and the subsequent reduction of the solvent.

Performance losses occurring in commercial cells for high power applications were studied by accelerating degradation via high temperature aging. Cell components were tested by using electrochemical and post-mortem analysis techniques to elucidate the

mechanisms for capacity fade and cell resistance increase. Capacity and power fading phenomenon in these cells were found to occur in two stages that were caused by: (i) lithium loss in the SEI in the negative electrode and (ii) active material dissolution and surface layer growth on the positive electrode.

A model was developed to simulate and predict performance of a typical lithium-ion battery used in a hybrid electric vehicle. Discharge simulation results on batteries consisting of a nickel cobalt manganese (NCM) positive electrode and a graphite negative electrode showed good agreement with experimental data. Losses in cell capacity and power due to lithium loss in the SEI were determined using the model. Cyclable lithium loss in the SEI was found to contribute significantly to the power capability loss and cell resistance increase. Capacity fade occurring in commercial cells via lithium loss mechanism was elucidated by combining experimental and modeling results.

CHAPTER 1

INTRODUCTION

The transportation industry is one of the largest contributors to greenhouse gas (GHG) emissions. Dependence on fossil fuels for powering vehicles has been a critical factor for significant increases in global temperatures and air pollution. As shown in Figure 1.1, the transportation sector contributed to over a quarter of GHG emissions in 2013 in the U.S. [1]. Petroleum based fuels, such as gasoline and diesel, account for over 90 % of the fuels used in transportation [1]. GHG emissions from the transportation sector can be reduced by limiting reliance on petroleum based fuels and looking for cleaner alternative sources.
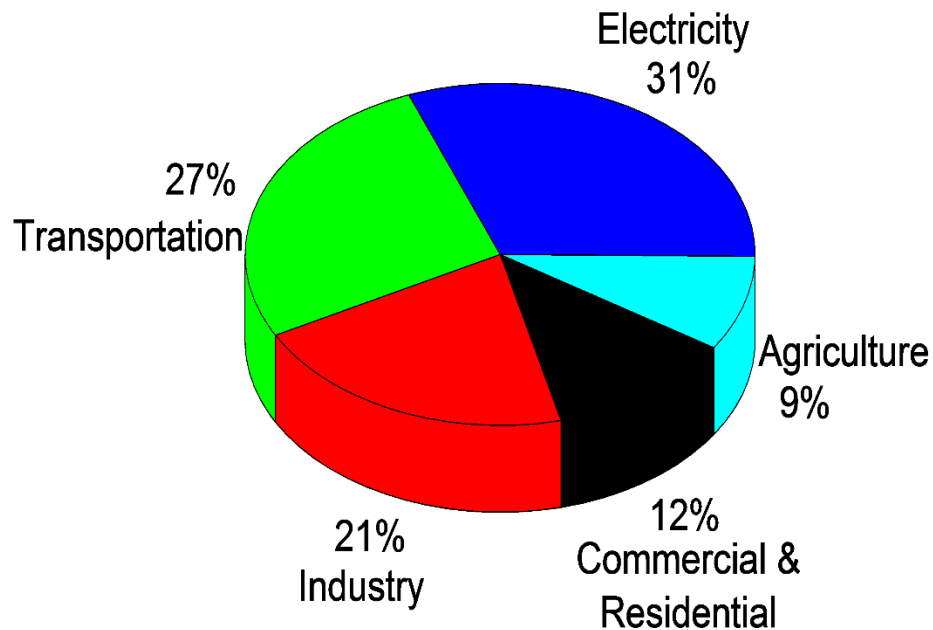
Figure 1-1. U.S. Greenhouse Gas Emissions by Economic Sector in 2013 [1].

Electric and hybrid electric vehicles are becoming increasingly popular because they are environmentally friendly as well as energy and fuel efficient compared to fossil fuel powered vehicles. Pollution due to tailpipe emissions of criteria pollutants occurring in vehicles using conventional petroleum based fuels can be controlled by vehicle electrification. Lithium-ion batteries are being used in more and more hybrid electric vehicles (HEV), plug-in hybrid vehicles (PHEV), and fully electric vehicles (EV) for electric powertrains. The adoption of lithium-ion batteries for transportation applications has been increasing and is expected to continue to grow. According to an estimate by the metal and minerals market research firm Roskill, total sales of lithium battery vehicles worldwide is expected to be more than double compared to today's number and reach greater than four million units by year 2020 [2]. Sales share of electrified vehicles (HEV, PHEV, and EV) is expected to be above 6.5 % of total light duty vehicles in North America by 2022 increasing from current share of 4 % in 2015 [3]. With increasing adoption of lithium-ion batteries for transportation applications, demand for batteries is also on the rise. The Department of Energy (DOE) published a set of guidelines and requirements for lithium-ion batteries for transportation applications [4]. These requirements specify the required life of batteries as well as energy, power, and safety requirements. Newer and more advanced materials are constantly being developed in order to meet the demands of improved batteries to power next generation of electric vehicles. These materials require qualification to meet the performance requirements for their intended applications.

1.1 Motivation

Cell capacity and power are often used as parameters to describe cell performance. Cell capacity is a measure of the total electrical charge a cell is able to store. Capacity is expressed in ampere-hours, Ah. A fully charged battery with a capacity of one Ah (or 1000 mAh) can provide a total charge of 3600 coulombs by discharging it at a current of one ampere (A) for one hour. Cell power is a measure of how fast a cell can provide the stored energy and is reported in watts (W). The theoretical capacity and the equilibrium voltage of a cell depend on materials used for the cell. During operation (current flow), the voltage of a cell differs from the equilibrium voltage depending on current applied and internal resistance of the cell. When current is applied, cell capacity observed is less than theoretical capacity. Cell performance is determined by many competing effects, including materials used, mode of operation, and temperature among others. By understanding the influence of these factors on cell performance, design considerations can be made to improve cell performance. Every design consideration during cell fabrication has effect on long term performance of batteries. Understanding of cell degradation mechanisms under different modes of operation can help tremendously in designing a better battery aimed at achieving performance goals for specific applications.

1.1.1 Need for physical insight and improved predictive capability

Lithium-ion batteries are used in many applications ranging from medical implants to satellites. As such, the requirements of batteries vary greatly depending on each application. The performance of a battery is influenced by many design considerations that take into account the intended applications. Material advancements enable the development

of improved batteries to meet increasing demands and improved goals. As stated earlier, battery performance is dictated by a multitude of parameters. It is essential to understand how performance varies with regards to changing cell parameters and applications to meet the performance goals of the battery. Performance degradation in batteries is inevitable and the degradation mechanisms vary based on materials used, design considerations, and modes of operation of batteries.

It is often impractical to test batteries for the entire duration as intended for their future application. For example, batteries used in electric vehicles are expected to have a calendar life of 15 years [4]. It is impractical to require testing for the entire expected life of the batteries. Such testing is extremely expensive and becomes a bottleneck for introduction of new materials. Accelerated testing or tools to assess the long-term performance are needed. Accurate battery models can help in making predictions about the performance without relying solely on experiments. By combining the physical insights gained through experiments about different modes of degradation in batteries, better predictive models can be made. Insight about physical processes can be useful in designing cells for specific applications and for making better predictive models.

1.1.2 Approach

Experimental studies provide insight into physical processes that affect cell performance. Experiments can be designed to gain a qualitative as well as quantitative understanding of different cell parameters. Knowledge about cell parameters is valuable in making accurate models to simulate cell performance. Often, a specific mode of cell degradation, such as dissolution of active material from electrode and its effects on cell

performance, can be studied by using experimental techniques. A combined experimental and modeling study can help understand different cell processes that affect performance. By utilizing experimental and modeling techniques, degradation modes such as lithium loss in the surface layer of the negative electrode and its effects on cell capacity and power can be studied in detail.

In this work, a combined experimental and modeling technique was used to elucidate different cell degradation mechanisms and their effects on cell performance. Performance degradation results in lithium-ion batteries from repeated charging and discharging (cycling) as well as storage (aging) for a long period of time. Degradation processes are slow and occur over the lifetime of a cell. In addition, there are many competing effects that influence cell performance. We studied degradation due to dissolution of transition metals from the positive electrodes by replicating dissolution in degraded cells. This was achieved by adding dissolved transition metal salts in the electrolyte. Similarly, accelerated degradation in commercial cells was achieved by aging the cell at high temperature (75 °C). Electrochemical testing and analytical techniques were employed to isolate cell components and to understand different degradation mechanisms and their influence on cell performance. Modeling studies were completed to look at the role of the lithium loss in the surface layers formed on the negative electrode, commonly referred as solid electrolyte interphase (SEI) on cell performance degradation.

1.2 Scope of the work

The primary objective of this work is to understand degradation mechanisms that affect capacity and power in practical lithium-ion batteries used in transportation

applications. In this work, we focused on degradation mechanisms affecting cells employing mixed nickel cobalt manganese (NCM) positive electrodes and graphite negative electrodes. We used experimental and modeling techniques to understand and quantify different degradation mechanisms and their effects on cell capacity and power. Specific tasks completed and results accomplished in this work are described briefly below.

1.2.1 Understanding SEI growth

We used experimental and modeling techniques to study the SEI growth and its effects on cell performance. We fabricated and tested coin cells with NCM positive electrodes and graphite negative electrodes to better understand the nature of SEI formed on practical cells. Accelerated testing was done in lab-made coin cells and commercial cells and techniques including post-mortem analysis were used to study the SEI formed. Models developed earlier by Fuller *et al.* [5, 6] were extended to study the effects of lithium loss on the SEI on capacity and power fade. Results on our studies on the SEI are discussed in detail in **Chapters 4, 5,** and **6**.

1.2.2 Understanding degradation due to dissolution

Dissolution of transition metals is one of the major degradation mechanisms occurring in the positive electrode materials used in most commercial cells. Active material dissolution has been reported to occur in NCM electrodes. We designed experiments to accelerate the degradation caused via dissolution mechanism and studied the effects on cell performance and SEI growth. Commercial cells were also tested and electrochemical and post-mortem analyses were performed to understand dissolution and its effects. Results

discussing dissolution and performance degradation related to this are covered in **Chapters 4** and **5**.

1.2.3 Identifying degradation processes in commercial li-ion cells

Lithium-ion cells are designed for specific applications and the degradation mechanisms occurring in cells vary based on the duty cycles and aging conditions. Often, multiple competing processes are responsible for cell performance degradation in practical cells. We studied commercial cells designed for high-power for hybrid electric vehicles. By designing electrochemical and post-mortem analytical studies, we analyzed and identified cell components and mechanisms responsible for power fade. Our results on study of commercial cells for identifying power fade mechanisms and cell components affecting degradation are discussed in **Chapter 5**.

1.2.4 Modeling full cell with NCM cathode and graphite anode

We took information and parameters obtained from experimental studies on commercial cells and used those to develop a model to study the effects of the lithium loss in SEI. Parameters from commercial cells were used to improve the accuracy and reliability of the model. Simulation results were validated by comparing to experimental results whenever possible. Incorporation of lithium loss into the model enabled qualitative and quantitative predictions to be made about the effects of lithium loss in SEI on power fade and capacity fade in practical cells.

1.3 Outline

The outline of the remainder of this dissertation is organized as follows.

1.3.1 Background

　　Chapter 2 provides a review of different components and working principles of a lithium-ion battery. A background on different electrode chemistries and degradation mechanisms are discussed. Brief review of modeling lithium-ion batteries is also presented.

1.3.2 Experimental methods

　　Cell fabrication, testing, and analysis techniques are discussed in **Chapter 3**.

1.3.3 Effects of dissolved transition metals on the electrochemical performance and SEI growth in lithium-ion batteries

　　In **Chapter 4**, accelerated testing is used to study dissolution occurring from positive electrodes containing transition metal oxides in full cells. Effects of dissolved transition metals in the electrolyte on cell capacity, impedance, and SEI growth are shown. A mechanism of SEI growth based on transition metal reduction on the negative electrode is presented.

1.3.4 Understanding power losses in commercial lithium-ion batteries employing mixed NCM cathodes and hard carbon anodes for HEV applications by using experimental methods

Results on capacity fade and resistance increase in commercial cells achieved via high temperature aging are described in **Chapter 5**. Experimental methods including electrochemical testing and post-mortem analysis were used to investigate performance losses in cells. Mechanisms for cell performance deterioration at different stages of aging were determined.

1.3.5 On capacity and power fade resulting from lithium loss in the SEI

Chapter 6 shows the modeling results of cells containing NCM positive electrodes and graphite negative electrodes. Discharge simulation results from the model are compared to experimental data in order to test the accuracy of the model. Effects of lithium loss in the SEI on cell capacity, resistance, and power were determined.

1.3.6 Conclusions and recommendation

Summary of this work and recommendations for possible future work are presented in **Chapter 7**.

1.4 References

1. *Sources of Greenhouse Gas Emissions*. 2015 7/21/2015 [cited 2015 09/09/2015]; Total U.S. Greenhouse Gas Emissions by Economic Sector in 2013]. Available from: http://www.epa.gov/climatechange/ghgemissions/sources.html.

2. Handwerger, J. *World: Electric vehicle production and lithium demand for electric vehicle batteries, 2008-2020*. 2014 05/09/2014 11/03/2015]; Available from: http://www.marketoracle.co.uk/Article45532.html.

3. Yan (Joann) Zhou, T.S., *E-drive Vehicle Sales Analyses*. 2014, Vehicle Technologies Annual Merit Review.

4. INEEL, *FreedomCAR Battery Test Manual for Power-Assist Hybrid Electric Vechicles*. 2003, Prepared for the U.S. Department of Energy.

5. Fuller, T.F., M. Doyle, and J. Newman, *Simulation and Optimization of the Dual Lithium Ion Insertion Cell.* Journal of the Electrochemical Society, 1994. **141**(1): p. 1-10.

6. Doyle, M., T.F. Fuller, and J. Newman, *Modeling of Galvanostatic Charge and Discharge of the Lithium Polymer Insertion Cell.* Journal of the Electrochemical Society, 1993. **140**(6): p. 1526-1533.

CHAPTER 2

BACKGROUND

Lithium-ion batteries have become the first choice for energy storage for a variety of applications. The use of lithium-ion batteries for various applications, including consumer electronics, electric vehicles (EVs), hybrid electric vehicles (HEVs), and satellites, has been on the rise since they were first commercialized by Sony [1]. Lithium-ion batteries have evolved a lot since they were first developed. All aspects of a lithium-ion battery including the cathode, anode, and electrolyte have improved significantly. The development of new electrode materials has provided for higher capacities, greater power capability, increased cyclability, lower cost, and improved safety of the batteries. These advancements have made a new generation of hybrid electric vehicles (HEV) viable. The characteristics that make lithium-ion batteries suitable for these applications include high specific energy, high specific power, high energy efficiency, and low rates of self-discharge [2]. Specific energy or gravimetric energy density of a battery indicates how much electrical energy a battery can store for a given mass and is measured in Wh/kg. Specific power of a battery indicates the maximum available power per unit mass and it is measured in W/kg. Self-discharge indicates the capability of batteries to retain charge during storage when there is no electrical contact between the electrodes. Self-discharge of a battery is used to measure the shelf life of batteries.

2.1 Components of li-ion battery

11

A schematic of a typical lithium-ion battery is shown in **Figure 2.1**. It consists of two electrodes separated by a porous polymer film that keeps the electrodes mechanically and electrically apart. The separator prevents electronic contact between the opposite electrodes but allows for the passage of lithium ions through its pores. An organic solvent containing a lithium salt serves as an electrolyte proving an ionic pathway between the electrodes. During cell discharge, electron moves from the negative electrode to the positive electrode through an external circuit. The direction of the electrons is reversed during charging.

The negative electrode is a composite that usually consists primarily of carbon (graphite, hard carbon, or coke,), which is the active material. The active material for the positive composite electrode is a lithiated transition metal oxide. Typically, negative electrodes are cast on a copper foil and positive electrodes are cast on an aluminum foil. These foils serve as current collectors, and all of the current is directed through the foil to the positive and negative tabs of the cell. Some of the common materials used as positive electrodes in lithium-ion batteries include lithium cobalt oxide ($LiCoO_2$), lithium iron phosphate ($LiFePO_4$), lithium manganese oxide ($LiMn_2O_4$), lithium nickel oxide ($LiNiO_2$), lithium nickel cobalt aluminum ($LiNi_aCo_bAl_cO_2$), and lithium nickel cobalt manganese oxide ($LiNi_aCo_bMn_cO_2$). Compared to graphite, these metal oxides have relatively low electronic conductivity. Consequently, conductive additives are used to lower the resistance of the electrodes. Carbon black is a commonly used conductive additive. The binders are mixed with active materials in electrodes to improve mechanical stability of the electrodes and to improve adhesion to the metal foils. Polyvinylidene fluoride (PVDF) is a commonly used binder in electrodes.
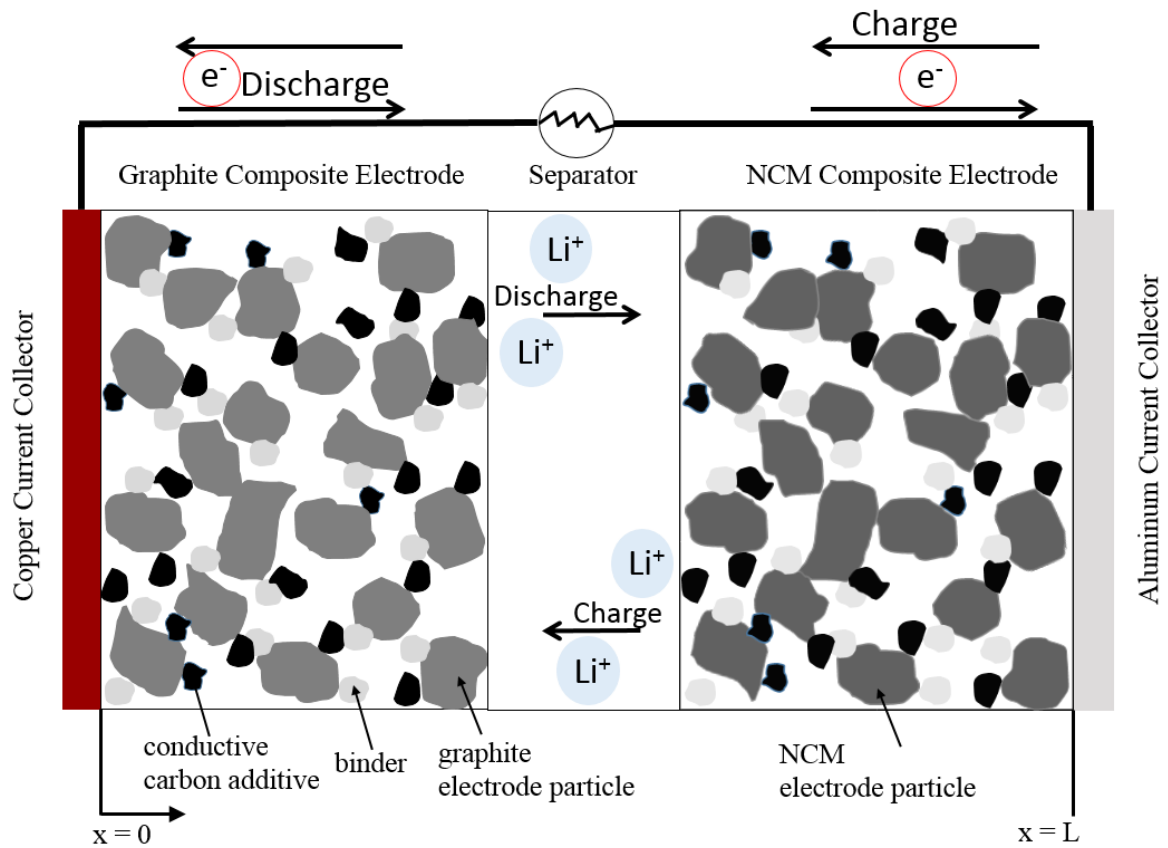
Figure 2-1. A schematic of a dual-insertion lithium-ion cell showing composite negative electrode and composite positive electrode. Porous separator separates the electrodes.

2.2 Review of electrodes

A brief background on different types of chemistries for electrode materials used lithium-ion batteries is provided here. Furthermore, electrode materials used in majority of this dissertation are highlighted.

2.2.1 Positive electrodes

Positive electrode materials in lithium-ion batteries generally determine the operating potential, reversible capacity, energy and power density, safety characteristics, toxicity, and cost of the cell. Lithium-ion batteries typically contain carbonaceous negative electrode, whereas a wide array of positive electrode materials are used. Thus, most of the cell properties and improvements are dependent on the choice of the positive electrode in the cell. Accordingly, the positive electrode is the component that has the larger effect on determining the power capability of the cell. Cell potential is a function of both the positive and negative electrode and it given by the difference of positive and negative electrode potentials; however, since graphite is the most commonly used active material in the negative electrode, the choice of positive electrode for all intents and purposes determines the operating potential. Commonly used positive electrode materials for lithium-ion batteries can be divided into three structural groups: spinel, olivine, and layered. Lithium manganese oxide ($LiMn_2O_4$) and lithium iron phosphate ($LiFePO_4$) are the most commonly used positive electrode materials with spinel and olivine structural configuration, respectively. The first commercial lithium-ion batteries developed by Sony in 1990 used layered lithium cobalt oxide ($LiCoO_2$) as the positive electrode material [1]. Low power capability and safety issues of $LiCoO_2$ prevent it from making a suitable positive electrode candidate for high-power applications [3]. Layered lithium metal oxides containing a mixture of nickel, cobalt, and manganese ($LiNi_aCo_bMn_cO_2$), commonly referred to as NCM, is a widely used positive electrode material. We focused primarily on NCM positive electrode material in this work because of the funding for this work and its use in charge sustaining hybrids.

NCM positive electrode materials show good performance in terms of capacity, cycling, power, and safety and are candidates for application in HEVs and EVs. These cathode materials have a high specific capacity (above 270 mAh/g) [4, 5] and high electrical conductivity compared to LiFePO$_4$ [6]. These materials also provide good thermal stability and safety [7-13]. NCM cathodes offer very good cyclability and storage properties. The charge/discharge reaction for NCM material is

$$Ni_aCo_bMn_cO_2 + yLi^+ + ye^- \rightleftharpoons Li_yNi_aCo_bMn_cO_2 \qquad [2\text{-}1]$$

where the forward direction represents a cell discharge, whereby Li$^+$ is inserted into the positive electrode, and the backward direction represents a cell charge where Li$^+$ is removed from the positive electrode and intercalated into the negative electrode.

2.2.2 Negative electrodes

Carbon is the most commonly used material for the negative electrode in lithium-ion batteries. Although some new materials have been introduced, carbon has remained the predominant choice since lithium-ion batteries were first commercialized. Graphite is the most widely used negative electrode material. The properties that make graphite the material of choice in a large number of negative electrodes is low cost, high abundance, high electrical conductivity, and high cyclability. In this work, we focus mainly in graphite because of its commercial applicability. The charge/discharge reaction for graphite electrode is

$$Li_xC_6 \rightleftharpoons xLi^+ + C_6 + xe^-, \qquad [2\text{-}2]$$

where a single Li atom is stored per 6 carbon atoms in graphite. The theoretical capacity of graphite is 372 mAh/g. There is small expansion and contraction of the active material during insertion and de-insertion of lithium. The volume change in graphite is 10 % compared to 270 % for Si [14]. Thus, graphite is a suitable electrode material.

Hard carbon is another commercially used carbon negative electrode materials. It differs from graphite as it contains smaller graphitic grains with disordered orientation and can provide higher gravimetric capacity compared to graphite [14]. However, lower volumetric capacity and susceptibility to SEI formation are drawbacks of hard carbon. Lithium titanium oxide ($Li_4Ti_5O_{12}$/LTO) is also used commercially in negative electrode for lithium-ion batteries because it provides protection against SEI formation and can provide high cycle life. However, the high cost of titanium and the high voltage relative to lithium are drawbacks of this material. LTO has an equilibrium potential of about 1.55 V vs. Li/Li^+, which results in lower cell potential for the full cell when used as a negative electrode.

2.3 Degradation in li-ion batteries

Capacity and power fade in lithium-ion batteries result from degradation in different components of the battery. These degradation mechanisms lead to a loss of cyclable lithium available for intercalation in the composite electrodes, increased internal resistance, decomposition of the electrolyte, active material dissolution from the electrodes, passive film formation over the surface of the electrodes, phase changes in the active materials, and loss of contact between the electrodes and current collector. It is these degradation modes that ultimately limit the life-time performance of the battery. Better

understanding of all the degradation phenomena is vital to the development of improved batteries and to extending their cycle life. Degradation is a big concern pertaining to batteries used in applications requiring long-term use. Batteries used in consumer electronics may be expected to last for two to three years whereas batteries used in EVs and HEVs must perform much longer without significant drops in capacity and power. A rule of thumb is that when the capacity reaches 80 % of its initial capacity, the battery has reach the end of its life. Automakers and the U.S. Department of Energy have set a calendar life of 15 years as a goal for batteries used in EVs and HEVs [15]. Thus, understanding cell degradation mechanisms becomes important in order to design cells to last longer without a decrease in performance over time.

Degradation mechanisms vary between the positive electrode, electrolyte, and the negative electrode. Degradation due to electrolyte affects the electrodes and, hence, is covered with electrodes here rather than separately.

2.3.1 Degradation in negative electrodes

During the first few cycles, side-reactions, i.e., reactions other than the intercalation of lithium into the electrode, occur on the negative electrode surface. The reaction is typically the reduction of the organic solvent or its salt. The reduction products accumulate on the graphite surface to form a passivating layer that is mostly electrically insulating. This passive layer is called the solid electrode interphase, SEI. This process is illustrated in **Figure 2-2** and the main features of the SEI are presented in the following discussion. Because the solvents react with lithium, the SEI serves an important role in the operation of a lithium-ion cell. An ideal SEI prevents or minimizes further electrolyte decomposition

by blocking electron transport while allowing ion transport through it [16]. SEI formation on the negative electrode/electrolyte interface is the main degradation mechanism occurring on the negative electrode in lithium-ion batteries [17]. It has been studied extensively by multiple researchers [16-19]. The physico-chemical properties of the SEI are strongly dependent on the electrolyte and the negative electrode used. Different factors like the choice of organic solvents, inorganic salts, electrolyte additives, type of carbon, mode of operation of the battery, and temperature affect SEI formation and its ensuing properties [20]. SEI growth affects cell performance due to lithium loss and impedance increase arising from SEI growth and related phenomenon.
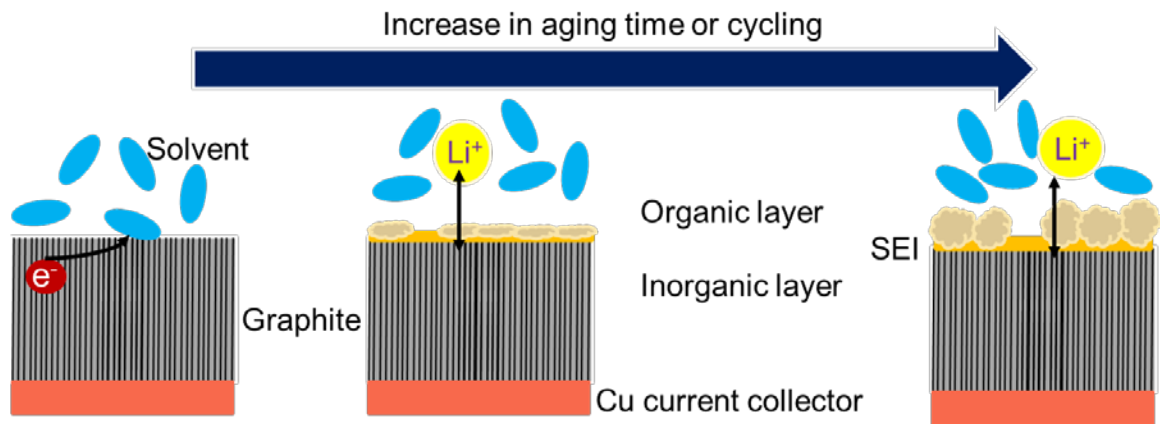
Figure 2-2. Solid electrolyte interphase (SEI) formation and growth in negative electrodes.

The potential at which the SEI forms depends on electrolyte composition and the negative electrode [20-25]. Ryu *et al.* showed that the solvent reduction dominates intercalation reaction in the potential range of 0.2 V-0.6 V (Li|Li$^+$) for LiAsF$_6$ + ethylene carbonate (EC) + diethyl carbonate (DEC) solution[22]. For LiPF$_6$ + EC + DEC solution, they found this potential range to be 0.25 V- 0.7 V (Li|Li$^+$). Aurbach reported that the

solvent reduction occurs at potentials higher than 0.3 V (Li|Li$^+$) for graphite electrodes [23]. Kang *et al.* reported EC reduction on graphite surface at 0.7 V (Li|Li$^+$) [24]. For LiClO$_4$ + EC + dimethyl carbonate (DMC) solution, reduction of EC on graphite has been reported to occur at 0.4 V (Li|Li$^+$) [26]. Aurbach *et al.* also found that the reduction of electrolyte components occurs in the range of 0.3 V-1 V (Li|Li$^+$) for propylene carbonate (PC) based electrolytes [21]. SEI formation occurs at a potential more positive than 1.0 V (Li|Li$^+$) for vinylene carbonate (VC) based electrolytes [25].

The SEI is comprised of inorganic and organic compounds resulting from the degradation of inorganic salts and organic solvents in the electrolyte. As previously stated, the composition of this layer depends on a lot of factors including the electrolyte, electrodes, temperature, and mode of operation. Aurbach *et al.* [21, 27-29] investigated EC based electrolytes on graphite and found that the major components of the SEI were lithium alkyl carbonate (ROCO$_2$Li) and lithium carbonate (Li$_2$CO3). For VC based electrolytes, Ota *et al.* [25] found that SEI formation due to VC reduction preceded that due to EC reduction. They found VC reduction products poly (vinylene carbonate), polyacetylene, lithium vinylene dicarbonate, lithium divinylene dicarbonate, and lithium carboxylate on graphite surface. Zhuang and Ross [30] suggested that the main components in the SEI formed on graphite electrode extracted from cycled commercial cells were lithium oxalate (Li$_2$C$_2$O$_4$), lithium carboxylate (RCOOLi), lithium methoxide (CH$_3$OLi), lithium hydroxide (LiOH), methanol (CH$_3$OH), and lithium hydrogen carbonate(LiHCO$_3$). The presence of lithium fluoride (LiF) is also reported for electrolytes comprised of fluorinated salts [31, 32].

The thickness of the passivating layer on carbon electrodes continues to grow with long cycling and storage, and is responsible for capacity fade [33]. The thickness of the SEI may vary from few nanometers to several hundreds of nanometers [34, 35]. The total resistance of the SEI is assumed to be in the range of 10-1000 $\Omega \cdot cm^2$ [36].

In addition to the electrolyte degradation and SEI growth, volume changes in the electrode, binder decomposition, current collector corrosion, and lithium plating are also known causes of degradation affecting the negative electrode [37]. Volume changes in the electrode may cause changes in porosity and an increase of the contact resistance in the electrode. Binder decomposition may lead to loss of mechanical stability. Lithium plating leads to loss of lithium and decreased cell capacity and power.

2.3.2 Degradation in positive electrodes

Positive electrode materials in batteries degrade via several mechanisms causing performance losses in batteries. **Figure 2-2** provides an overview of some of the common degradation mechanisms in positive electrode materials. The losses in cell performance due to degradation in positive electrode materials are associated with the dissolution of active materials, loss of contact to conductive particles, surface layer formation, micro cracking, loss of contact with conductive particles, corrosion of current collector, binder decomposition, and structural degradation.

Active material dissolution from cathodes is a prevalent problem in lithium-ion batteries. Dissolution occurring in cathode materials is specific to the active materials and electrolytes used and factors like structural defects in active materials, charging potentials, and carbon additive content in cathodes are responsible for the degree of dissolution.

Electrodes with structural defects may have a weak bonding of transition metal and oxygen

which may cause dissolution at high
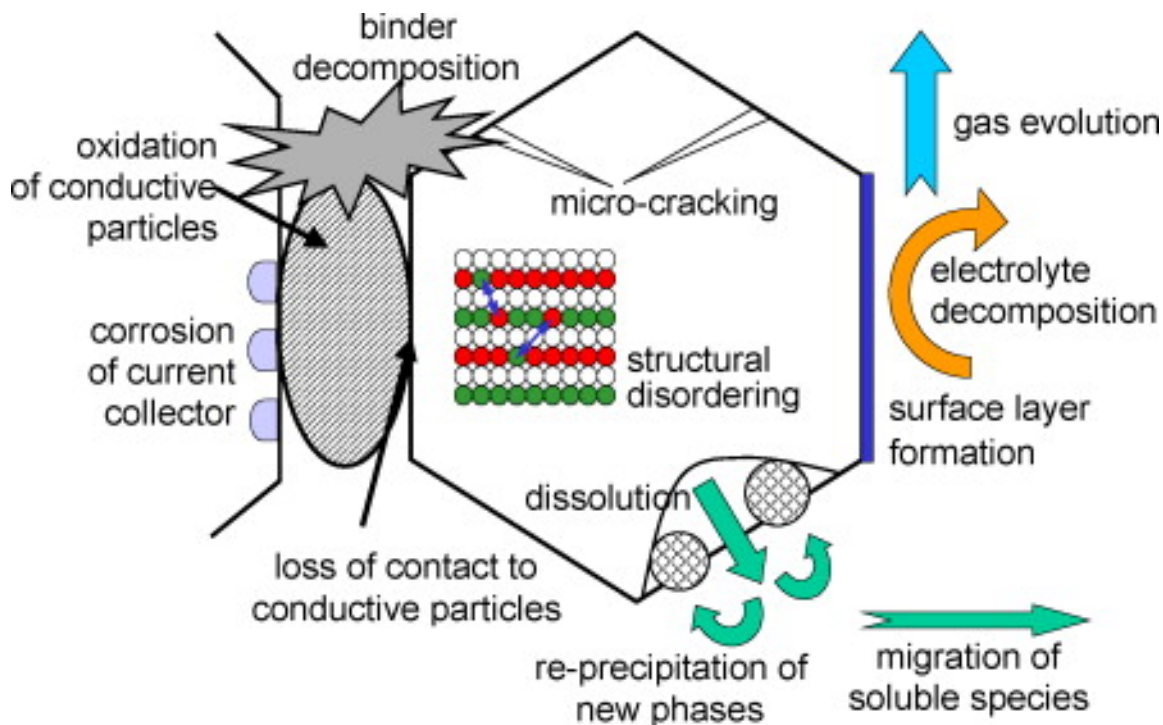
Figure 2-3. Summary of degradation mechanisms in positive electrode materials. Reprinted from [37] with permission.

potentials [17]. Dissolution of active material from electrode leads to capacity fade because

of material loss and increased cell resistance [38, 39]. Mn dissolution in spinel electrodes

is an important issue; and thus, dissolution has been studied mostly in spinel electrode

systems [40, 41]. The actual mechanism for dissolution is still under debate and different

mechanisms are proposed by various researchers[17]. Mn^{2+} resulting from dissolution is

transported to the anode and reduced on the surface

$$Mn^{2+} + 2e^- \rightarrow Mn(s) \qquad\qquad [2\text{-}3]$$

Mn dissolution is aided by trace amounts of moisture present in li-ion batteries. In fluorine based electrolytes, water reacts with fluorinated salts and produces HF. The acidic environment leads to transformation of active material and enhances dissolution [42]. Wang *et al.* [41]studied dissolution in $LiMn_2O_4$ electrodes and concluded that dissolution occurs at the end of charge (EOC) and the end of discharge (EOD). They also found that the extent of dissolution is greater at EOC (>4.1V) compared to EOD (<3.1V). Recently, capacity fade due to dissolution at high potentials for the same electrode material was studied by another group of researchers and they found manganese deposition on anode [43]. They ascribed part of the capacity fade occurred to the loss of mobile lithium ions due to manganese deposition on anode. When comparing the capacity fades from the two electrodes, they found that the anode contribution was greater. Transition metal deposited on anodes may accelerate the degradation of the electrolyte leading to thicker SEI. The presence of the SEI does not prevent transition metals from depositing on anode surface [44].

Loss of contact between active material and current collector as well as contact between active material and conductive additives like carbon leads to significant capacity losses in lithium-ion batteries. Active materials that have excellent intrinsic electronic properties and conductive agents providing good contact with active materials facilitate faster ionic exchange and electronic transfer throughout the cathode. The electronic properties of cathodes depend not only on the type of active materials and conductive additives, but also on their relative composition in cathodes [45, 46].

A homogenous distribution of carbon additives in cathodes is important in providing good contact with active material for better electronic properties. Non-uniform

contact resistance and decreased electronic conductivity in the electrode occurs because of the non-homogeneity in the distribution of carbon additives caused during various manufacturing processes. Because of these irregularities, there is not a continuous conducting network between the active material particles, which leads to inferior electronic properties [47]. Kerlau *et al.* studied capacity and power fade in composite cathodes and concluded that the decline in electronic properties of cathodes is due to rearrangement of carbon additives and formation of surface film [48]. Repeated mechanical stresses on electrodes during the life of the battery leads to increased contact resistance. Concentration of carbon additives and conductivity of cathode surface decreased over time with cycling [48]. An increase in the resistance of electrodes also occurs as a result of loss of active material contact with current collector. In cathodes with aluminum current collectors, the acid generated in $LiPF_6$ containing electrolytes corrodes aluminum over time. Similarly, for anodes with copper current collectors, corrosion of copper occurs when the cell is over-discharged [49].

2.4 Battery modeling

Materials development has led to a whole array of new electrode chemistries for lithium-ion batteries. These new electrode materials have to be qualified for use in lithium-ion batteries. There are several challenges towards qualifying the new materials: time of testing, methods of testing, and cost. First, there are limitations to the amount of time that a material can be tested. As a result of constant improvements in materials, present long-term testing for use in applications such as EVs, HEVs, and satellites may not be viable for battery developers. By the time of qualification, newer and more advanced batteries will

have replaced the older generation of batteries. We can consider the requirement prescribed by the DOE for a calendar life of 15 years for batteries for power-assist HEVs [15]. Second, a well-defined series of tests can be used to induce accelerated degradation. However, experimental testing can be limiting due to the onset of multiple degradation mechanisms occurring simultaneously, with no optimal method to separate them. Finally, for battery manufacturers, there are economic factors and limitations in resources to consider while testing new unproven materials for long-term applications.

Battery models can help alleviate some of these limitations by enabling long-term prediction of performance via simulations, thus allowing for the use of accelerated testing with more confidence. One approach is to perform extensive lab testing and correlate the data through equivalent circuits, reduced ordered models, or curve fits [50, 51]. This approach, which represents a lot of the present practice, has limitations because of the time spent to collect the data. The predictive capabilities of this method are limited to the system that has been used to generate data, and predictions cannot be extended beyond the limits for which the system has been tested. This approach fails to identify the mechanisms responsible for performance degradation; and hence, improvements to the system cannot be made. Another approach includes using statistical methods and smart data analysis [52-54]. The most important factors responsible for performance degradation can be identified using this method and performance predictions can be made outside the range for which the data were collected. However, this method cannot be used to predict performance of new materials. The third approach is physics-based models [55, 56]. By understanding physics-based mechanisms and incorporating them into performance models, reliable predictions can be made. Use of accurate physico-chemical parameters for different

24

systems can render these models to make reliable predictions about long-term performances for different types of materials.

Fuller *et al.* [57] developed a model to simulate a full lithium-ion cell with two insertion electrodes. They used their model to simulate the behavior of a cell consisting of graphite and lithium manganese oxide ($LiMn_2O_4$) as the negative and positive electrode, respectively. Because of the detailed physics used in this model, it is applicable to other electrode materials and the incorporation of additional phenomena is simple. This model has been used by other researchers for different insertion electrodes and additional phenomena have been incorporated [58, 59]. With detailed understanding of relevant thermodynamics, kinetics, and transport phenomenon occurring in the battery, a predictive model that can make reliable estimates about the long-term performances of a battery can be developed. Physicochemical data that describe the properties and behavior of the experimental cell are needed for materials used in the system. These, coupled with mechanisms responsible for degradation in the experimental cell, enable to increase the predictability of the model. Because of these characteristics, these type of models are faster and cheaper alternatives to empirical models.

2.5 References

1.   Tarascon, J.M. and M. Armand, *Issues and challenges facing rechargeable lithium batteries.* Nature, 2001. **414**(6861): p. 359-367.

2.   Husain, I., *Electric and hybrid vehicles : design fundamentals*. 2003, Boca Raton, Fla. :: CRC Press.

3.   Julien, C., et al., *Comparative Issues of Cathode Materials for Li-Ion Batteries.* Inorganics, 2014. **2**(1): p. 132.

4.   Li, J., et al., *Synthesis and electrochemical performance of the high voltage cathode material Li[Li0.2Mn0.56Ni0.16Co0.08]O-2 with improved rate capability.* Journal of Power Sources, 2011. **196**(10): p. 4821-4825.

5.   Wohlfahrt-Mehrens, M., et al., *Study of multi-walled carbon nanotubes for lithium-ion battery electrodes.* Journal of Power Sources, 2011. **196**(6): p. 3303-3309.

6.   Ngala, J.K., et al., *The synthesis, characterization and electrochemical behavior of the layered LiNi0.4Mn0.4Co0.2O2 compound.* Journal of Materials Chemistry, 2004. **14**(2): p. 214-220.

7.   MacNeil, D.D., Z. Lu, and J.R. Dahn, *Structure and electrochemistry of Li NixCo1-2xMnx O-2 (0 <= x <= 1/2).* Journal of the Electrochemical Society, 2002. **149**(10): p. A1332-A1336.

8.   MacNeil, D.D., et al., *A comparison of the electrode/electrolyte reaction at elevated temperatures for various Li-ion battery cathodes.* Journal of Power Sources, 2002. **108**(1-2): p. 8-14.

9.   Jouanneau, S., et al., *Morphology and Safety of Li NixCo1-2xMnx O-2 (0 <= x <= 1/2).* Journal of the Electrochemical Society, 2003. **150**(10): p. A1299-A1304.

10.   Belharouak, I., et al., *Li(Ni1/3Co1/3Mn1/3)O-2 as a suitable cathode for high power applications.* Journal of Power Sources, 2003. **123**(2): p. 247-252.

11.   Liu, X., et al., *A mixture of LiNi1/3Co1/3Mn1/3O2 and LiCoO2 as positive active material of LIB for power application.* Journal of Power Sources, 2007. **174**(2): p. 1126-1130.

12.   Wang, Y.D., J.W. Jiang, and J.R. Dahn, *The reactivity of delithiated Li(Ni1/3Co1/3Mn1/3)O-2, Li(Ni0.8Co0.15Al0.05)O-2 or LiCoO2 with non-aqueous electrolyte.* Electrochemistry Communications, 2007. **9**(10): p. 2534-2540.

13.   Qin, Y., et al., *Electrolyte additive to improve performance of MCMB/LiNi1/3Co1/3Mn1/3O2 Li-ion cell.* Journal of Power Sources, 2010. **195**(19): p. 6888-6892.

14.   Nitta, N., et al., *Li-ion battery materials: present and future.* Materials Today, 2015. **18**(5): p. 252-264.

15.   INEEL, *FreedomCAR Battery Test Manual for Power-Assist Hybrid Electric Vechicles.* 2003, Prepared for the U.S. Department of Energy.

16.   Peled, E., et al., *The role of SEI in lithium and lithium ion batteries.* Materials for Electrochemical Energy Storage and Conversion - Batteries, Capacitors and Fuel Cells, 1995. **393**: p. 209-221.

17.   Arora, P., R.E. White, and M. Doyle, *Capacity fade mechanisms and side reactions in lithium-ion batteries.* Journal of the Electrochemical Society, 1998. **145**(10): p. 3647-3667.

18.   Andersson, A.M., K. Edstrom, and J.O. Thomas, *Characterisation of the ambient and elevated temperature performance of a graphite electrode.* Journal of Power Sources, 1999. **81**: p. 8-12.

19.   Golodnitsky, D., et al., *XPS analysis of the SEI formed on carbonaceous materials.* Solid State Ionics, 2004. **170**(1-2): p. 83-91.

20.   Verma, P., P. Maire, and P. Novak, *A review of the features and analyses of the solid electrolyte interphase in Li-ion batteries.* Electrochimica Acta, 2010. **55**(22): p. 6332-6341.

21.   Aurbach, D., et al., *Failure and stabilization mechanisms of graphite electrodes.* Journal of Physical Chemistry B, 1997. **101**(12): p. 2195-2206.

22.   Ryu, Y.G. and S.I. Pyun, *Passivation kinetics of surface films formed on a graphite electrode in organic lithium salt solution as a function of salt anion type.* Journal of Electroanalytical Chemistry, 1997. **433**(1-2): p. 97-105.

23.   Aurbach, D., *Review of selected electrode-solution interactions which determine the performance of Li and Li ion batteries.* Journal of Power Sources, 2000. **89**(2): p. 206-218.

24.   Kang, S.H., et al., *Investigating the solid electrolyte interphase using binder-free graphite electrodes.* Journal of Power Sources, 2008. **175**(1): p. 526-532.

25.   Ota, H., et al., *Analysis of vinylene carbonate derived SEI layers on graphite anode.* Journal of the Electrochemical Society, 2004. **151**(10): p. A1659-A1669.

26.   Kotz, R., et al., *Electrochemical SPM investigation of the solid electrolyte interphase film formed on HOPG electrodes.* Electrochemistry Communications, 2000. **2**(6): p. 436-440.

27.   Aurbach, D., et al., *The Behavior of Lithium Electrodes in Propylene and Ethylene Carbonate - The Major Factors That Influence Li Cycling Efficiency.* Journal of Electroanalytical Chemistry, 1992. **339**(1-2): p. 451-471.

28.   Aurbach, D., et al., *The Study of Electrolyte-Solutions Based on Ethylene and Diethyl Carbonates for Rechargeable Li Batteries .2. Graphite-Electrodes.* Journal of the Electrochemical Society, 1995. **142**(9): p. 2882-2890.

29.   Aurbach, D., et al., *A comparative study of synthetic graphite and Li electrodes in electrolyte solutions based on ethylene carbonate dimethyl carbonate mixtures.* Journal of the Electrochemical Society, 1996. **143**(12): p. 3809-3820.

30.   Zhuang, G.R.V. and P.N. Ross, *Analysis of the chemical composition of the passive film on Li-ion battery anodes using attentuated total reflection infrared Spectroscopy.* Electrochemical and Solid State Letters, 2003. **6**(7): p. A136-A139.

31.   Andersson, A.M. and K. Edstrom, *Chemical composition and morphology of the elevated temperature SEI on graphite.* Journal of the Electrochemical Society, 2001. **148**(10): p. A1100-A1109.

32.   Peled, E., et al., *An advanced tool for the selection of electrolyte components for rechargeable lithium batteries.* Journal of the Electrochemical Society, 1998. **145**(10): p. 3482-3486.

33.   Huang, C.K., Smart, M., Davies, E., Cortez, R., Surampudi, S. in *The 190th Electrochem. Soc. Meeting*. 1996. San Antonio: The Electrochemical Society.

34.   Yoshida, T., et al., *Degradation mechanism and life prediction of lithium-ion batteries.* Journal of the Electrochemical Society, 2006. **153**(3): p. A576-A582.

35.   Edstrom, K., M. Herstedt, and D.P. Abraham, *A new look at the solid electrolyte interphase on graphite anodes in Li-ion batteries.* Journal of Power Sources, 2006. **153**(2): p. 380-384.

36. Peled, E., Golodnitsky, D., ed. *Lithium-ion Batteries : Solid-Electrolyte Interphase*. ed. P.B. Balbuena and Y. Wang. 2004, Imperial College Press: London :.

37. Vetter, J., et al., *Ageing mechanisms in lithium-ion batteries.* Journal of Power Sources, 2005. **147**(1-2): p. 269-281.

38. Jang, D.H., Y.J. Shin, and S.M. Oh, *Dissolution of spinel oxides and capacity losses in 4V Li/LixMn2O4 coils.* Journal of the Electrochemical Society, 1996. **143**(7): p. 2204-2211.

39. Park, J., et al., *Numerical Simulation of the Effect of the Dissolution of LiMn(2)O(4) Particles on Li-Ion Battery Performance.* Electrochemical and Solid State Letters, 2011. **14**(2): p. A14-A18.

40. Aoshima, T., et al., *Mechanisms of manganese spinels dissolution and capacity fade at high temperature.* Journal of Power Sources, 2001. **97-8**: p. 377-380.

41. Wang, L.F., et al., *Study of mn dissolution from LiMn2O4 spinel electrodes using rotating ring-disk collection experiments.* Journal of the Electrochemical Society, 2003. **150**(7): p. A905-A911.

42. Blyr, A., et al., *Self-discharge of LiMn2O4/C Li-ion cells in their discharged state - Understanding by means of three-electrode measurements.* Journal of the Electrochemical Society, 1998. **145**(1): p. 194-209.

43.   Tsujikawa, T., et al., *A Study on the Cause of Deterioration in Float-Charged Lithium-Ion Batteries Using LiMn(2)O(4) as a Cathode Active Material.* Journal of the Electrochemical Society, 2011. **158**(3): p. A322-A325.

44.   Komaba, S., N. Kumagai, and Y. Kataoka, *Influence of manganese(II), cobalt(II), and nickel(II) additives in electrolyte on performance of graphite anode for lithium-ion batteries.* Electrochimica Acta, 2002. **47**(8): p. 1229-1239.

45.   Dettlaff-Weglikowska, U., et al., *Effect of Single-Walled Carbon Nanotubes as Conductive Additives on the Performance of LiCoO(2)-Based Electrodes.* Journal of the Electrochemical Society, 2011. **158**(2): p. A174-A179.

46.   Zane, D., et al., *Factor affecting rate performance of undoped LiFePO4.* Electrochimica Acta, 2004. **49**(25): p. 4259-4271.

47.   Chen, G. and T.J. Richardson, *Continuity and performance in composite electrodes.* Journal of Power Sources, 2010. **195**(16): p. 5387-5390.

48.   Kerlau, M., et al., *Studies of local degradation phenomena in composite cathodes for lithium-ion batteries (Reprinted from Electrochimica Acta vol 52, pg 5422-5429, 2007).* Electrochimica Acta, 2007. **53**(3): p. 1385-1392.

49.   Myung, S.T., Y. Hitoshi, and Y.K. Sun, *Electrochemical behavior and passivation of current collectors in lithium-ion batteries.* Journal of Materials Chemistry, 2011. **21**(27): p. 9891-9911.

50.   Liaw, B.Y., et al., *Modeling capacity fade in lithium-ion cells.* Journal of Power Sources, 2005. **140**(1): p. 157-161.

51.   Sone, Y., et al., *Cycle-life evaluation of the 30 Ah prismatic Li-ion secondary cells for low earth orbit satellite.* Electrochemistry, 2003. **71**(7): p. 542-548.

52.   Sauer, D.U. and H. Wenzl, *Comparison of different approaches for lifetime prediction of electrochemical systems - Using lead-acid batteries as example.* Journal of Power Sources, 2008. **176**(2): p. 534-546.

53.   Safari, M., et al., *Life-Prediction Methods for Lithium-Ion Batteries Derived from a Fatigue Approach I. Introduction: Capacity-Loss Prediction Based on Damage Accumulation.* Journal of the Electrochemical Society, 2010. **157**(6): p. A713-A720.

54.   Safari, M., et al., *Life Prediction Methods for Lithium-Ion Batteries Derived from a Fatigue Approach II. Capacity-Loss Prediction of Batteries Subjected to Complex Current Profiles.* Journal of the Electrochemical Society, 2010. **157**(7): p. A892-A898.

55.   Safari, M., et al., *Multimodal Physics-Based Aging Model for Life Prediction of Li-Ion Batteries.* Journal of the Electrochemical Society, 2009. **156**(3): p. A145-A153.

56.   Darling, R. and J. Newman, *Modeling side reactions in composite LiyMn2O4 electrodes.* Journal of the Electrochemical Society, 1998. **145**(3): p. 990-998.

57.   Fuller, T.F., M. Doyle, and J. Newman, *Simulation and Optimization of the Dual Lithium Ion Insertion Cell.* Journal of the Electrochemical Society, 1994. **141**(1): p. 1-10.

58.   Ramadass, P., et al., *Mathematical modeling of the capacity fade of Li-ion cells.* Journal of Power Sources, 2003. **123**(2): p. 230-240.

59.   Chandrasekaran, R. and T.F. Fuller, *Analysis of the Lithium-Ion Insertion Silicon Composite Electrode/Separator/Lithium Foil Cell.* Journal of the Electrochemical Society, 2011. **158**(8): p. A859-A871.

CHAPTER 3

EXPERIMENTAL TECHNIQUES TO STUDY DEGRADATION

Cell capacity and power fade occur via multiple degradation mechanisms that affect different cell components. Different electrochemical and analytical techniques can be used to better understand these mechanisms. Experimental analysis helps us identify cell components and probable mechanisms responsible for performance losses in a cell. Techniques used in this study helped characterize cell performance in terms of cell capacity, power, and resistance. Furthermore, analytical and electrochemical techniques were also used to investigate changes in structure of the electrodes and conductivity of the electrodes to identify possible cell degradation mechanisms.

Resistance in a lithium ion battery is normally measured by applying a current and measuring the voltage response of the cell. When a current is applied to a cell, the voltage is dependent on the open-circuit potential of both electrodes, and the overpotentials resulting from concentration polarization and charge transfer polarization, as well as the ohmic losses in the cell. This resistance is referred to as the cell resistance and it differs from the internal resistance and ohmic resistance in the cell, as it includes contributions due to kinetic and mass transfer polarization. Cell resistance increase is a major cause of performance loss in batteries used in high power application. It can occur due to degradation of different cell components that lead to cell resistance increase via different mechanisms. Identifying the cell components and related mechanisms for cell resistance increase can enable better cell design and remediation techniques. **Figure 3.1** shows different causes of cell resistance increase in cells. It highlights different ways in which

performance degradation occurs and also lists experimental and analytical techniques to study cell components and degradation mechanisms.

Increase in cell resistance in lithium-ion batteries is explored in detail in **Chapter 5** is by applying experimental methods. Fault tree highlighted in **Figure 3.1** was used as a guide to look at several cell components and degradation mechanisms occurring in the cell. Conductivity changes of each electrode and of the electrolyte, microstructure analysis of the electrodes, capacity changes of each electrode, and surface analysis of each electrode were performed by utilizing electrochemical and analytical experimental techniques to understand cell resistance and power fade mechanisms in lithium ion cells.

In this study, we examined different degradation mechanisms occurring in cells. We completed a variety of experiments using different instruments and techniques to study degradation. We fabricated coin cells and pouch cells, carried out electrochemical testing, and post-mortem analyses on tested cells to further study the cell components.

3.1 Cell fabrication

$Li_{1.05}Ni_{1/3}Co_{1/3}Mn_{1/3}$ (NCM) (NM- 3100, Toda America) was used as the active material in the positive electrodes. For full-cell studies, commercial graphite electrodes were used for the negative electrode. For half-cell studies, lithium metal foil (Sigma Aldrich) was used for the negative electrode. To prepare the composite positive electrode, carbon black (Super C65) and graphite (KS 6L) supplied by TIMCAL were used as conductive additives. Polyvinylidene fluoride (PVDF) (Kureha-7305) supplied by Kureha America was the binder used for the positive electrode. The PVDF was dissolved in N-methyl-2-pyrrolidinone (NMP) and consisted of 5% (by weight) polymer. The

compositions of the positive electrode were 87 % (NCM active material), 5 % carbon black (CB), 3 % graphite, and 5 % PVDF by weight. The separator used was a tri-layer polyethylene/polypropylene membrane developed by Celgard (Celgard 2325). 1M $LiPF_6$ in ethylene carbonate/diethylene carbonate (EC/DEC) (1:1 by wt. %) (Novolyte Technologies) was the electrolyte used. For dissolution studies in **Chapter 4**, Nickel(II) Bis(trifluoromethanesulfonyl)imide $(Ni(TFSI)_2)$ (Solvionic), Cobalt(II) Bis(trifluoromethanesulfonyl)imide $(Co(TFSI)_2)$ (Solvionic), and Manganese(II) Bis(trifluoromethanesulfonyl)imide $(Mn(TFSI)_2)$ (Solvionic) were added to the electrolyte to simulate degradation occurring via metal dissolution from positive electrodes.
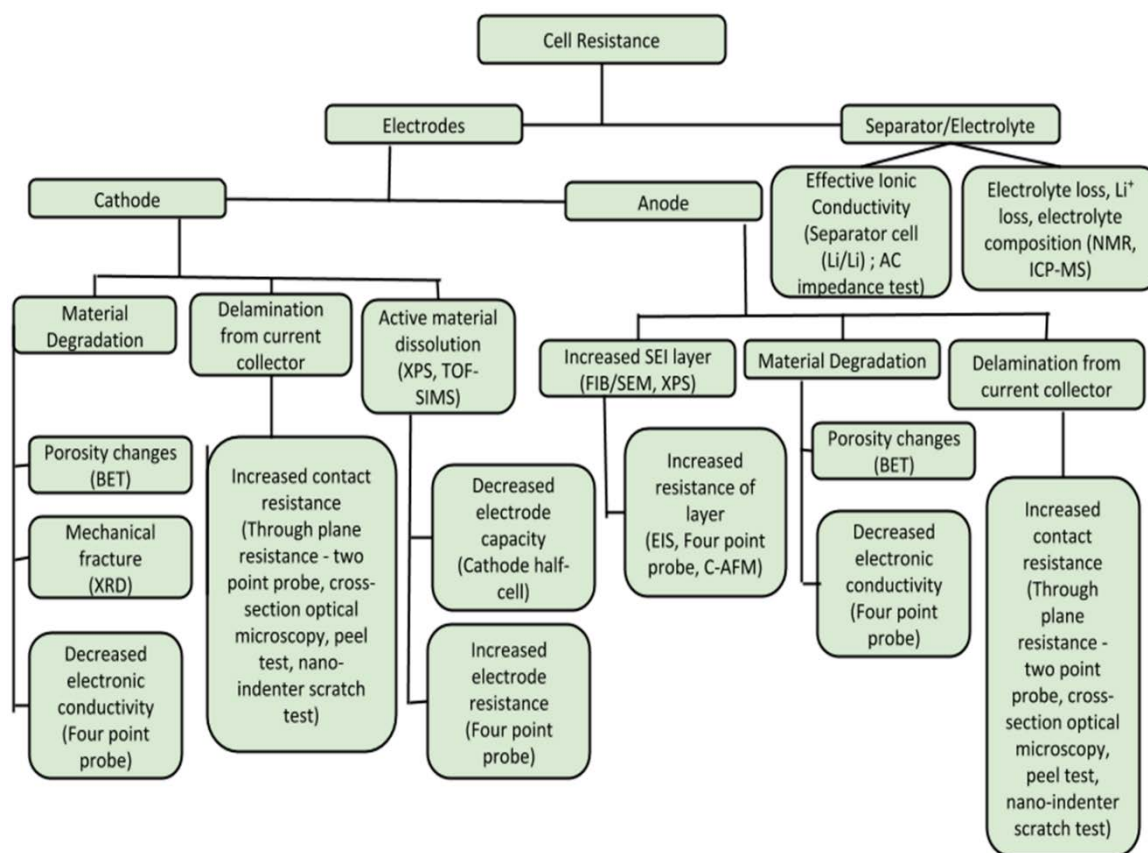
Figure 3-1. Degradation mechanisms affecting cell resistance are shown here. Different cell components along with degradation mechanisms including the experimental and analytical techniques used to study degradation mechanisms and cell components are also shown.

A slurry was prepared by mixing the active material, carbon black, graphite, and binder (PVDF in NMP) in appropriate weight percentages. Good mixing was achieved by stirring the mixture with an ultrasonic liquid processor (Sonicator 3000, Misonix) for 30 minutes. For consistent mixing, the slurry was mixed manually using a spatula at each 15 minutes interval. The next mixing step involved stirring the slurry using a magnetic stir bar for additional two hours. The mixed slurry was cast onto an aluminum current collector. The current collector was placed on a vacuum plate (DP-201505, Gardco) and mixed slurry was spread evenly onto the current collector using a doctor blade (AP-99500403, Gardco).

After casting, the coated metal foil was transferred to a vacuum chamber. The cast was dried at 120 °C overnight.

Coin cells in 2032 configuration were fabricated to study degradation in the cell. Electrodes with 1.4 cm diameter were cut using an arch punch. The diameter of the separator was slightly larger (1.6 cm diameter) than the size of the electrode. Thus, contact between the opposite electrodes was avoided. Coin cell hardware was purchased from Pred materials. The negative electrode was placed on the bottom case and the separator was placed over it. Electrolyte (150 µL) was added to wet the separator. Positive electrode material was placed over the separator facing the negative electrode. Stainless steel spacer and a disk spring were put on top of the positive electrode and a casing top with a gasket was used to enclose the coin cell. The cell was sealed using a hydraulic crimper (MTI Corporation). Cell fabrication was carried out inside an Argon filled glovebox. Moisture and oxygen level in the glovebox were less than 1 ppm.

3.2 Battery Cycling

Testing of coin cells was started the day after the cells were assembled. Cells were visually inspected for electrolyte leaks. Good contact of the electrodes or possible shorting was also checked by measuring the potential difference across the cell before cycling tests. All cycling tests were performed on Arbin BT2000 battery cycler (Arbin Instruments). Initial formation cycles included 5 charge and discharge cycles at C/10 rate based on the theoretical capacity of the positive electrode. In lithium-ion batteries, there is a sharp drop in cell capacity during the first few cycles due to side reactions such as passivation of the negative electrode or SEI formation. Normally, cells are conditioned or cycled to allow this

process to occur prior to use. This initial cycling period is referred to as the formation period. C-rate is a measure of the current used to charge or discharge a cell. When a fully charged cell is discharged at a rate of 1C, the discharge takes one hour. Similarly, a discharge of a fully charged cell at C/10 takes 10 hours to complete. Cells were charged by following the constant current-constant voltage (CC-CV) protocol. During charging, the end-of-charge (EOC) voltage limit was set at 4.2 V (recommended by supplier for NCM materials). The voltage limits for charge and discharge are dependent on choice of electrode materials and electrolyte used in the cell. As we discussed in **Chapter 2**, side reactions occurring in batteries affect performances and safety of batteries. In order to limit the degradation due to side reactions, a stable voltage window is chosen based on the electrode materials and electrolyte used in a battery. The galvanostatic (constant current) charge at C/10 was maintained until this EOC voltage was met; then cells were then held at 4.2 V until current dropped to C/20. This combination of charging steps, where a constant voltage charging step follows a constant current charging step, is normally referred to as CC-CV charging protocol. After each charge and discharge step, there was a rest period of one hour to allow the cells to achieve electrochemical equilibrium. The discharge was carried out at a rate of C/10. The discharge step continued until end-of-discharge (EOD) voltage limit of 2.75 V was met. Discharging the cells to lower potentials can permanently damage the cells. EOD voltage limit depends on the material used.

Discharge capacity of the cell at the end of the formation cycles was used as the true cell capacity. All subsequent testing after formation cycling were based on capacity measured at the end of the formation cycles. Long-term cycling tests helped study the cell and the electrode capacities during formation and changes occurring during cycling.

Changes in cell and electrode capacities, rate capabilities, and coulombic efficiencies (discharge capacity/charge capacity x 100 %) were studied using this technique. Commercial cells were tested in an environmental chamber at fixed temperatures. All lab-made cells were tested at room temperature outside the environmental chamber. Testing at room temperature outside the environmental chamber was done due to a lack of availability of a temperature chamber for these tests.

3.3 Electrochemical impedance spectroscopy

Electrochemical impedance spectroscopy (EIS) was performed on cells using a potentiostat/galvanostat (Model PGSTAT302N, Metrohm-Autolab) running Nova software. EIS is a powerful technique that is useful to decouple impedance contributions to total impedance in electrochemical systems. Various physicochemical processes in an electrochemical cell such as transport processes and surface reactions have different characteristic time-constants and are exhibited at different alternating current (AC) frequencies. A small amplitude sinusoidal wave is applied to the cell and the frequency is varied from high to low values over a broad range to identify and quantify the impedances associated to different processes. The measured impedance is a complex number that can be broken into real and imaginary parts. Typically, EIS results are commonly represented using a Nyquist plot which contains the imaginary component of the impedance (commonly represented by -Z") on the vertical (y) axis and the real component of the impedance (commonly represented by Z') on the horizontal (x) axis.

In lithium-ion battery systems, impedance spectroscopy helps identify factors limiting performance including electrode and electrolyte conductivity, charge transfer properties, solid-state diffusion in electrodes, and properties of passivating surface layers. The impedance was carried out in the potentiostatic mode at open-circuit potentials at charged (graphite lithiated) states. The amplitude of the AC signal was set at 5 mV, and the frequency ranged from 1 MHz to 10 mHz. Description of this technique as it relates to studying degradation in lithium-ion batteries is provided again in **Chapters 4** and **5**.

3.4 Post-mortem analysis

Following electrochemical testing, cells were disassembled, and the electrodes and electrolyte from cycled cells were analyzed. Dismantling of cells was done inside a glovebox in an argon environment. Electrodes recovered from cells were soaked in dimethyl carbonate (DMC) to remove lithium salts and dried out inside the glovebox before analyses.

3.4.1 Half Cell

Cell capacity of the electrodes recovered from full cells tested in **Chapter 5** was measured by fabricating coin cell with lithium foil as reference/counter electrode. The electrodes used in full cells were double-sided (active material coating on both sides of the current collector). In order to use the electrodes in half cells, coating from one side was removed by soaking Kimwipes® in NMP solvent and gently wiping the electrode surface. This process was continued until the electrode coating was removed from one side. The

one-sided electrode thus prepared was dried in a vacuum oven at 120 °C for 12 hours to dry out any solvent or moisture from the electrode. The dried electrodes were transferred to a glovebox and cut into 1.4 cm diameter electrodes using an arch punch. Same sized lithium foil (Sigma Aldrich) was used as the reference/counter electrode and Celgard 2325 (1.6 cm diameter) was used as the separator. 150 µL of 1M LiPF$_6$ in EC:DEC 1:1 wt% was used as the electrolyte, and same fabrication process as described earlier was used.

3.4.2 Conductivity Cell

The conductivity of the electrolyte recovered from the commercial cells described in **Chapter 5** was measured by using coin cells with stainless steel electrodes. Two stainless steel electrodes were electrically isolated by using a separator (Celgard 2325). 150 µL of electrolyte recovered from the cells was used in the conductivity cell.

Using EIS tests, electrolyte resistance was calculated by averaging the solution impedances from five runs. EIS was carried out in the frequency range from 1 MHz to 1 kHz using a 5 mV amplitude. From the impedance spectrum, the impedance at the high frequency intercept on the real-axis was taken as the solution resistance for the electrolyte. This is illustrated in a Nyquist plot in **Figure 3-2**.
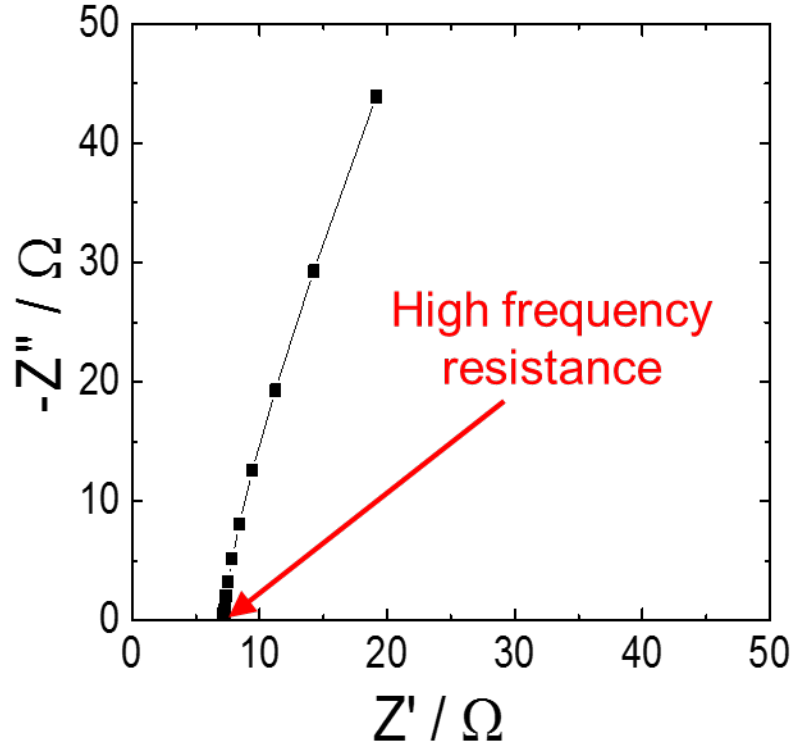
Figure 3-2. Example EIS used to find the solution resistance.

The effective conductivity (κ_{eff}) of the electrolyte through a separator membrane is given by

$$\kappa_{eff} = \frac{\kappa \cdot \varepsilon}{\tau}$$

[3-1]

where ε is the porosity of the separator and τ is the tortuosity of the membrane. The porosity of the separator (39 % for Celgard 2325) was obtained from the manufacturer. Tortuosity of the separator was determined experimentally using an electrolyte of known concentration and conductivity. In order to improve the accuracy of the measurements, five conductivity cells were made with different number of separators, and the solution resistance was measured as described earlier. 1 M of LiPF$_6$ in EC:DEC

(1:1 by wt %) with a known conductivity of 7.8 mS/cm was used. With known values of conductivity and porosity, **Equation 3.1** was used to calculate the apparent tortuosity of the separator. The effective conductivity can be calculated by using **Equation 3-2**. l and A are the thickness and area of the separator. R is the solution resistance, measured experimentally.

$$\kappa_{eff} = \frac{l \cdot \varepsilon}{R \cdot A \cdot \tau}$$ [3-2]

The number of separators was increased and the tortuosities obtained were plotted against the number of separators to obtain **Figure 3-3**. We can then obtain the true tortuosity of the separator using the slope of the curve obtained. The tortuosity value obtained for Celgard 2325 was 4.11.
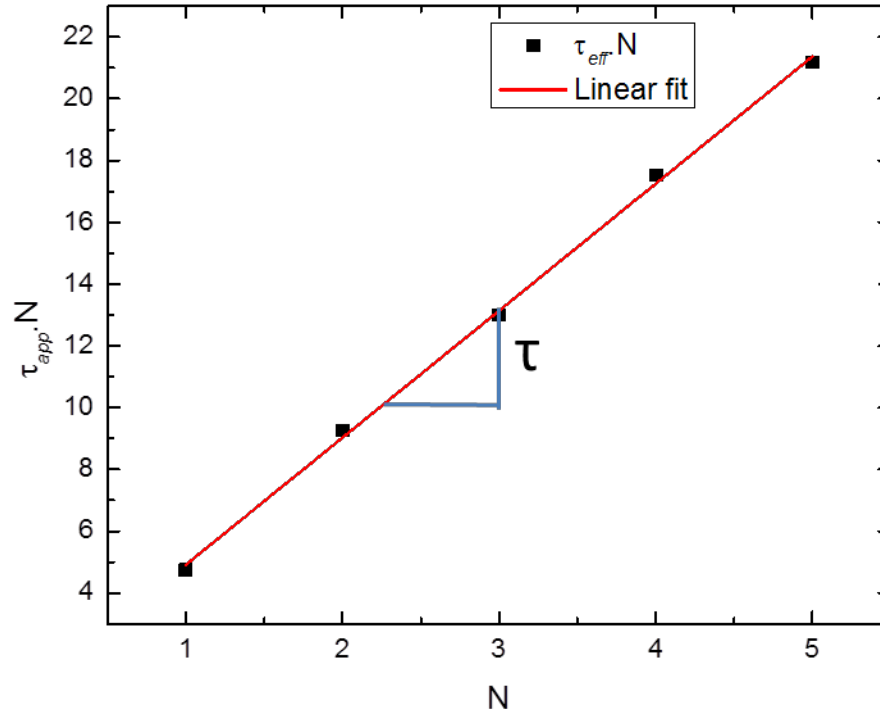
Figure 3-3. Calculation of true tortuosity of the separator using apparent tortuosity with increasing number of separators.

With the tortuosity thus calculated, similar experiments were conducted using the electrolyte from commercial cells with increasing number of separators. **Figure 3-4** shows the increasing solution resistance with added separators for the electrolyte from commercial cell studied in **Chapter 5**. From this curve, the slope of the curve was used as the true solution resistance and that value was used to calculate the conductivity of the electrolyte using **Equation 3.2**.
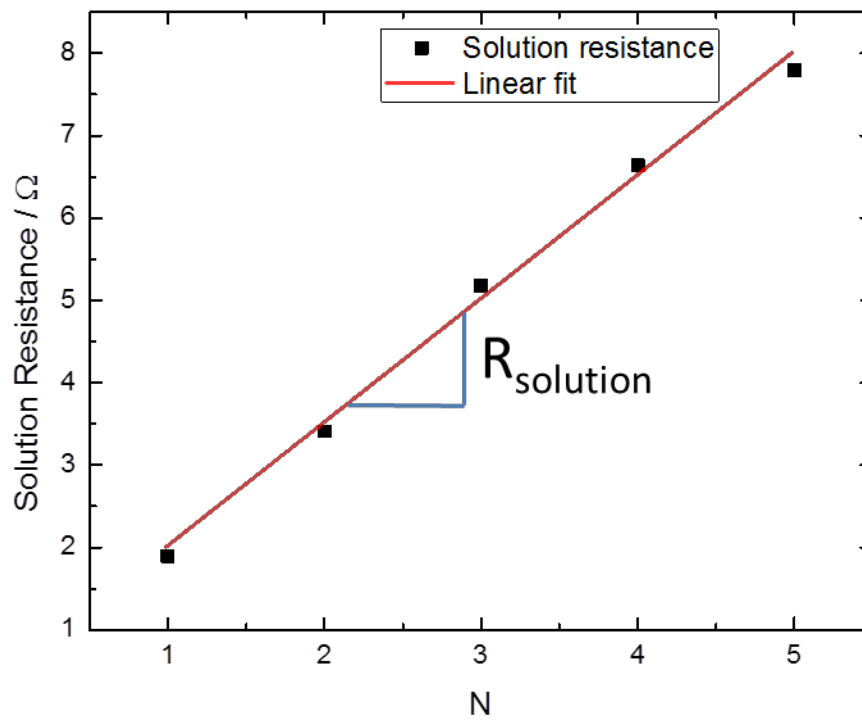
Figure 3-4. Variation of solution resistance with increasing number of separators for electrolyte from F-1.

High resolution scanning electron microscopy (HR-SEM) (Hitachi SU8000) was used to study the surface morphology of the electrodes. Focused ion beam section with SEM (FIB/SEM) was used to observe the surface morphologies of the surface layers by taking cross-sections of the electrodes. X-ray photoelectron spectroscopy (XPS) (Thermo K Alpha) was used to study the nature of the surface layers formed on the electrodes. Analysis techniques and parameters used in the studies are explained in corresponding sections in **Chapters 4** and **5**.

CHAPTER 4

EFFECTS OF DISSOLVED TRANSITION METALS ON THE ELECTROCHEMICAL PERFORMANCE AND SEI GROWTH IN LITHIUM-ION BATTERIES

4.1   Introduction

Consumption of fossil fuels in the transportation sector is one of the leading causes of greenhouse gas emissions (GHG) [1]. Efforts to develop cleaner and more efficient alternatives to the internal combustion engine running on petroleum fuels, such as fuel cells and batteries, are on the rise to mitigate this problem. Rechargeable lithium-ion (Li-ion) batteries offer high energy and power densities, good cyclic stability, and low rates of self-discharge. These characteristics are essential for applications in hybrid electric vehicles (HEV), plug-in hybrid vehicles (PHEV), and electric vehicles (EV) [2-8]. $LiCoO_2$, $LiFePO_4$, $LiMn_2O_4$, $LiNi_{1/3}Co_{1/3}Mn_{1/3}O_2$, and $LiNi_{0.8}Co_{0.15}Al_{0.05}O_2$ are some of the common materials used for positive electrodes in lithium-ion batteries. $LiNi_{1/3}Co_{1/3}Mn_{1/3}O_2$ (NCM) positive electrode materials operate safely over a wide voltage window from 2.5 V to 4.6 V (Li/Li^+). This positive electrode material can provide a high reversible capacity of around 160-180 mAh/g at high rates. NCM provides better thermal stability with the electrolyte at high states of charge compared to other positive electrodes, such as $LiNi_{0.8}Co_{0.15}Al_{0.05}O_2$, $LiNiO_2$, and $LiCoO_2$, which is important for high power applications [3, 7-14]. Dissolution of transition metals from the positive electrode is a concern for lithium-ion batteries, and manganese dissolution is a major reason for capacity fade in spinel electrodes, including $LiMn_2O_4$ [15]. Although less susceptible than spinel,

metal dissolution does occur in NCM electrodes and has been implicated in a rise in impedance and capacity fade with cycling [4, 16]. Two main routes by which capacity fading may occur due to dissolution are (i) structural changes to the positive electrode and leading to reduced insertion capacity and (ii) accelerated growth of the SEI at the negative electrode and the resulting irreversible Li consumption [15, 17-22]. Capacity fade due to the structural changes occurring in the positive electrode during partial dissolution is more likely in spinel electrodes, where the extent of dissolution is high, or at high potentials (overcharge). This large degree of dissolution in spinels may cause shrinkage of the active material, which has been found to decrease the effective transport properties and kinetics of the electrode [20, 23]. The extent of dissolution in different positive electrode materials was compared by Choi and Manthiram [18], and amount of Mn dissolution is 16 times greater in $LiMn_2O_4$ compared to NCM electrodes. They also reported that structural stability is directly related to the extent of dissolution in electrodes [18].

Dissolution may also cause a decrease in cell capacity by increased growth and breakdown of the SEI [21, 22] on the negative electrode. Although dissolution has been studied extensively in spinel electrode materials and its negative effects on cell capacity have been well established, how dissolution affects the growth of the solid electrolyte interphase (SEI) layer is not well-understood. The exact mechanism by which cell degradation occurs due to dissolution in NCM positive electrodes is under debate. Proposed mechanisms for dissolution include disproportionation reaction [17, 24] and acid corrosion starting from trace moisture present in the electrolytes [18, 25, 26]. Transition metal ions resulting from dissolution diffuse across the separator and are reduced on the negative electrode [4, 16, 19, 21, 27-33]. Since the growth of the SEI on negative electrodes is one

of the major factors leading to capacity fade in Li-ion batteries, it is important to understand the effect of metal dissolution on the properties of the SEI [21, 22, 34-41]. Understanding the changes occurring in the electrodes and the associated effect on the electrochemical performance of the cell is important in assessing the long-term behavior of these materials. Most of the reports in this area have been conducted in half cells [15, 18, 27, 31]. Although half-cell studies are helpful and provide valuable information about the electrochemical properties of the electrode material, they do not provide true estimates of capacity fade for practical applications. Electrode and cell performance varies significantly in full cells compared to those of half-cells. For that purpose, full cell studies with a practical negative electrode materials like graphite are necessary [42]. Because dissolution is a slow process in NCM, alternative methods are sought to assess the long-term effects of metal dissolution on cell performance.

In this work, the effects of metal dissolution on full cells employing NCM positive electrode and graphite negative electrode were accelerated. Multiple authors have reported dissolution of all transition metal species in NCM positive electrodes [4, 16, 18, 32]. In order to understand the effects of dissolution on the SEI and capacity fade, transition metal salts representing the metal species in NCM electrodes were added in the electrolyte to accelerate the degradation processes that may follow because of the dissolution. In this study, collective effects of all dissolved ions (Ni, Co, Mn) on the SEI formed in a full cell were investigated. Although all transition metal ions may have a similar effect on degradation and on the SEI, a separate study examining the effects of individual ions is warranted to understand it fully. Changes in electrochemical performance of full cells due to the effect of metal dissolution and the effect of dissolved metal ions on the SEI are

presented. Based on the findings, a possible mechanism for capacity fade due to dissolution is discussed.

4.2 Experimental methods

4.2.1 Electrode Preparation and Cell Fabrication

Coin cells in 2032 configuration were assembled in the lab to study the effect of transition metal dissolution in NCM positive electrodes. The positive electrode consisted of $Li_{1.05}Ni_{1/3}Co_{1/3}Mn_{1/3}O_2$ (NCM, *NM- 3100, Toda America*), carbon black (CB, *Super C65, TIMCAL*), graphite (*KS 6L, TIMCAL*), and polyvinylidene fluoride (PVDF) binder (*Kureha-7305, Kureha America*). PVDF was dissolved in N-methyl-2-pyrrolidone (NMP) and consisted of 5% of solution (by weight). The composition of these electrodes was 87% (NCM), 5% (CB), 3% (graphite), and 5% (PVDF) by weight. The positive electrodes used in the cells were made in our laboratory. The negative graphite electrodes were commercial (MTI Corporation). The separator was a trilayer polyethylene/polypropylene membrane (*Celgard 2325*). The electrolyte contained 1M $LiPF_6$ in ethylene carbonate (EC): diethylene carbonate (DEC) (1:1 by wt.%) (Novolyte). In order to simulate the metal dissolution that may occur in NCM positive electrodes, transition metal salts were added to the electrolyte. Powders of thermally stable nickel(II) Bis(trifluoromethanesulfonyl)imide $(Ni(TFSI)_2)$, cobalt(II) Bis(trifluoromethanesulfonyl)imide $(Co(TFSI)_2)$, and manganese(II) Bis(trifluoromethanesulfonyl)imide $(Mn(TFSI)_2)$ (Solvionic) salts were dissolved in the electrolyte so that the concentration of each metal cation was 10 mM (a 30 mM total metal

concentration), referred to here as NMC salt. The counter anion TFSI is normally used in ionic liquid electrolytes in lithium ion batteries. At high concentrations of organic solvents such as EC and DEC, electrolyte systems with TFSI anion depict similar transport properties and cyclability compared to organic electrolytes [43]. A high concentration of dissolved transition metals was chosen in order to accelerate the degradation process, as mentioned earlier. Carrying out a similar study with lower concentrations of transition metal ions may be helpful in the future to understand and correlate the extent of transition metal dissolved to the capacity fade. In this accelerated degradation approach, transition metal salts were introduced in the electrolyte before the SEI formation takes place. In a practical cell, dissolution of transition metal occurs slowly and may proceed after formation of SEI is complete. Gowda *et al.* published recent findings and showed that transition metal reduction on graphitic anodes is not affected whether or not an SEI is preformed relative to the introduction of the transition metal ions in the electrolyte [32]. It should be noted that any subsequent dissolution occurring from the positive electrode will not change the concentration of the electrolyte significantly because a relatively high concentration of transition metal salts were added into the electrolyte.

For fabrication of the positive electrode, a slurry was prepared by mixing the active material (NCM), carbon black, and the binder in weight percentages given above. The mixture was blended by using an ultrasonic liquid processor (*Sonicator 3000, Misonix*) for 30 minutes. The slurry was mixed manually with a spatula after 15 minutes of sonication and after the sonication was complete. Next, it was stirred by using a magnetic stir bar for another two hours. Using a doctor blade (*AP-99500403, Gardco*), the slurry was cast onto

an aluminum foil current collector placed on a vacuum plate (*DP-201505, Gardco*). Following the casting, the electrode was dried at 120 °C overnight in a vacuum oven.

1.4 cm diameter electrodes were made from the dried cast with an arc punch. Similarly, the separator was made, but slightly larger size (1.6 cm diameter) to prevent contact between the two electrodes. The assembly process was carried out inside an Argon filled glove box. First the negative electrode was placed unto the bottom case and covered by the separator. Then, 150 µL of electrolyte was added and the positive electrode was placed facing the negative electrode. After that, spacers and a spring washer were added and the coin cell was sealed using a crimper. Thus prepared coin cells were left overnight, and electrochemical testing commenced on the following day.

4.2.2 Electrochemical Testing

All cycling tests were performed on an Arbin BT2000 battery cycler (*Arbin Instruments*). Initial formation cycles included 5 charge and discharge cycles at C/10 rate based on the theoretical capacity of the positive electrode. As described in **Chapter 3**, a fully charged cell discharged at a rate of C/10 takes ten hours to complete the discharge. Cells were charged by following a constant current-constant voltage (CC-CV) protocol. The end-of-charge (EOC) voltage limit was 4.2 V. Following galvanostatic charge at C/10 till this EOC voltage was met; cells were then held at 4.2 V until the current dropped to C/20. After each charge and discharge step, there was a rest period of one hour to allow the cells to equilibrate. The discharge was carried out at a rate of C/10. The discharge step continued until EOD voltage limit of 2.75 V was met. After the formation cycles, the useable capacity was determined based on the formation cycle capacity. For long-term

testing, 50 cycles were done at C/2. A complete discharge at the rate of C/2 takes two hours to complete. Finally, 5 cycles were done at C/10 to compare the end of cycle capacity to capacity obtained at the end of formation. Electrochemical impedance spectroscopy (EIS) was performed on cells using a potentiostat/galvanostat (*Model PGSTAT302N, Metrohm-Autolab*) running Nova software. The impedance was carried out in potentiostatic mode at open-circuit potentials on a fully charged cell. The amplitude of the AC signal was set at 5 mV and the frequency ranged from 1 MHz to 10 mHz. Different processes occurring within a cell have different characteristic time-constants that are exhibited at different frequencies. Thus, EIS is conducted over a broad range of frequencies to include all the effects or impedances associated with different cell processes.

4.2.3 Postmortem Analysis

After cycling was completed, the discharged cells (graphite delithiated) were dismantled in a glove box in an argon environment. The graphite electrodes were soaked in dimethyl carbonate (DMC) to remove Li salt and dried out before post-mortem analyses. High Resolution (HR)-SEM (*Hitachi SU8000*) and Focused Ion Beam (FIB)-SEM (*Nova nanolab FEI 200*) were used to investigate the morphology of the negative electrode surface and cross-section of the SEI. X-ray photoelectron spectroscopy (*Kratos XPS*) was used to identify and analyze the surface components of the SEI.

4.3 Results and Discussion

The first voltage profiles for two full cells, one with the standard electrolyte and one with 30 mM NMC salt added to the electrolyte, are shown in charge-discharge curves in **Figure 4-1(a)**. Performance of batteries are typically presented in the form of charge-discharge curves by plotting the change in cell capacity with cell voltage. The abscissa is labeled cell capacity, which during discharging can be thought of as the discharge capacity, and on charging as the charge capacity. After the charge, it is customary to show the discharge capacity of a cell starting from zero. Cells are assembled in the discharged state, and therefore it begins with a charge capacity of zero. The charge capacity increases as charging continues and voltage increases to 4.2 V. After charging is completed, the axis is shifted to zero and discharge capacity is measured starting at zero at fully charged state (4.2 V). The discharge capacity increases with increasing discharge time and reaches the maximum value at the end of discharge (2.75 V). In **Figure 4-1**, during the first cycle, reduced charge and discharge capacities were observed for cells with NMC salt added in the electrolyte. The first cycle irreversible capacity loss for cell with standard electrolyte was 16 %, by comparison the loss was 25 % for the cell where the transition metal salts were added to the electrolyte. Large first-cycle capacity losses were also observed by Tsunekawa *et al.* [28] after soaking the graphite negative electrode in Mn containing salt.

Differential (incremental) capacity curves, dQ/dV, for these cells are compared in **Figure 4-1(b)**. Information about the changes in electrochemical behavior of cells can be gained by comparing the dQ/dV peaks. From the differential capacity curves, the charging peaks shift positively by about 100 mV, corresponding to higher over-potentials for the cell with NMC salt. This shift during charge was only seen for the first cycle. The discharge peaks remain the same for both cells; thus, the shift in peaks during charging cannot be

attributed to ohmic losses in the cell. During discharge, a smaller area under the curve is observed, representing lower capacity for cell with NMC salt. The contributing factor for the shift in dQ/dV curves may be higher overpotentials due to the blockage of intercalation sites by the transition metals reduced on the negative electrode surface. Reduced transition metals on the electrode surface may cover significant areas of the electrode and block lithium intercalation sites. Similarly, changes on the negative electrode surface may be caused by impurities such as water and oxygen in the salt. Reduction of water and oxygen can occur at potentials around 1.5 V (vs. Li/Li^+) in non-aqueous electrolytes, which can cause surface passivation on the negative electrodes [44]. Although caution was used to dehydrate the salt by drying it overnight in a vacuum oven at 120 °C, there may still be trace moisture present in the salt while transferring the salt into the glovebox from the vacuum oven.

The surface of the electrode is changed due to the reduced species and a larger overpotential is required to complete the charge-transfer process at the negative electrode. Lithium ions on the electrode surface may have to take more tortuous paths to circumvent the reduced transition metal, which may cause an additional diffusional resistance and increased overpotential.
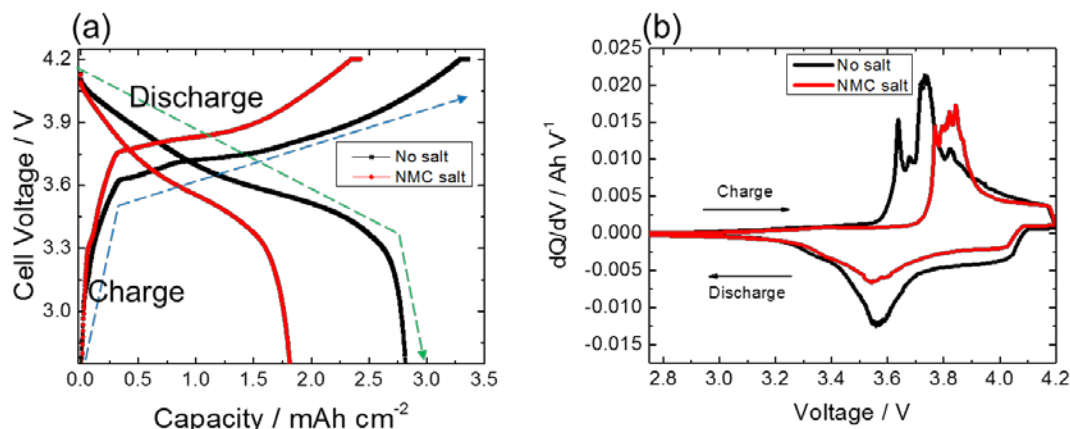
Figure 4-1. (a) First cycle charge and discharge capacities of a full cell comparing the effects of NMCsalt addition to the electrolyte, **(b)** Differential capacity curve of a full cell during first cycle charged and discharged between 2.75V and 4.2V at C/10.

Cell capacities and coulombic efficiencies are compared in **Figure 4-2**. The cells were cycled between 2.75 V and 4.2 V at C/10 rate for the first 5 cycles. The addition of 30 mM NMC salt in the electrolyte resulted in a loss of 30 % of initial capacity measured at the end of the formation period, whereas the control cell lost only 4 % of its formation-period capacity. Fluctuations in the overall capacity with cycling were caused by small temperature variations in the room. After 50 cycles at C/2, the rate was reduced to C/10 and 96 % of the initial capacity for cell with no salt additives was available at the end of the cycling period. The loss of reversible capacity at low rate (C/10) can be attributed mostly to the loss of cyclable lithium in the cell as reduction products in the SEI. After 5 cycles at C/10, discharge capacity at high rate (C/2) for the cell with NMC salt was 41 %
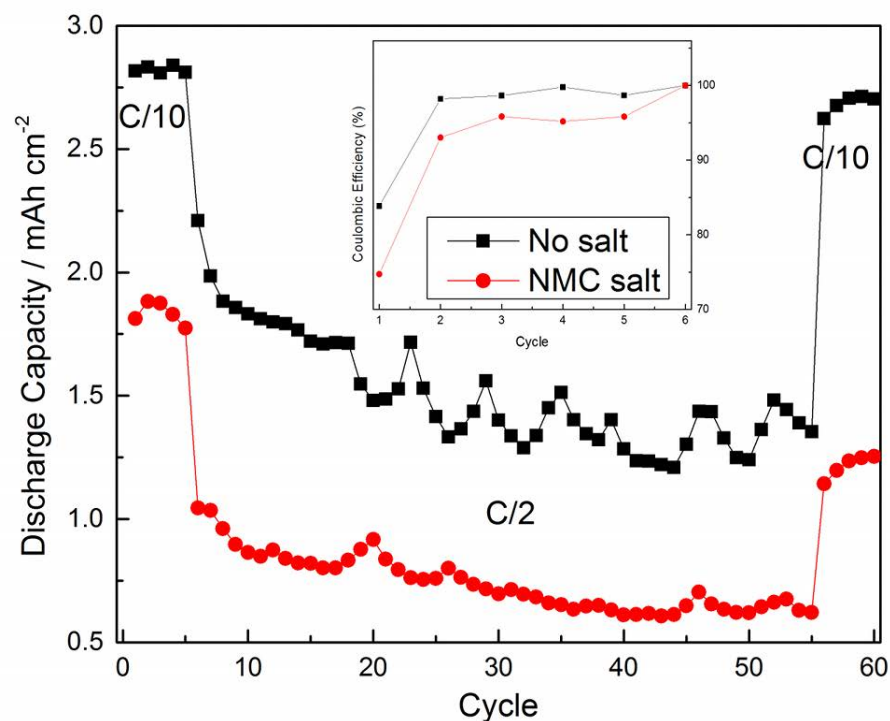
Figure 4-2. Cycling performance of full cells with and without NMC salt additive in the electrolyte. Cycling was done at C/2. First and last 5 cycles were cycled at C/10.

lower than the discharge capacity at low rate. Conversely, for cell with standard electrolyte, the reduction in capacity at high rate compared to low rate was 21 % between cycles 5 and 6. The difference in ohmic drop at C/2 and C/10 is only 8 mV for the NMC salt sample. This was estimated by the change in potential of the cell after the current was applied for the cell at rest period following the charge step. The ohmic resistance alone cannot describe the large drop in discharge capacity between C/10 and C/2. In order to correctly identify the contributing factors for this decrease in capacity at higher rate, charge transfer resistance and diffusional resistance as well as the potential drop across the SEI need to be

considered. Transition metal salts added in the electrolyte caused a significant loss in initial capacity as well as irreversible capacity after cycling. The coulombic efficiency of cell with NMC salt is lower in the first cycle and it stays lower compared to the cell with standard electrolyte. Coulombic efficiency is the ratio of the discharge capacity to the charge capacity for every charge-discharge cycle and is normally expressed in percentage. The coulombic efficiency during a charge discharge cycle of a cell is less than 100 % if lithium is being consumed in side reactions resulting in lower capacity on discharge compared to that on charge. After 3 cycles, the coulombic efficiencies for both cells are constant. Thus, it appears that a relatively stable SEI is formed after a few cycles, but the rate of SEI growth during formation is higher in cells with the added NMC salt.

EIS was performed to identify different contributions to the total cell impedance. Results from an EIS analysis are useful in identifying the solution resistance, SEI resistance, charge-transfer resistance, and mass-transfer resistance in the solid phases of the porous electrodes. EIS results are normally shown using a Nyquist plot containing the real part of the total impedance (-Z') on the horizontal (x) axis and the imaginary part of the total impedance (Z'') on the vertical (y) axis. The frequency response in a Nyquist plot typically contains a high-frequency intercept recognized as the solution resistance, a semi-circle at high frequencies ascribed to the surface layer or SEI impedance, a semicircle at middle frequencies attributed to the charge-transfer impedance, and an inclined line at low frequencies associated with diffusion processes in the porous electrodes [42, 45, 46]. Comparing the impedance spectra after the formation period in **Figure 4-3(a)**, a larger semi-circle at high frequency for NMC salt sample was observed. Assignments of different impedance contributions to the total cell impedance were based on previous results in the

literature for similar impedance spectra for lithium-ion batteries [42, 45, 46]. The first semi-circle at the high frequency was assigned to the SEI resistance. The second semi-circle at middle frequencies was assigned to the charge-transfer resistance. The diameter of the semi-circle at high frequencies and the diameter of the semi-circle at middle frequencies were larger for the cell containing NMC salt. Corresponding to the larger diameter semi-circles, the charge-transfer resistance as well as the SEI resistance were both higher, according to our analysis. A similar trend was seen on the impedance spectra for the cycled cells in **Figure 4-3(b)**. After cycling, there were increases in the diameter of the semi-circle related to the SEI resistance as well as the diameter of the semi-circle related to the charge transfer for both cells. As observed from the diameter of the semi-circles at high frequencies and the diameter of the semi-circles at middle frequencies, the increases in resistances for NMC salt cell were much larger again compared to the EIS from the cells with the standard electrolyte.
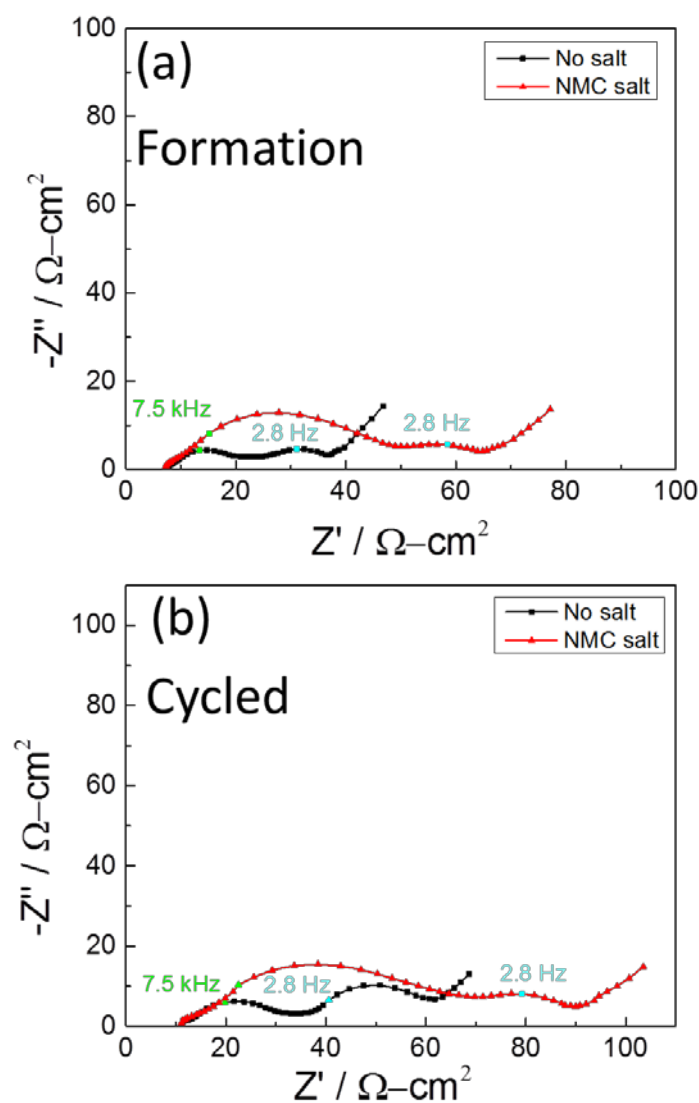
Figure 4-3. Nyquist plots of fully charged cells after **(a)** formation period and **(b)** after cycling.

Postmortem SEM analysis was carried out to examine the changes in the surface morphology of the electrodes. SEM images were taken at different locations in the electrodes to characterize the changes occurring throughout the electrodes. The positive electrode surface did not show any changes after cycling, and the results are not included

here. The cells were cycled for 60 cycles at room temperature. Therefore, surface modifications on the positive electrode due to dissolution are expected to be low in NCM [18]. **Figure 4-4 (a)** shows the SEM images of a pristine graphite electrode. SEM images of graphite electrodes harvested from cycled full cells with standard electrolyte and with NMC salt added in the electrolyte are shown in **Figures 4-4(b) and 4-4(c)** respectively. In both cases, graphite electrode samples from
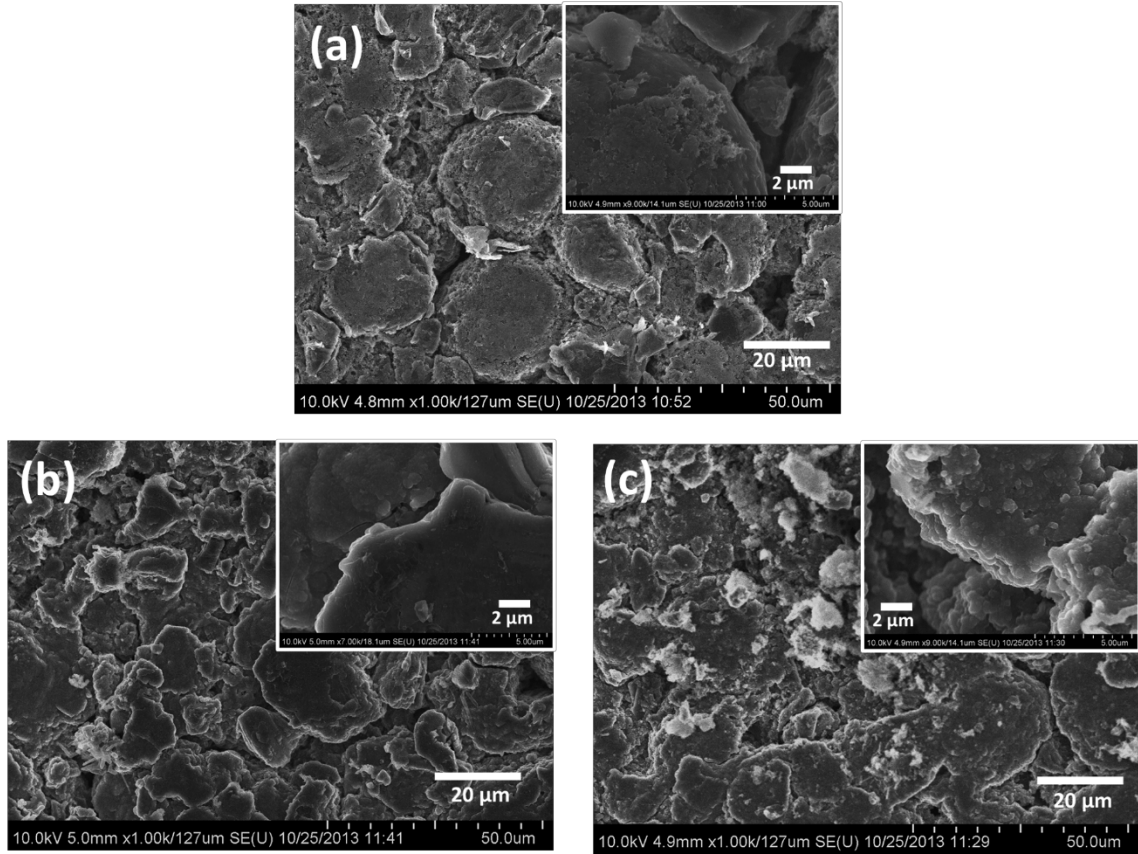
Figure 4-4. HR-SEM surface morphologies of graphite electrode from **(a)** pristine electrode **(b)** full cell with no transition metal salt after cycling **(c)** full cell with transition metal salt after cycling.

cycled cells show a bright layer around the edges of the electrode particles. The lower conductivity of the surface layers compared to the bulk graphite particles leads to an

appearance of bright layer around graphite particles. This bright layer surrounding the cycled graphite electrode particles is normally seen on the negative electrodes and is believed to be the SEI [42]. When transition metals were added to the electrolyte in **Figure 4-4 (c)**, noticeably higher surface roughness of the electrode as well as large agglomerates of a bright oxide layer non-uniformly distributed throughout the graphite electrode were seen. These agglomerates were irregular in size and varied from nano-sized up to 11 µm. Since the composition of these agglomerates is not verified, it is referred to as SEI-like particles. These SEI-like particles were absent in other electrode samples. These particles may be formed due to the growth in inorganic component of the SEI resulting from the transition metal ions reacting with other SEI components and with solvent molecules in the electrolyte.

The electrode surfaces were cut with rectangular shapes (~10 x 5 x 5 µm) by a focused ion beam (FIB) and the inside cross-section was observed using a SEM. Cross-sectional images of graphite electrodes from full cells provide a better idea about the relative thicknesses of the SEI-like surface layer. Conductivity differences between the surface layers and the graphite active materials help in estimating the relative thicknesses of the surface layers formed on the graphite particles. Cross-sections were taken for the graphite particles at different locations in the negative electrode to verify the morphological

changes occurring in the cycled electrodes. **Figures 4-5 (a)** and **4-5(b)**
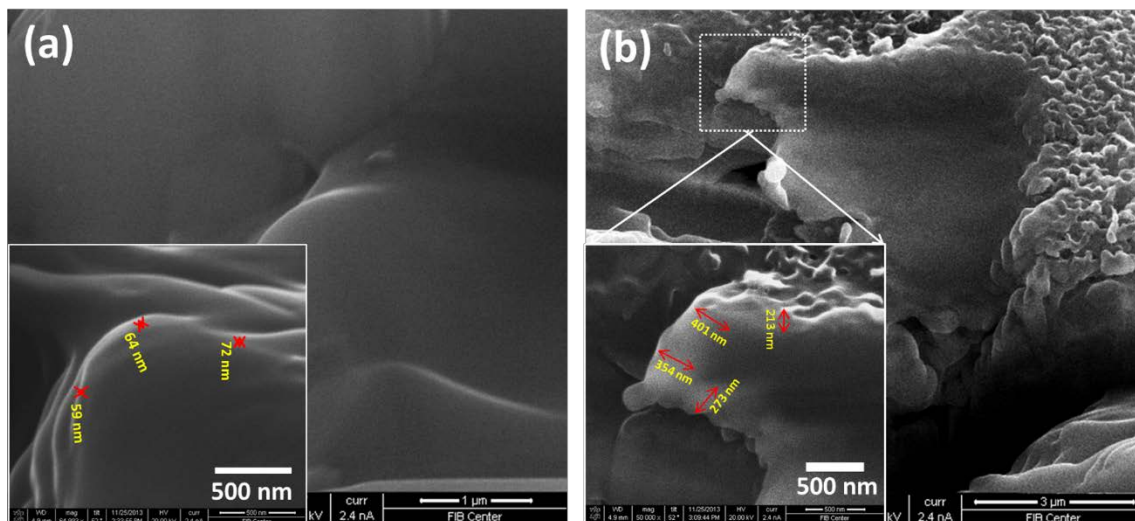
Figure 4-5. FIB-SEM cross-sectional images of graphite electrodes after cycling from full cells **(a)** with standard electrolyte and **(b)** with transition metal salts added in the electrolyte.

show FIB-SEM cross-section images of the graphite electrodes from full cells after cycling. The surface layer thickness on the graphite electrode with standard electrolyte in **Figure 4-5 (a)** was uniform and it varied from 60 nm to 70 nm. In contrast, the surface layer thickness with transition metal salts added in the electrolyte in **Figure 4-5 (b)** was irregular and much thicker, varying from 200 nm to 400 nm. Transition metal salts added to the electrolyte appear to have significantly accelerated the growth of the SEI in the negative electrode in the full cell. It is evident from comparisons of SEM and FIB-SEM images that transition metals in the electrolyte not only contribute to the growth of a non-uniform SEI throughout the electrode but also to a thicker SEI.

Figure 4-6 shows the XPS spectra from the graphite electrodes. All electrode samples showed a peak in the region of 284.8 eV for graphite and a peak in the region of

289 eV for PVDF. The XPS was not coupled with sputtering and the analysis and peak assignments for all species were done based on relevant literature available [47-53]. A peak in the region of 285.8 eV was assigned to the sp^2 hybridized carbon. The observation of a peak around 286.5 eV in all samples is due to the C-O group. In case of fresh electrode samples, this contribution is likely due to oxidation of carbon black used as an additive in the electrode. In cycled electrode samples, presence of this peak suggests that organic components of the SEI like polyethylene oxide (PEO) and other polymeric species were present. Similarly, a peak around 289.5 eV was identified which was attributed to lithium alkyl carbonates ($ROCO_2Li$). Lithium ethylene dicarbonate ($(CH_2OCO_2Li)_2$) is known to be one of the major constituents of the SEI formed in systems containing EC in electrolytes [47, 48]. Along with these organic SEI components, in the case of electrode samples with transition metal salts in the electrolyte, another peak around 290 eV was observed. This peak was assigned to Li_2CO_3 which constitutes the inorganic components of the SEI. The addition of transition metal in the electrolyte likely caused an increase in the inorganic

components   of   the   SEI.
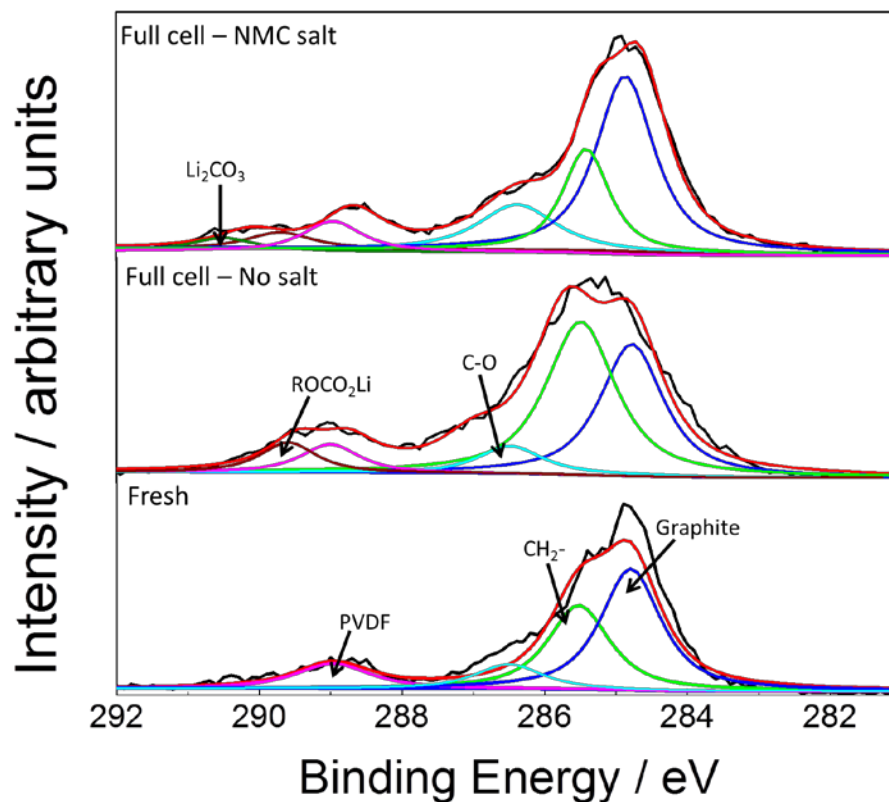
Figure 4-6. C 1s XPS spectra for graphite electrode from a fresh graphite electrode and cycled graphite electrodes harvested from full cells and half cells with and without transition metal salts added in the electrolyte.

Results presented here show that transition metal salts in the electrolyte cause a significant loss in capacity in full cells. Capacity fade is caused by a number of mechanisms that are often coupled. The exact nature of the capacity fade is unclear. Adding transition metals to the electrolyte to accelerate capacity fade, as used in this report, helps focus on dissolution as a cause of capacity fade. Based on our experimental observations and

relevant literature in this area, we present a discussion to understand the effects of the dissolved transition metal salts on the nature of the SEI and its growth.

Transitional metal ions present in the electrolyte would diffuse to the negative electrode. There is no question that these transition metals accumulate at the negative electrode [16, 30, 32, 33]; however, the valence of these metals has been disputed. Because their standard potentials are more positive than lithium, these metals are expected to be reduced on the negative electrode surface. Recently two different groups at Argonne National Lab and Oak Ridge National Lab presented compelling evidence that the Mn from the positive electrodes is metallic Mn (Mn^0) [32, 33]. These results are useful in elucidating the increased rates of capacity fade and increased resistance ascribed to the SEI.

One hypothesis for explaining increased degradation is the increased loss of lithium in the SEI in the negative electrode. For the first cycle, the irreversible capacity loss of the cell with NCM salt in the electrolyte is more than 25 %. Most of the capacity loss during the formation cycles is related to the SEI formation [41]. The total amount of lithium available for cycling is fixed by the lithium content of the positive electrode when the cell is assembled. As more cyclable lithium is lost to the SEI, the total lithium available in the cell for charge and discharge decreases. A large lithium loss causes the NCM electrode to operate at a more delithiated state and at higher potential. The lithium content of the negative electrode increases due to the accumulation of lithium in the SEI. Thus, for the same cell potential, the positive electrode operates at a more delithiated state and at a higher potential.

The reduction of a transition metal ion on the surface of the graphite electrode is accompanied by the deintercalation of two Li^+ from the graphite electrode. The reduction

reaction of transition metal ions in the negative electrode proceeds by a transition metal (M^{2+}) – Li^+ exchange mechanism [28].

$$yM^{2+} + Li_xC_6 \rightarrow yM + Li_{x-2y}C_6 + 2yLi^+ \qquad [4\text{-}1]$$
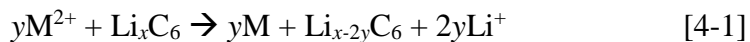
As reduction of dissolved transition metal ions on the graphite electrode proceeds, the subsequent loss of Li^+ from the graphite electrode leads to a capacity loss of the cell. If all of the added transition metal in the electrolyte (10×10^{-3} mol each, 150×10^{-6} L) are reduced ($M^{2+} + 2e^- \rightarrow M^0$) on the negative electrode, 9×10^{-6} mol Li^+ will be deintercalated according to reaction [1]. For the graphite electrode used, total intercalated Li^+ is estimated to be 1.44×10^{-4} mol based on the active material weight of 12.83×10^{-3} g for graphite and 300 mAh/g capacity. From this estimate, the capacity loss of the graphite electrode due to the Li^+ deintercalation from transition metal reduction on its surface can be calculated to be 6.3 %. This value represents a significant capacity loss for the electrode. However, the much higher capacity loss of 30 % measured for cells with transition metal dissolved in the electrolyte cannot be explained by this mechanism alone. In order to understand the increased capacity fade fully, we need to look at the SEI and modifications in the SEI due to transition metals in the electrolyte.

The reduction of electrolyte at the negative electrode and electrolyte interface during the first few cycles helps form the SEI. The electrolyte reduction continues throughout the life of the battery but the rate of growth is greatly diminished after the first few formation cycles. The SEI formed in carbonaceous electrodes is complex in structure. The emerging consensus is that the SEI contains an inner thin dense layer that consists mainly of inorganic reduction products and an outer layer that consists of mainly organic reduction products [47]. The properties and composition of the SEI including the inorganic

and the organic layers vary with the choice of the negative electrode and electrolyte solution. The growth of the SEIs is believed to be controlled by the transport of solvent molecules through the outer porous layer. The outer porous organic layer restricts the transport of solvated Li-ions or solvent molecules but allows for the diffusion of de-solvated Li-ions through the layer after the formation of stable SEI at the end of the formation period.

Experimental evidence presented in literature concerning SEI growth due to transition metals highlight a common observation: presence of transition metal on the negative electrode accelerates the growth of the inorganic components of the SEI [22, 28, 33]. Formation of different metal fluorides and carbonates including LiF and Li_2CO_3 have been reported on the SEI formed on the negative electrode with transition metal present in the electrolyte. In this work, we also identified Li_2CO_3 as a component in the surface layer of the graphite electrode of the cell with transition metal salts added in the electrolyte. Li_2CO_3 was not observed in the sample with standard electrolyte during the postmortem analysis by using XPS. Previous XPS studies coupled with sputtering have shown the presence of Li_2CO_3 well within the SEI [52, 53]. It is also noted in the literature that organic SEI component like $ROCO_2Li$, which is a major reduction product in EC containing electrolytes, undergoes decomposition according to **Reaction [4-4]** noted below to form Li_2CO_3. As this organic reduction product is closer to the surface, the subsequent decomposition reaction is very likely when the electrode sample is being prepared and transferred to the analysis chamber. Thus, although most of the Li_2CO_3 in the SEI is well within the relatively thicker SEI, further decomposition of surface organic products into Li_2CO_3 when the sample is exposed leads to its detection on the surface analysis by XPS.

Although the utmost precaution was taken to avoid exposing the electrode sample to the ambient atmosphere, it is almost impossible to avoid doing so when preparing and transferring the electrode sample for XPS analysis. In EC based electrolytes, $(CH_2OCO_2Li)_2$ is a major solvent reduction product and the solvent reduction reaction proceeds as follows [41]

$$EC + e^- \rightarrow EC^- \qquad [4\text{-}2]$$

$$2EC^- + 2Li^+ \rightarrow (CH_2OCO_2Li)_2 + C_2H_4 \qquad [4\text{-}3]$$
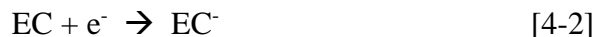
$(CH_2OCO_2Li)_2$ forms a protective layer around graphite active material and protects against further solvent reduction. It forms a porous outer layer and controls the growth of the SEI by limiting the rate of solvent diffusion through this layer. When transition metals are present in the negative electrode, $(CH_2OCO_2Li)_2$ undergoes further decomposition to produce Li_2CO_3 and other inorganic SEI components.

$$(CH_2OCO_2Li)_2 \rightarrow Li_2CO_3 + C_2H_4 + CO_2 + \tfrac{1}{2}O_2 \qquad [4\text{-}4]$$
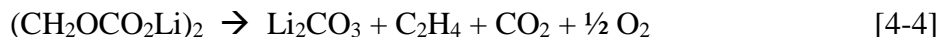
Li_2CO_3 thus produced may react with HF in the electrolyte (formed by the reaction of fluorinated salt with trace H_2O) to give LiF.

$$Li_2CO_3 + 2HF \rightarrow 2LiF + H_2CO_3 \qquad [4\text{-}5]$$

$$LiPF_6 + H_2O \rightarrow LiF + 2HF + POF_3 \qquad [4\text{-}6]$$
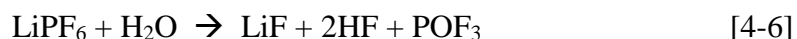
Based on our results and corroborating evidence in literature, we predict that the presence of transition metals in the negative electrode may catalyze the decomposition reactions and promotes the formation of Li_2CO_3 and LiF. The decomposition of $(CH_2OCO_2Li)_2$ leads to an increase in cracks and pores in the SEI. Furthermore, this decomposition leaves an increased surface area of the graphite active material exposed to the electrolyte, which enables solvent reduction to continue. As a result, SEI growth

continues beyond the formation period and contributes to a large capacity fade in cells with continued transition metal dissolution. From our XPS results (**Figure 4-6**) and other literature studies with transition metals in the electrolyte, it is evident that transition metals present on the negative electrode accelerate the formation of inorganic SEI components such as Li_2CO_3 and LiF. Similarly, accelerated growth of the SEI was also observed from our SEM (**Figure 4-4**) and FIB/SEM studies (**Figure 4-5**), which is corroborated by literature studies analyzing the effects of transition metals on the SEI [33]. The growth of the SEI due to transition metal contributes to a large increase in the impedance of a cell. Additionally, the growth of the SEI supported by the transition metal leads to a loss of cyclable lithium within the SEI leading to an increased capacity fade.

SEI growth may occur through electronic conduction through the layer or may be governed by the solvent diffusion. If all of the added transition metal in the electrolyte (10 mM, 150 µL) are reduced ($M^{2+} + 2e^- \rightarrow M^0$) on the negative electrode, 1.62 g/m^2 of metal would be deposited. Using the graphite active material loading (76.6 g/m^2) and BET surface area (4 m^2/g) values for the negative electrode, total area of 4.9 x 10^{-2} m^2 is obtained. For an average SEI thickness of 300 nm in **Figure 4-5 (b)**, the total volume of the SEI was calculated to be 1.5 x 10^{-8} m^3. The weights of reduced metals in the SEI were converted to volumes using tabulated densities. Thus, the total volume fraction of the SEI due to the reduced metal was estimated to be 0.0021. For such a small volume fraction of metal in the SEI, electronic conduction through the layer is highly unlikely. Therefore, SEI growth through solvent diffusion may provide a better explanation.
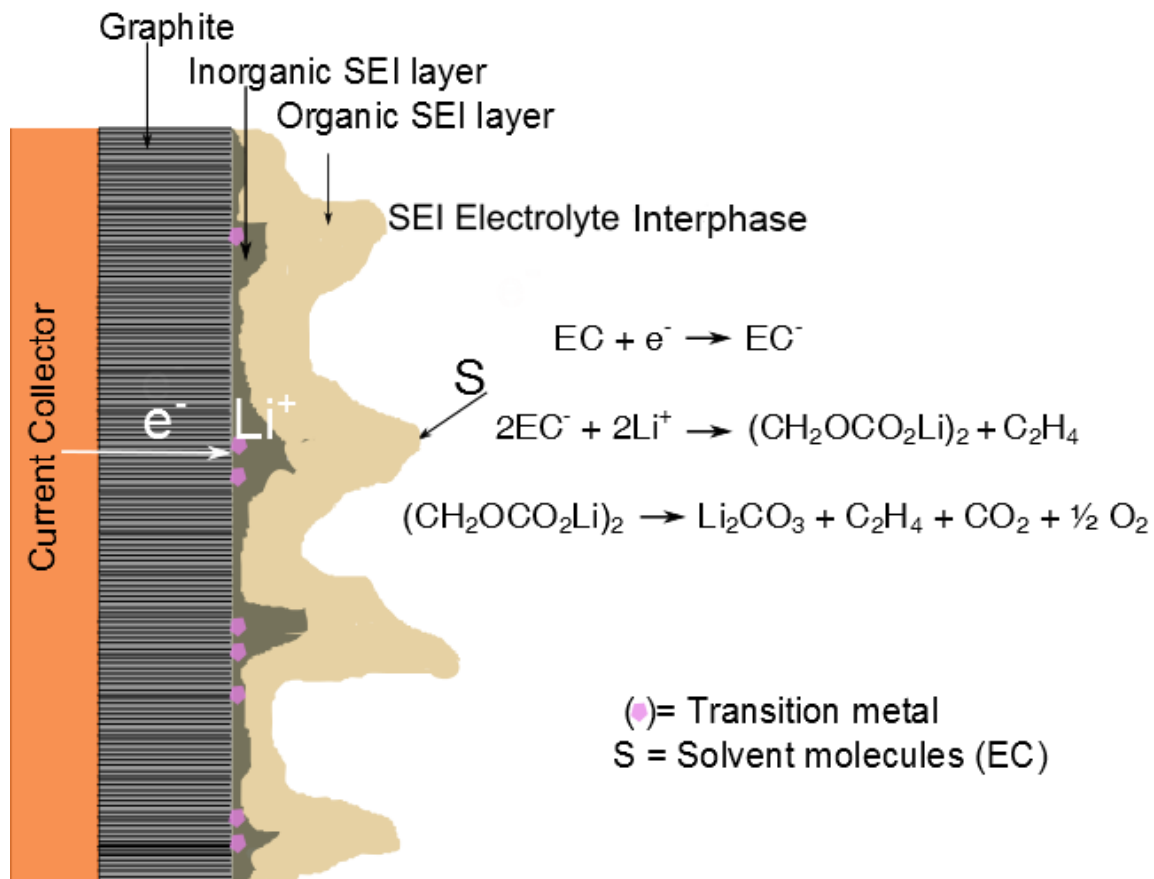
Figure 4-7. Schematic of a negative electrode and electrolyte interface showing the growth of the SEI due to transition metal species present in the electrolyte.

A schematic showing a physical picture of the SEI growth is shown in **Figure 4-7**. Transition metal ions present in the electrolyte diffuse through the SEIs and get reduced on the graphite/SEI interface. Solvent molecules may diffuse through the porous SEIs and get reduced at the graphite active material surface mainly forming lithium alkyl carbonates. Electrons required for this reduction reaction is available through conducting graphite. Li^+ can diffuse through the SEIs. Lithium alkyl carbonates shields the graphite active material surface from further reduction. But, in presence of transition metals, lithium alkyl carbonates undergo further decomposition to form Li_2CO_3 and other inorganic compounds.

The area in the graphite/SEI interface where metal reduction occurs catalyzes this decomposition reaction. Transition metals catalyze this degradation reaction and the organic SEI undergoes morphological changes which cause cracks and pores. The cracks in the SEIs provide a channel for solvent species to diffuse through the layers. As we observed from FIB/SEM results (**Figure 4-5**), the growth of the SEI is non-uniform. Transition metal reduction on the graphite electrode also occurs non-uniformly and the areas in the graphite electrode where metal reduction occurs favor the largest growth in the SEI [33]. As a result, the growth of the SEI due to dissolved transition metals is also not uniform. The regions in the graphite electrode with transition metal reduced accelerate the further growth of the SEI via reduction and subsequent breakdown of solvent species.

4.4 Conclusions

We studied the effects of the transition metal dissolution in full cells employing NCM positive electrodes and graphite negative electrodes by using accelerated testing via addition of transition metal salts in the electrolyte. The addition of transition metal salts in the electrolyte of full cells decreased the capacity and cycleability of the cells. Reduction of transition metal salts in the negative electrode likely caused an increase in the SEI resistance. Post-mortem analysis showed appearance of agglomerates of randomly distributed SEI-like particles throughout the electrode in case of cycled graphite electrode from full cell with transition metal salt added in the electrolyte. Cross-sectional images from FIB-SEM showed up to 4 times thicker SEI for NMC salt sample compared to that with cycled graphite electrode with regular electrolyte. Addition of transition metal species in the electrolyte was shown to facilitate the growth of the SEIs. A mechanism showing

73

the increase in the growth of the SEI as a result of dissolution of transition metal salts in the electrolyte was presented.

4.5 References

1.   Meinshausen, M., et al., *Greenhouse-gas emission targets for limiting global warming to 2 degrees C.* Nature, 2009. **458**(7242): p. 1158-U96.

2.   Whittingham, M.S., *Lithium batteries and cathode materials.* Chemical Reviews, 2004. **104**(10): p. 4271-4301.

3.   Xu, J.T., et al., *Cathode materials for next generation lithium ion batteries.* Nano Energy, 2013. **2**(4): p. 439-442.

4.   Zheng, H.H., et al., *Correlation between dissolution behavior and electrochemical cycling performance for LiNi1/3Co1/3Mn1/3O2-based cells.* Journal of Power Sources, 2012. **207**: p. 134-140.

5.   Tarascon, J.M. and M. Armand, *Issues and challenges facing rechargeable lithium batteries.* Nature, 2001. **414**(6861): p. 359-367.

6.   Wu, S.L., et al., *High Rate Capability of Li(Ni1/3Mn1/3Co1/3)O-2 Electrode for Li-Ion Batteries.* Journal of the Electrochemical Society, 2012. **159**(4): p. A438-A444.

7.   Belharouak, I., et al., *Li(Ni1/3Co1/3Mn1/3)O-2 as a suitable cathode for high power applications.* Journal of Power Sources, 2003. **123**(2): p. 247-252.

8.   He, Y.B., et al., *Preparation and characterization of 18650 Li(Ni1/3Co1/3Mn1/3)O-2/graphite high power batteries.* Journal of Power Sources, 2008. **185**(1): p. 526-533.

9.   Martha, S.K., et al., *A comparative study of electrodes comprising nanometric and submicron particles of LiNi0.50Mn0.50O2, LiNi0.33Mn0.33Co0.33O2, and LiNi0.40Mn0.40Co0.20O2 layered compounds.* Journal of Power Sources, 2009. **189**(1): p. 248-255.

10.   Ellis, B.L., K.T. Lee, and L.F. Nazar, *Positive Electrode Materials for Li-Ion and Li-Batteries.* Chemistry of Materials, 2010. **22**(3): p. 691-714.

11.   Qin, Y., et al., *Electrolyte additive to improve performance of MCMB/LiNi1/3Co1/3Mn1/3O2 Li-ion cell.* Journal of Power Sources, 2010. **195**(19): p. 6888-6892.

12.   Santhanam, R. and B. Rambabu, *High rate cycling performance of Li1.05Ni1/3Co1/3Mn1/3O2 materials prepared by sol-gel and co-precipitation methods for lithium-ion batteries.* Journal of Power Sources, 2010. **195**(13): p. 4313-4317.

13.   Yabuuchi, N. and T. Ohzuku, *Novel lithium insertion material of LiCo1/3Ni1/3Mn1/3O2 for advanced lithium-ion batteries.* Journal of Power Sources, 2003. **119**: p. 171-174.

14.   Wohlfahrt-Mehrens, M., et al., *Study of multi-walled carbon nanotubes for lithium-ion battery electrodes.* Journal of Power Sources, 2011. **196**(6): p. 3303-3309.

15.   Wang, L.F., et al., *Study of mn dissolution from LiMn2O4 spinel electrodes using rotating ring-disk collection experiments.* Journal of the Electrochemical Society, 2003. **150**(7): p. A905-A911.

16.   Abraham, D.P., et al., *Evidence of Transition-Metal Accumulation on Aged Graphite Anodes by SIMS.* Electrochemical and Solid State Letters, 2008. **11**(12): p. A226-A228.

17.   Jang, D.H., Y.J. Shin, and S.M. Oh, *Dissolution of spinel oxides and capacity losses in 4V Li/LixMn2O4 coils.* Journal of the Electrochemical Society, 1996. **143**(7): p. 2204-2211.

18.   Choi, W. and A. Manthiram, *Comparison of metal ion dissolutions from lithium ion battery cathodes.* Journal of the Electrochemical Society, 2006. **153**(9): p. A1760-A1764.

19.   Wang, E., et al., *Stability of lithium ion spinel cells III. Improved life of charged cells.* Journal of the Electrochemical Society, 2000. **147**(11): p. 4023-4028.

20.   Park, J., et al., *Numerical Simulation of the Effect of the Dissolution of LiMn(2)O(4) Particles on Li-Ion Battery Performance.* Electrochemical and Solid State Letters, 2011. **14**(2): p. A14-A18.

21.   Cho, I.H., et al., *Effect of SEI on Capacity Losses of Spinel Lithium Manganese Oxide/Graphite Batteries Stored at 60 degrees C.* Electrochemical and Solid State Letters, 2010. **13**(11): p. A168-A172.

22.   Delacourt, C., et al., *Effect of Manganese Contamination on the Solid-Electrolyte-Interphase Properties in Li-Ion Batteries.* Journal of the Electrochemical Society, 2013. **160**(8): p. A1099-A1107.

23.   Lin, F., et al., *Surface reconstruction and chemical evolution of stoichiometric layered cathode materials for lithium-ion batteries.* Nat Commun, 2014. **5**.

24.   Xia, Y.Y. and M. Yoshio, *An investigation of lithium ion insertion into spinel structure Li-Mn-O compounds.* Journal of the Electrochemical Society, 1996. **143**(3): p. 825-833.

25.   Wohlfahrt-Mehrens, M., C. Vogler, and J. Garche, *Aging mechanisms of lithium cathode materials.* Journal of Power Sources, 2004. **127**(1-2): p. 58-64.

26.   Aurbach, D., et al., *Capacity fading of Li(x)Mn(2)O(4) spinel electrodes studied by XRD and electroanalytical techniques.* Journal of Power Sources, 1999. **81**: p. 472-479.

27.   Komaba, S., N. Kumagai, and Y. Kataoka, *Influence of manganese(II), cobalt(II), and nickel(II) additives in electrolyte on performance of graphite anode for lithium-ion batteries.* Electrochimica Acta, 2002. **47**(8): p. 1229-1239.

28.   Tsunekawa, H., et al., *Capacity fading of graphite electrodes due to the deposition of manganese ions on them in Li-ion batteries.* Journal of the Electrochemical Society, 2002. **149**(10): p. A1326-A1331.

29.   Komaba, S., et al., *Impact of 2-vinylpyridine as electrolyte additive on surface and electrochemistry of graphite for C/LiMn2O4 Li-ion cells.* Journal of the Electrochemical Society, 2005. **152**(5): p. A937-A946.

30.   Tsujikawa, T., et al., *A Study on the Cause of Deterioration in Float-Charged Lithium-Ion Batteries Using LiMn(2)O(4) as a Cathode Active Material.* Journal of the Electrochemical Society, 2011. **158**(3): p. A322-A325.

31.   Ochida, M., et al., *Influence of Manganese Dissolution on the Degradation of Surface Films on Edge Plane Graphite Negative-Electrodes in Lithium-Ion Batteries.* Journal of the Electrochemical Society, 2012. **159**(7): p. A961-A966.

32.   Gowda, S., et al., *Oxidation State of Cross-over Manganese Species on the Graphite Electrode of Lithium-ion Cells.* Physical Chemistry Chemical Physics, 2014.

33.   Xiao, X., et al., *Unraveling manganese dissolution/deposition mechanisms on the negative electrode in lithium ion batteries.* Physical Chemistry Chemical Physics, 2014.

34.   Ning, G., B. Haran, and B.N. Popov, *Capacity fade study of lithium-ion batteries cycled at high discharge rates.* Journal of Power Sources, 2003. **117**(1-2): p. 160-169.

35.   Spotnitz, R., *Simulation of capacity fade in lithium-ion batteries.* Journal of Power Sources, 2003. **113**(1): p. 72-80.

36.   Kida, Y., et al., *A study on the cycle performance of lithium secondary batteries using lithium nickel-cobalt composite oxide and graphite/coke hybrid carbon.* Electrochimica Acta, 2002. **47**(11): p. 1691-1696.

37.   Zhang, Q. and R.E. White, *Capacity fade analysis of a lithium ion cell.* Journal of Power Sources, 2008. **179**(2): p. 793-798.

38.   Safari, M., et al., *Multimodal Physics-Based Aging Model for Life Prediction of Li-Ion Batteries.* Journal of the Electrochemical Society, 2009. **156**(3): p. A145-A153.

39.   Yang, L., M. Takahashi, and B.F. Wang, *A study on capacity fading of lithium-ion battery with manganese spinel positive electrode during cycling.* Electrochimica Acta, 2006. **51**(16): p. 3228-3234.

40.   Abraham, D.P., et al., *Effect of electrolyte composition on initial cycling and impedance characteristics of lithium-ion cells.* Journal of Power Sources, 2008. **180**(1): p. 612-620.

41.   Arora, P., R.E. White, and M. Doyle, *Capacity fade mechanisms and side reactions in lithium-ion batteries.* Journal of the Electrochemical Society, 1998. **145**(10): p. 3647-3667.

42.   Eom, K., et al., *The design of a Li-ion full cell battery using a nano silicon and nano multi-layer graphene composite anode.* Journal of Power Sources, 2014. **249**(0): p. 118-124.

43.	George, V., *Room Temperature Ionic Liquid Electrolyte for Lithium ion Batteries*. 2015, Georgia Institute of Technology.

44.	Tang, M., et al., *Effect of Graphite Orientation and Lithium Salt on Electronic Passivation of Highly Oriented Pyrolytic Graphite*. Journal of The Electrochemical Society, 2012. **159**(5): p. A634-A641.

45.	Mellgren, N., et al., *Impedance as a tool for investigating aging in lithium-ion porous electrodes*. Journal of the Electrochemical Society, 2008. **155**(4): p. A304-A319.

46.	Zhang, S.S., K. Xu, and T.R. Jow, *Electrochemical impedance study on the low temperature of Li-ion batteries*. Electrochimica Acta, 2004. **49**(7): p. 1057-1061.

47.	Verma, P., P. Maire, and P. Novak, *A review of the features and analyses of the solid electrolyte interphase in Li-ion batteries*. Electrochimica Acta, 2010. **55**(22): p. 6332-6341.

48.	Edstrom, K., et al., *Electrochemically lithiated graphite characterised by photoelectron spectroscopy*. Journal of Power Sources, 2003. **119**: p. 522-527.

49.	Kang, S.H., et al., *Investigating the solid electrolyte interphase using binder-free graphite electrodes*. Journal of Power Sources, 2008. **175**(1): p. 526-532.

50.	Andersson, A.M. and K. Edstrom, *Chemical composition and morphology of the elevated temperature SEI on graphite*. Journal of the Electrochemical Society, 2001. **148**(10): p. A1100-A1109.

51.   Bar-Tow, D., E. Peled, and L. Burstein, *A study of highly oriented pyrolytic graphite as a model for the graphite anode in Li-ion batteries.* Journal of the Electrochemical Society, 1999. **146**(3): p. 824-832.

52.   Lee, J.T., et al., *Comparative study of the solid electrolyte interphase on graphite in full Li-ion battery cells using X-ray photoelectron spectroscopy, secondary ion mass spectrometry, and electron microscopy.* Carbon, 2013. **52**: p. 388-397.

53.   Morigaki, K.-i. and A. Ohta, *Analysis of the surface of lithium in organic electrolyte by atomic force microscopy, Fourier transform infrared spectroscopy and scanning auger electron microscopy.* Journal of Power Sources, 1998. **76**(2): p. 159-166.

CHAPTER 5

INVESTIGATING RESISTANCE INCREASE AND CAPACITY FADE IN COMMERCIAL LITHIUM-ION CELLS FOR HIGH POWER APPLICATIONS

5.1 Introduction

Lithium-ion batteries are increasingly being used in hybrid electric vehicles (HEV), plug-in hybrid vehicles (PHEV), and electric vehicles (EV). For applications requiring long-term use, including vehicular applications, it is essential to understand the long-term performance of the battery. For this understanding, elucidating different degradation mechanisms that affect battery performance becomes paramount. Loss mechanisms responsible for decreased capacity and power capability include side reactions, surface layer formation on the electrodes, active material loss, and increased electronic and ionic resistances [1-11].

The power assist provided by batteries through electrical motors is a highly desirable feature in hybrid-electric vehicles. However, performance loss due to increased power fade in lithium-ion batteries is a serious issue. The power capability decreases with repeated use and aging of the battery. This power fade may occur through many different mechanisms and cell components. Degradation mechanisms may affect cell performance by losses related to active materials, conductive additives, electrolyte, separator, binders, and current collectors. By analyzing the degradation occurring in commercial cells, the contributions and origins of these degradation mechanisms can be accurately identified.

Degradation mechanisms vary depending on the electrode materials used in batteries. Some of the common positive electrode materials used in commercial lithium-ion batteries include $LiCoO_2$, $LiFePO_4$, $LiMn_2O_4$, $LiNi_xCo_yAl_zO_2$, and $LiNi_xCo_yMn_zO_2$ (NCM), and negative electrode materials include graphite, hard carbon, and $Li_4Ti_5O_{12}$. Despite many previous studies, a clear understanding of the degradation mechanisms, their origins, and the effects on long-term cell performance are lacking [2, 3, 12-16].

In this study, commercial cells employing NCM positive electrodes and hard carbon negative electrodes were calendar-aged to isolate the cell components that contributed the most to degradation and to understand the power-fade mechanism. High temperature (75 °C) aging was done to accelerate degradation. Reference electrochemical tests and post-mortem analyses were done to analyze cell performance due to aging and to analyze cell components including electrodes, separator, and electrolyte. Results are presented showing power and capacity fade with aging. Based on this electrochemical and post-mortem analysis, a mechanism for increased cell resistance in a power optimized commercial cell is discussed.

The XPS analysis used in this chapter was contributed by Nox Nitta and KwangSup Eom. Time of flight secondary ion mass spectroscopy (TOF-SIMS) analysis was contributed by Jim Benson. JungTae Lee and KwangSup Eom contributed to the transmission emission microscopy (TEM) analysis.

5.2 Experimental

Commercial lithium-ion prismatic cells (EH4, Blue Energy) with NCM positive electrodes and hard carbon negative electrodes were used in this study. Initially, capacity testing was done by charging and discharging the cell using a constant current of 4.7 A

based on the nominal capacity of 4.7 Ah for the cell, as rated by the manufacturer. The upper and lower voltage limits were set at 4.2 V and 2.4 V respectively. These limits were set following the manufacturer recommendations for the battery. Based on the cell capacity from initial testing, C/5 current was used to determine the state-of-charge (SOC) vs. open-circuit voltage (OCV) curve. This curve is useful to monitor the SOC of the cell based on the cell potential. A SOC of 100 % represents a fully charged cell whereas a SOC of 0 % represents a fully discharged cell. The profile used to derive the SOC-OCV curve for the cells at the beginning of testing is illustrated in **Figure 5-1**. A fully charged cell at 4.2 V (100 % SOC) was discharged using a current of C/5 in 30 min steps. Each discharge step was followed by 2 hour rest period to allow the cell to equilibrate. The steady-state voltage at the end of the rest period was used to build this curve. Each discharge step lowered the SOC of the cell by approximately 10 %. The process continued for 10 discharge and rest steps or until the cell reached the lower voltage limit.
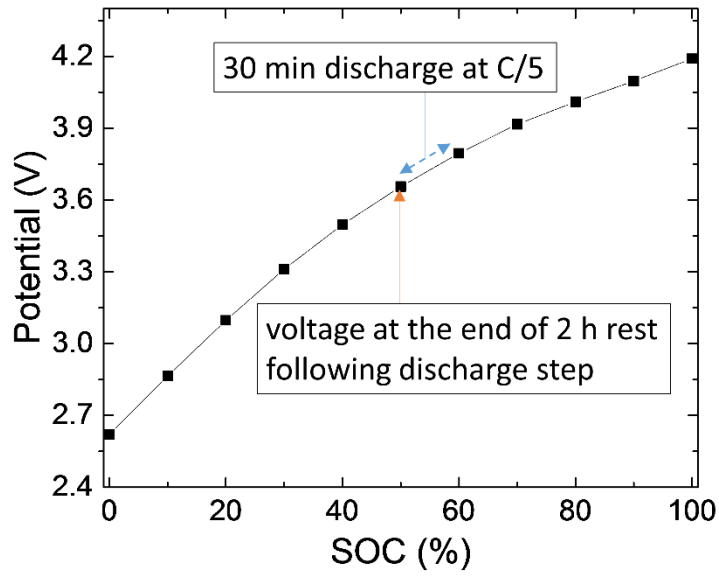
Figure 5-1. SOC-OCV curve for a fresh cell. Fully charged cell at 4.2 V is at 100 % SOC. 30 min discharges are performed at C/5 followed by a 2 h rest.

High temperature aging was accomplished by storing the cells at 75 °C. This test was carried out at a vendor's lab, and the cells were received in our lab after aging was completed for the intended duration. The cells were charged to a voltage corresponding to 90 % SOC (from the SOC-OCV curve) and stored in an environmental chamber. The capacity and resistance of the cells were measured every 400 hours during the aging process. These reference tests were performed after cooling the cells to 25 °C. Cell capacity was measured by charging the discharging the cell using a constant current at 1C, based on the capacity from initial cell testing. Resistance measurements were performed on the cells at 50 % SOC. Cells were charged to a voltage corresponding to 50 % SOC by following these steps: discharge the cell at 1C to 2.4 V, rest for 30 minutes, charge at 1C to corresponding voltage at 50 % SOC determined from the SOC-OCV curve, hold the

potential until the current drops below 0.05 C and then hold for 30 additional minutes at 50 % SOC before testing. The so called "cell resistance" was measured by charging and discharging the cells at different rates (±1C, 2C, 3C, and 6C) for 30 seconds at 50 % SOC. The profile used to measure the cell resistance during discharge is illustrated in **Figure 5-2**. Starting at 50 % SOC, the cell was discharged using pulse currents at 1C, 2C, 3C, and 6C for 30 seconds. After each discharge step, the cell was recharged at 0.1C until the capacity lost during the discharge step was matched (counting coulombs) to get the cell to the same starting SOC before another discharge pulse. A similar current profile was used to measure the cell resistance during charge. Starting at 50 % SOC, the cell was charged at 1C, 2C, 3C, and 6C for 30 s. After each charge step, cell was discharged at 0.1C until the capacity added to the cell during the charge pulse was matched.
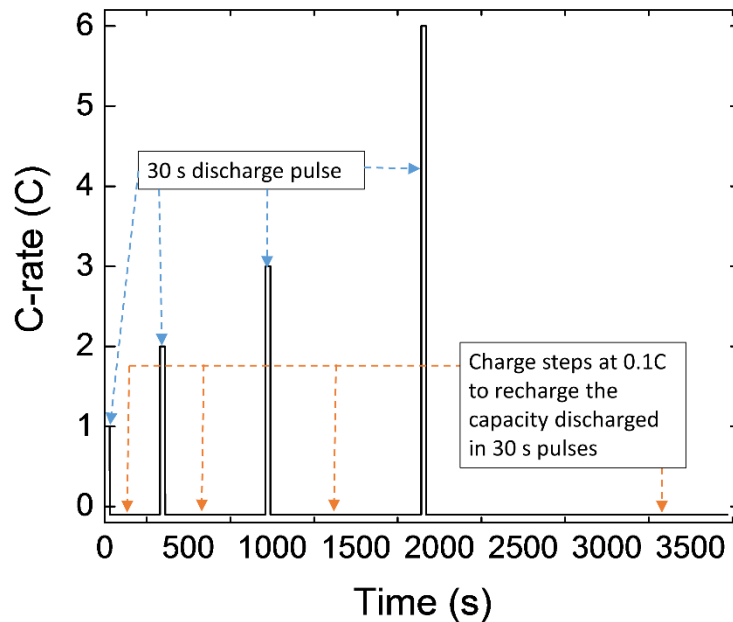
Figure 5-2. Current profiles used to measure the cell resistance during discharge. Cell was discharged using 30 s pulse at 50 % SOC. After each discharge step, capacity lost during

87

the discharge step was recharged using 0.1 C current. To measure the charge resistance, 30 s pulse currents at 1C, 2C, 3C, and 6C were used to charge the cell, followed by discharging the capacity increased during charging step.

Heat generation may occur in lithium-ion batteries when the cell potential deviates from the equilibrium value. Interfacial kinetics, concentration overpotentials, and ohmic losses can lead to deviation from the equilibrium value and heat generation in batteries. These losses are higher at high rates [17, 18]. High internal cell temperature due to heat generation may lead to increased side reactions at the electrode-electrolyte interface, oxygen evolution at the positive electrode, electrolyte evaporation, and melting of the separator membrane. Cell performance degradation and, in worse cases, cell failure and thermal runaway may occur due to excessive heat generation in lithium-ion batteries [17]. As described earlier, the cell used in this study was designed for high power applications; and the 30 s pulse currents at up to 6C for the cell at 25 °C during reference tests should not contribute significantly to cell degradation. Furthermore, since aging for this cell was achieved by soaking the cell at 75 °C, high temperature aging is the primary mode of performance degradation for the cell [17].

The voltage response of a cell with no high temperature aging during discharge at different rates is shown in **Figure 5-3**. Discharges were carried out for the cell at 50 % SOC using 1C, 2C, 3C, and 6C currents for 30 seconds. Resistances for charge and discharge were obtained by using the voltage at 30 seconds from the start of the charge or discharge current and using the slope of the I-V line obtained by this method, as shown in **Figure 5-4**. Thus measured resistance is referred to as "cell resistance" in this thesis and is different from the internal resistance or the ohmic resistance of the cell. When current is flowing in a battery, the resulting voltage is dependent on the open-circuit potentials of the

electrode materials as well as ohmic losses, the charge-transfer overpotentials and concentration overpotentials in the cell. Thus, cell resistance measured by applying current pulses of tens of seconds depends not only on the ohmic losses, but also on the kinetic and mass transfer polarizations.
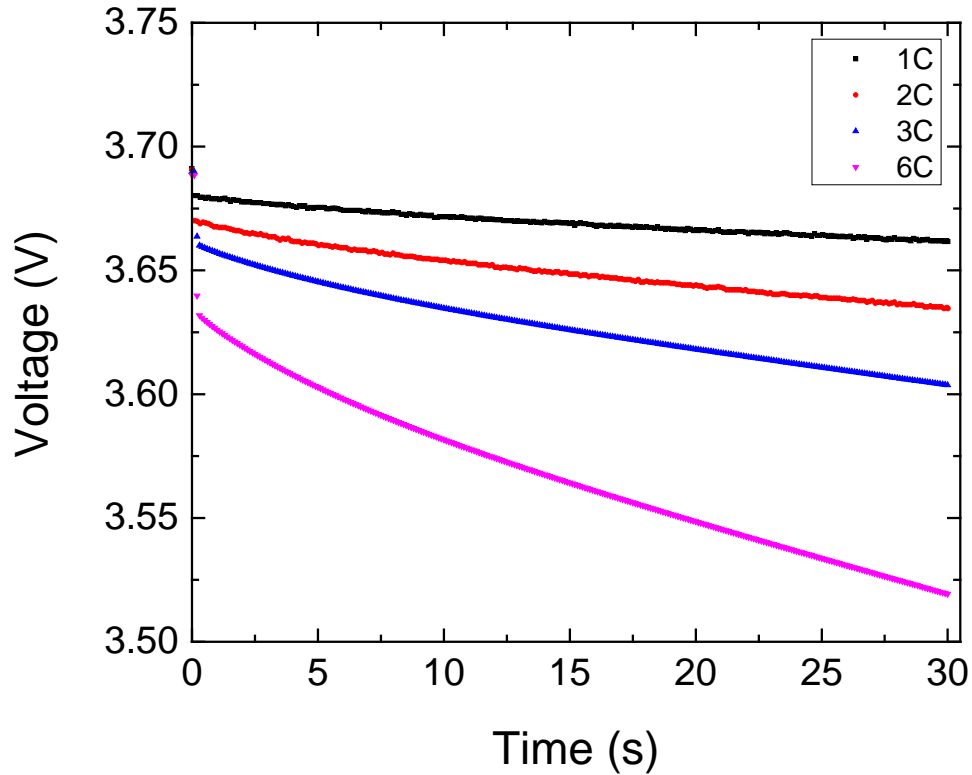
Figure 5-3. The voltage response of a cell during discharge at different C-rates used to measure cell resistance. For this example, data for a cell with no high temperature aging is shown.
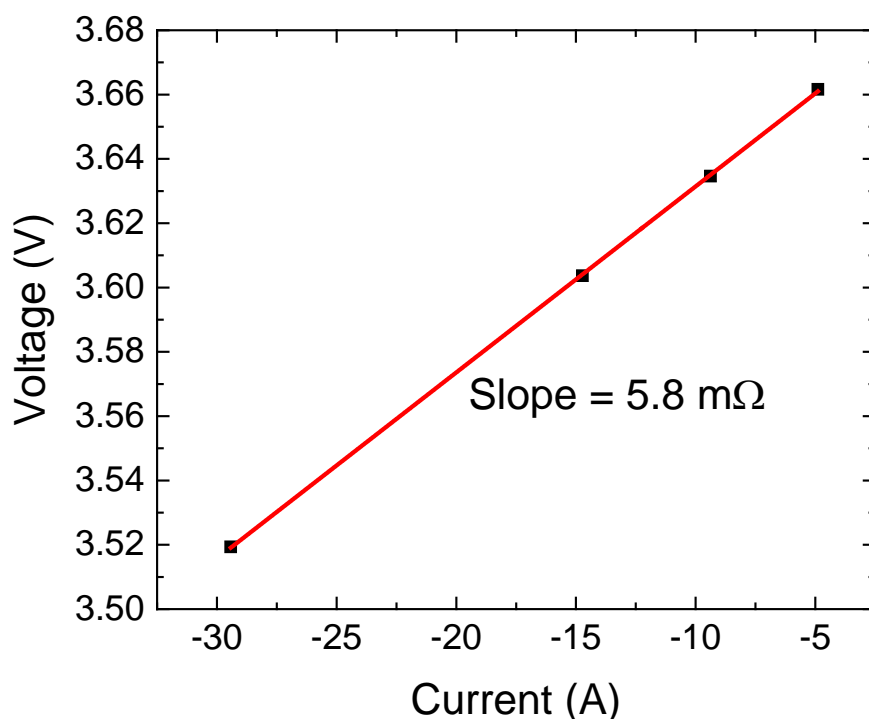
Figure 5-4. Cell resistance determination method- voltage at the end of the 30 s current pulse was used and the slope of the I-V curve was used to determine the cell resistance.

Three cells were taken at different stages of aging for analysis: Fresh cell—cell with no aging, as received from the manufacturer; 1600h cell—cell aged for 1600 hours; 3200h cell—cell aged for 3200 hours.

Post-mortem analysis was done after discharging the cell completely (discharge to 1 mV) and opening under inert (argon) atmosphere in a glovebox. The safety valve on the battery was plucked open with a tweezer to let out any gas build-up in the cell. A chisel and hammer were used to carefully cut around the upper edges of the cell containing the tabs. After the top of the cell was removed, the contents of the cell including the electrolyte, separator, and the electrodes were recovered. Postmortem tests included half-cell capacity

tests for electrodes, electrolyte conductivity tests, x-ray photoelectron spectroscopy (XPS), time of flight secondary ion mass spectroscopy (TOF-SIMS), and transmission electron microscopy (TEM).

The experimental procedures to prepare electrodes in order to fabricate half cells from electrodes recovered from the full cells as well as the experimental procedure to determine conductivity of the electrolyte recovered from these cells were described in **Chapter 3**. In order to estimate the capacity of the half-cells using positive electrode recovered from the full cells, the following procedure was used: (i) constant current charge (0.95 mA—1.5C based on discharge capacity of positive electrode half-cell) until voltage reached 4.2 V, (ii) voltage hold until current dropped below 0.012 mA or total charge time reached 24 hours, (iii) rest period of 10 minutes, (iv) constant current discharge (0.95 mA) until voltage dropped below 2.4 V, (v) rest period of 10 minutes. A similar procedure was used to estimate the capacity of the half-cells using negative electrodes. The cycling procedure used was as follows: (i) constant current discharge (0.95 mA) until voltage dropped below 5 mV, (ii) voltage hold until current dropped below 0.012 mA or total discharge time reached 24 hours, (iii) rest period of 10 minutes, constant current charge (0.95 mA) until voltage reached 1.5 V, (iv) rest period of 10 minutes. The above steps including the voltage limits and currents used to estimate half-cell capacities were prescribed by the manufacturer. These steps were repeated for 3 cycles and the discharge capacity at the end of the third cycle was used to compare the changes in electrode capacity with aging. To prepare electrodes for surface analyses, they were soaked in dimethyl carbonate (DMC) to remove Li salt and were dried at room temperature inside the glovebox. For XPS analysis, a Thermo K Alpha was used with an Al k-alpha X-ray source

91

and 50 eV pass energy for detailed scans and 200 eV pass energy for survey scans. Points were taken at 0.1 eV intervals for 50 ms and repeated 10 times for detailed scans and 2 times for survey scans. A vacuum sealed transfer chamber was used to protect samples from air exposure during sample transfer. TOF-SIMS depth profiling was done using an IONTOF TOF-SIMS 5-300 in positive ion collection using a 25kV Bi^+ primary and 2kV O_2 sputter gun and 150 x 150 μm collection area. Sputter depth was calibrated vs. the time required to sputter through a 200 nm SiO_2 coated Si wafer to avoid depth discrepancies due to different sputter rates between materials. TEM analysis was performed by a Tecnai G2 F30 (FEI, Netherlands) operated at an accelerating voltage of 300 kV. The electrodes were immersed in DMC under inert gas (Ar) and sonicated to be separated from the current collector and dispersed in solvent. Electrode powders dispersed in DMC solvent were drop casted on TEM grids for imaging.

5.3 Results and Discussion

5.3.1 Electrochemical Analysis

The discharge capacity of the fresh cell (as received, after formation period) with no high-temperature aging was measured to be 4.9 Ah. The capacity of the cell aged at 75

°C for 1600 hours was measured to be 4.20 Ah and that for the cell aged for 3200 hours
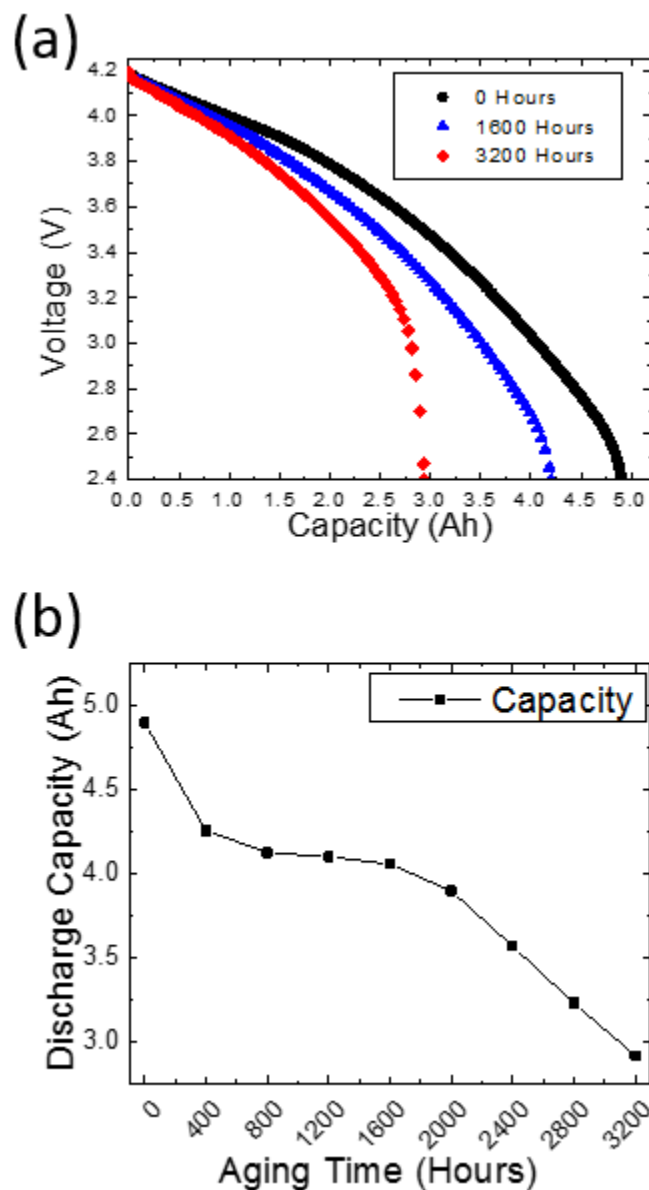
Figure 5-5.(a) Capacity-voltage profiles during 1C discharge for full cells with no high temperature aging, 1600 hours aging, and 3200 aging; **(b)** Decrease in cell capacity with aging.

was measured to be 2.94 Ah. The discharge capacities of the three cells with different degrees of aging are compared in **Figure 5-5(a)**. The decay in capacity with aging at each reference point of 400 hours is shown in **Figure 5-5(b)**. The discharge capacity of the cell decreased 13 % after 1600 hours. After 3200 hours of high-temperature aging, the decrease in discharge capacity was around 40 %.

The voltage profile shown in **Figure 5-5(a)** is governed principally by the open-circuit potential of both electrodes used in the cell. During the passage of current, ohmic, kinetic, and transport losses occur in the cell which results in deviation of the cell voltage from open-circuit or equilibrium values. Ohmic losses occur instantly, kinetic losses occur over a time scale of milliseconds, and noticeable transport losses begin to manifest over longer time scales [19]. When a fully charged cell is discharged, ohmic losses can lead to a drop in potential instantly as current is applied to the cell. When comparing the voltage profiles of the cells at that were aged for different durations in **Figure 5-5(a)**, there is no change in cell potential at the beginning of the discharge. As discharge begins, the voltage profiles for the cells with different aging times overlap. Thus, there is negligible change in the ohmic loss in the cells with increasing aging time. Most significant change in the voltage profiles for the cells with increasing aging times is seen towards the end of the discharge. We will identify the cause for this change in capacity as we continue our discussion.

The capacity fade trend in **Figure 5-5(b)** follows distinct regions of cell degradation with varying slopes: firstly there is a steep slope at the beginning of aging up to 400 hours, followed by a stable region in the middle, and a second steep region after 2000 hours with a larger rate of degradation. The sharp decline in the first 400 hours is most likely due to

the formation of a surface layer on the anode—the solid electrolyte interphase (SEI). The passivating SEI formation leads to irreversible lithium consumption resulting in decreased cell capacity, and is often the dominant mode of degradation in cells [3, 7, 14]. The high temperature used in this aging study as well as the high state-of-charge at storage contribute directly to increased degradation and capacity fade [4, 14]. After 400 hours, the rate of capacity fade decreases, and the cell performance stabilizes. As the SEI is formed, the rate of solvent decomposition to form additional layer and subsequent lithium loss decreases. The increase in the rate of capacity fade after 2000 hours is likely due to a second mechanism or mechanisms along with SEI formation on anode. Previous reports have indicated this sort of two regions for capacity fade [3, 5]. Material loss due to transition metal dissolution is an important degradation mechanism in cells containing transition metal oxides in positive electrodes [8, 14, 16]. The loss mechanism related to this different slope after 2000 hours may be related to material loss from the positive electrodes. As we present subsequent results, we will discuss the different degradation mechanisms and try to identify the mechanisms that explain this capacity fade behavior.
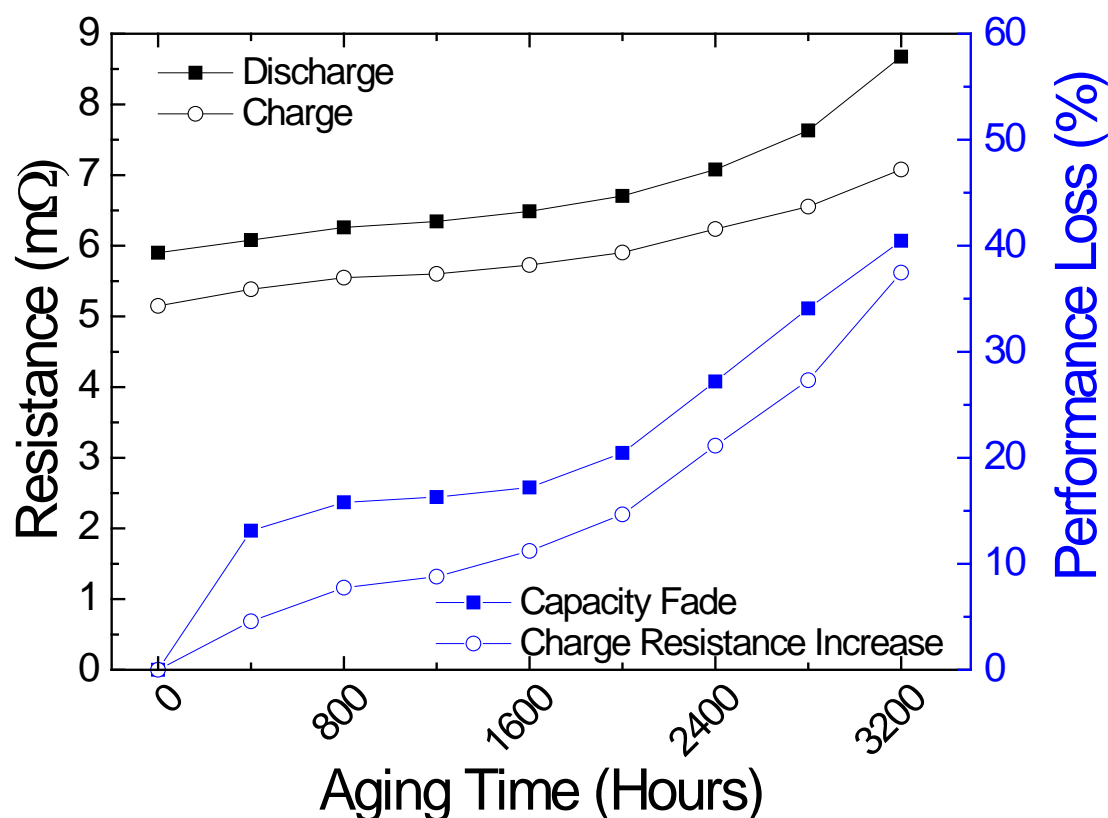
Figure 5-6. Increase in charge and discharge cell resistance with aging (in black) and performance loss from capacity and resistance increase with aging time as a percentage change (in blue).

Cell discharge and charge resistance measured at each reference interval of 400 hours is shown in **Figure 5-6** in black and follows a similar trend for charge and discharge. Cell resistance increases steadily in the beginning of aging up to 2000 hours, after which there is an increased rate of degradation with aging. The trend in cell resistance appears to follow two different regimes: up to 2000 hours, there is gradual increase in cell resistance; after 2000 hours, there is an increased slope representing a larger rate of degradation. Although both resistances were measured at the same state of charge, the discharge resistances are greater than charge resistances. It is likely due to the thermodynamic

properties of the electrodes. The open-circuit potential functions of each electrode dictate the amount of lithium stored in each electrode at fixed potentials and the SOC-OCV relationship for the full cell. The change in voltage is greater for discharge than that for charge for the same amount of current passed at 50 % SOC for the full cell in this study. As a result, the discharge resistance is greater than the charge resistance measured at that state of charge.

The resistance increase and capacity fade with aging seen in **Figure 5-5(b)** and **Figure 5-6** follow the same general behavior: initially, the degradation is slow and after 2000 hours, the rate of degradation increases. There is a sharp decrease in capacity after 400 hours, after which the rate of capacity fade decreases. The resistance increase trend does not show this sharp increase at the beginning of the aging. Despite this difference, the overall trend of the cell performance loss in terms of capacity fade and cell resistance increase is similar. It may be useful to perform reference tests more frequently than 400 hours in order to identify the trends in cell performance loss with aging time. In order to illustrate the similarity in capacity fade behavior and cell resistance increase, both are shown in **Figure 5-6** in blue. From this comparison, the cell capacity fade and resistance increase appear to be closely related and may be explained by similar degradation mechanisms.

Cell resistance was separated into an internal resistance (ohmic) contribution and mass-transfer contribution by attributing the resistance to the initial potential drop when the step change in current is applied (IR contribution) and to the mass-transfer polarization as concentrations build up in the electrodes (MT contribution). Cell resistances in **Figure 5-6** were used to identify IR contribution and MT contribution to total resistance. Voltage

profile during the application of pulse current at 6C was used to determine IR and MT contributions to total cell resistance. The change in voltage response of the cell with increasing aging time during 6C discharge and the procedure used to determine resistance contributions is illustrated in **Figure 5-7**. The IR contribution to total cell resistance was estimated by using the potential difference between the open-circuit potential before the application of charge or discharge current and the first data point after the application of such current. Since data was collected every 100 ms interval, the "IR contribution" thus measured also includes charge transfer polarization. The difference in total cell resistance and IR contribution was used to estimate the MT contribution to total resistance.
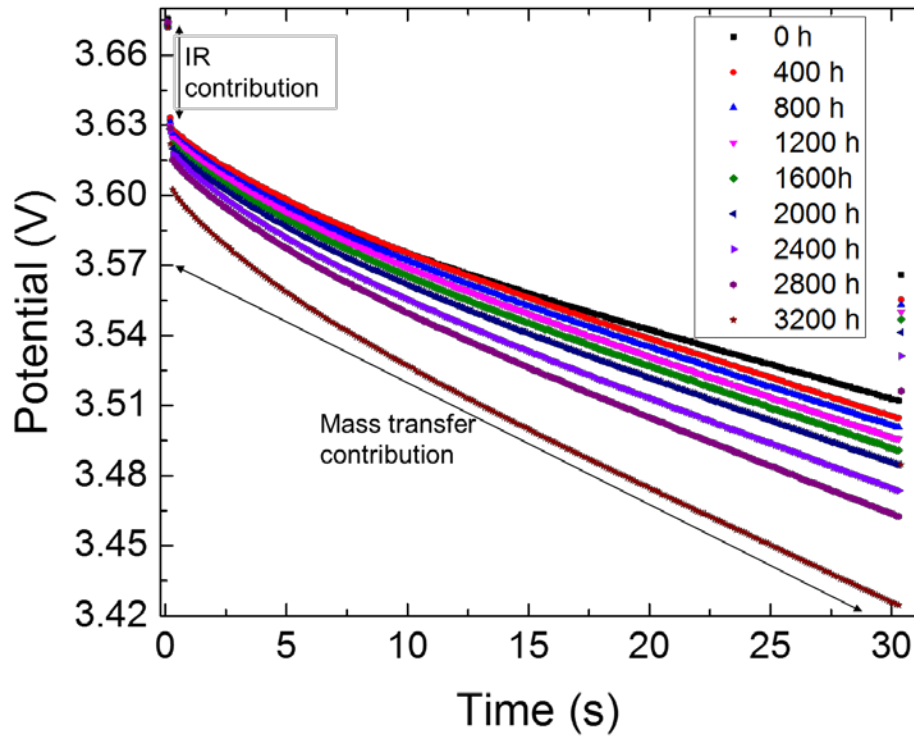
Figure 5-7. Changes in cell potential after applying a discharge current of 6C at 50 % SOC with increasing aging time. Reference tests were carried out at 400 h intervals at 25 °C. Cell resistance was separated into IR and MT contributions as shown.

IR and MT contributions to total resistance are separated and shown in **Figure 5-8**. The cell resistance increase appears to be mostly affected by mass transfer limitations. The IR increase for the cell at the end of the aging at 3200 hours was estimated to be less than 13 % whereas the MT resistance increase was more than 50 % for both charge and discharge. MT resistance increases most rapidly after around 2000 hours and contributes the most to the increase in cell resistance. Similar to the trend in capacity fade, this may be associated with different degradation mechanisms occurring in the cell with increasing aging times. Resistance analysis suggests that the internal resistance alone cannot be attributed to the increase in cell resistance. The changes occurring in the cell with increasing aging time lead to MT transfer limitations occurring in the cell which contributes primarily to the increase in cell resistance.

Mass transfer resistance is present in the negative electrode, the positive electrode, and the electrolyte. In principal, any of these could contribute to the greater "cell resistance" with aging. Next we consider how SEI growth in the negative electrode affects the concentration polarizations in the cell.

The total cyclable lithium in the cell is fixed. As SEI grows with aging, loss of cyclable lithium in the cell to form reduction products in the SEI may lead to both electrodes being operated at more delithiated state at a fixed potential compared to a cell with no cyclable lithium loss. This loss of cyclable lithium may lower the rate of lithium transport in the electrodes causing an increase in cell resistance. The rate of reaction for the charge transfer reaction at the electrode surface is dependent on the concentration of lithium at the electrode surface. The decreased rate of lithium transfer in the electrode

increases concentration polarization and charge transfer polarization in the cell, thus increasing cell resistance.

Another possible cause for increased mass transfer resistance in the cell may be related to the changes occurring in the positive electrode surface. Positive electrodes are also prone to surface layer formation and metal dissolution at high temperatures [6, 20, 21]. These changes on the positive electrode may decrease the diffusivity of lithium ion in the electrode [22]. Thus, transport limitations may occur due to lower lithium diffusivity causing an increase in cell resistance. The sources of performances losses can be understood better by studying the changes in cell impedance and by investigating the changes occurring in the electrodes via post-mortem analysis.
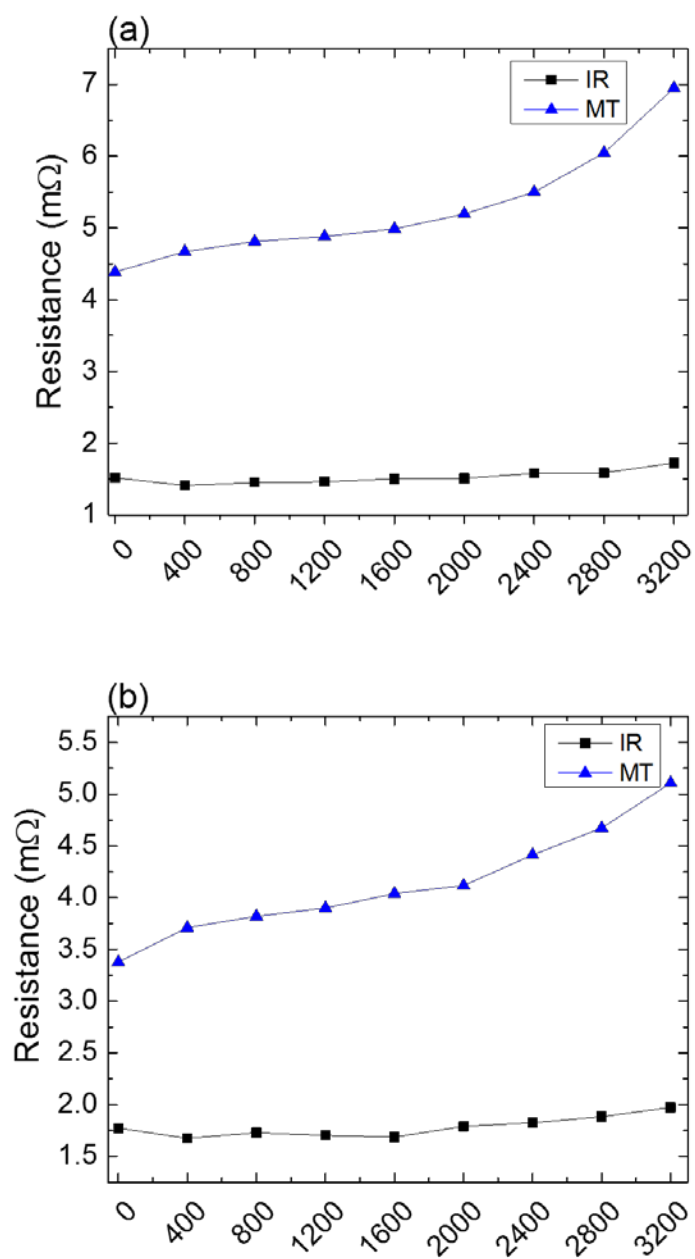
Figure 5-8. IR contributions and MT contributions of the total cell resistance calculated at 50 % SOC. Comparisons are shown for (a) discharge and (b) charge with increasing aging time for the full cell.

Electrochemical impedance spectroscopy (EIS) tests were performed to elucidate physical phenomena that contribution to the total cell impedance. EIS allows separation of different processes based on their characteristic time constants. A typical result is presented in a Nyquist plot containing semi-circles and inclined lines which represent the time constants associated with the different physical processes. The impedance contributions to the total cell impedance were designated based on the literature for similar lithium-ion cells [11, 23, 24]. The impedance response of a lithium-ion porous electrode can contain a semi-circle in the high frequency region, which is associated to surface-layer impedance. Semi-circles at medium frequencies are related to charge-transfer impedance. Diffusion in porous electrodes is represented by an elongated tail at low frequencies. Often, the semi-circles at high frequencies and medium frequencies overlap and are present as a flattened or depressed semi-circle from high to medium frequencies on a Nyquist plot. The comparison of the EIS spectra of cells with different extents of degradations is shown in **Figure 5-9** using a Nyquist plot (top) and a bode plot (bottom). EIS spectra were measured at 4.2 V for each cell to try to understand the contributions of different cell processes, such as internal resistance, charge-transfer resistance, and diffusional resistance.
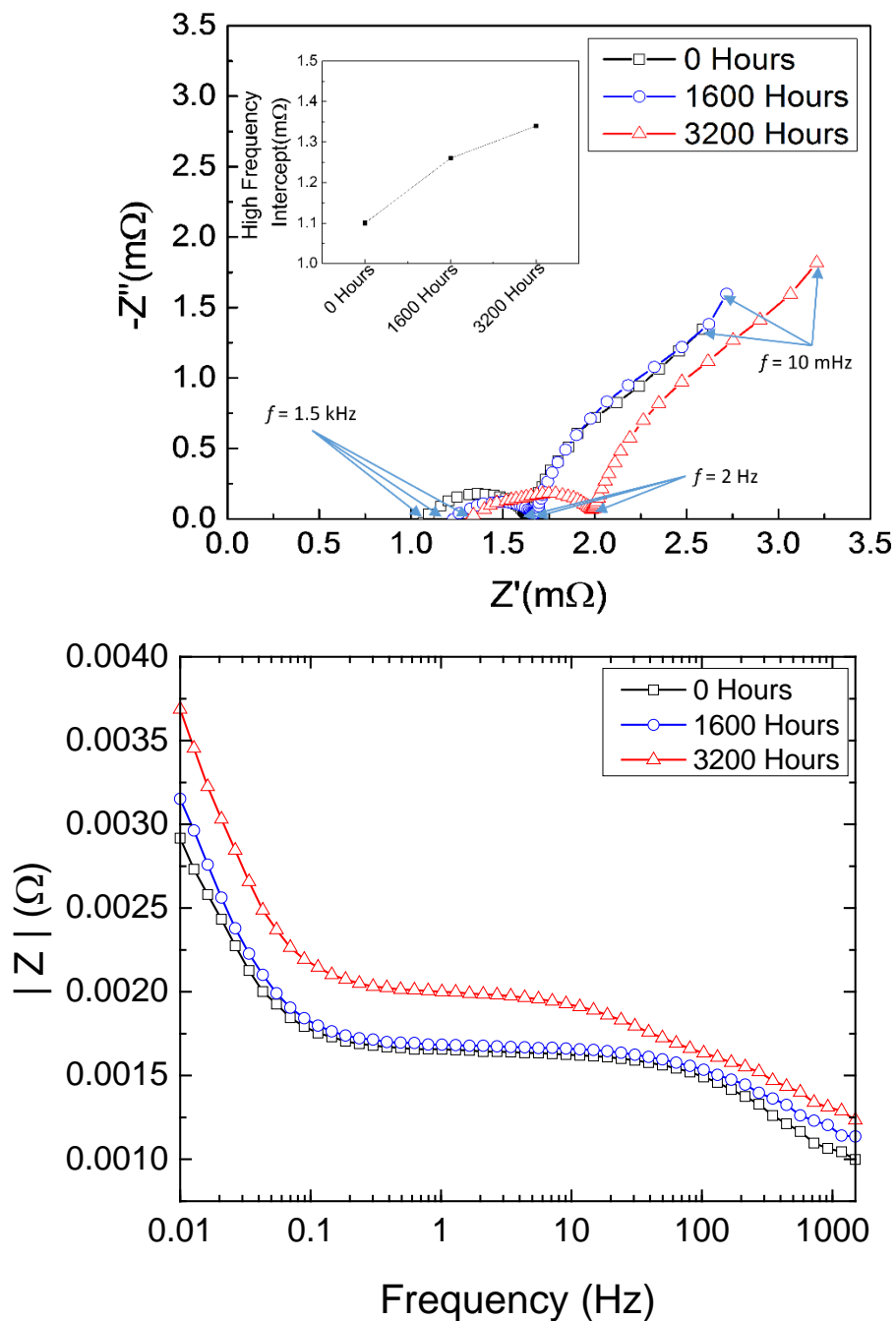
Figure 5-9. Complex plane impedance (Nyquist) plot of full cell showing increase in cell impedance with aging (top); and bode plot showing the magnitude of the cell impedance at different frequencies.

The high-frequency intercept in Nyquist plot in EIS spectra provides the internal resistance of the cell. The main part of this high frequency resistance is the effective

conductivity of the electrolyte. However, this impedance includes all contact resistances including the surface layer resistance and the electronic resistance in the electrode. From comparisons shown in **Figure 5-9**, the high frequency intercepts in the Nyquist plot of the cells follow an increasing trend with the extent of degradation. This increase in impedance is highlighted in the inset in **Figure 5-9**. The ohmic resistances observed from the high-frequency intercept in Nyquist plot were compared to the IR contributions determined earlier in resistance tests using pulse currents. The IR contributions thus measured included charge transfer polarization, as mentioned earlier. Charge transfer polarizations accounted for 20-30 % of the IR contributions measured from pulse current tests after accounting for the ohmic contributions as measured from EIS. Thus, charge transfer polarizations also contribute to the increase in cell resistance. In addition to the changes at high frequency, the tails of the low-frequency region in the impedance spectra are elongated for cells with largest extent of degradation. The increase in diffusional resistance is seen by the rise in Warburg impedance at low frequency region of the EIS. It is apparent from the EIS spectra comparisons that aging correlates with an increase in the high-frequency intercept (internal resistance) and growth in the low-frequency tail in impedance spectra.

5.3.2 Post-Mortem Analysis

The capacities of the half-cells using negative electrode (anode) and positive electrode (cathode) recovered from the full cells are shown in **Figure 5-10**. The electrodes from full cells aged for different hours are represented by different colors. The capacity of the anode half-cell decreases by around 20 % after 1600 hours aging compared to that for the cell that has not been aged at high temperature. The capacity of the cathode half-cell

remains unchanged after 1600 hours. The small increase observed in capacity of the cathode half-cell is likely due to experimental error. For the cells aged for 3200 hours, the capacity of the cathode half-cell decreases by 60 % whereas the capacity of the anode half-cell decreases by 30 % when compared to the half-cell capacity of the electrodes from fresh cells with no high temperature aging. The capacity fade trend for the full cell observed in **Figure 5-5(b)** may be explained further by changes in the capacities of the half cells from the electrodes recovered from full cells. The initial capacity loss of the full cell for up to 2000 hours was likely due to the changes occurring in the negative electrode, whereas the losses occurring in the positive electrode dominated the capacity fade in full cell after 2000 hours. The loss of cell capacity of the full cell during initial stages of aging may be caused by the growth of the SEI on the negative electrode as discussed earlier. The decrease in half-cell capacity of the anode and no change in half-cell capacity of the cathode suggest that this is a highly probable cause for cell capacity fade during the initial stages of aging. The trend of capacity fade of the full cell after 2000 hours aging suggests a different degradation mechanism affecting cell performance during the later stages of aging compared to the initial stages of aging. Large decrease in half cell capacity of the positive electrode from the cell aged for 3200 hours indicates that limitations occurring in the positive electrode may be the significant contributing factor to the performance losses in full cell in the later stages of aging. We will explore this and the changes occurring in the electrodes as we continue our discussion and analysis.
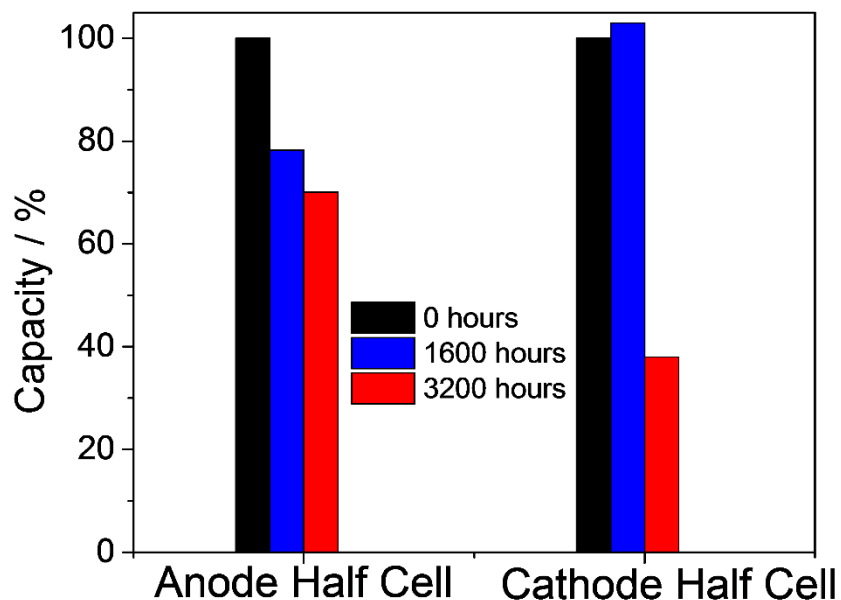
Figure 5-10. Capacities of half cells from the negative electrodes (anode) and positive electrodes (cathode) recovered from full cells after different aging times.

The conductivities of the electrolytes recovered from the cells at different stages of aging were determined by using conductivity cell experiments. The conductivity of the electrolyte from the cell with no high temperature aging was determined to be 8.9 mS/cm. Similarly, the conductivity of the electrolyte from the cell aged for 3200 hours was determined to be 8.6 mS/cm. The electrolyte conductivity remained essentially unchanged (around 3 % changed from 0 hours to 3200 hours). From EIS analysis of full cells, an increasing trend in the internal resistance which includes contributions from solution resistance and surface resistance were observed with increasing aging time. The conductivities of the electrolyte from the cells with different extent of aging suggest that the solution resistance cannot account for the increase in internal resistance in cells with aging. Thus, the increases in the internal resistance are attributed to changes in the negative

and positive electrodes. Surface modification and layer formation on the electrodes is one of the primary causes of resistance increase in electrodes [1]. After ruling out solution resistance increase from conductivity experiments, changes occurring on the surface of the electrodes were analyzed to identify degradation occurring on the electrodes.

The nature of the surface layers formed on the anode and cathode were further inspected using XPS. Detailed chemical information about the electrode surface can be obtained by this technique. Although depth profiling is possible, it changes the chemical structure and is slower than SIMS, so only surface analysis was performed with XPS. **Figure 5-11** shows the C 1s spectra of the negative electrode and the positive electrode recovered from full cells after different stages of aging. Several peaks related to an SEI typically formed on carbonaceous anode were identified. The C 1s spectra for both electrodes generally show broader and stronger peaks, indicating surface layer growth. Based on literature and reference samples, PVDF $\underline{C}$-CF$_2$ and $\underline{C}$-F$_2$ peaks were identified at 286.2 and 290.5 eV respectively and were used to adjust the spectra for charge shifts [25]. Based on the shape of the experimental data obtained, a graphitic sp2 carbon peak was identified at 284.8 eV with full-width-half-max (FWHM) ~ 0.7 eV, while the more general sp3 carbon peak was identified at 285 eV in all electrodes with FWHM the same as the

other
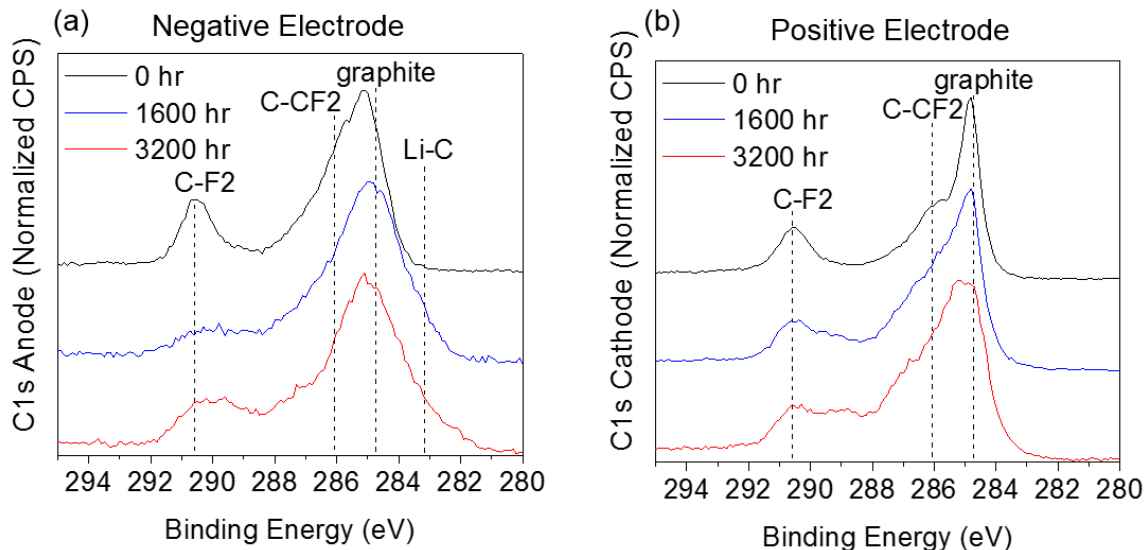
Figure 5-11. C 1s XPS spectra for the (a) negative electrode and (b) positive electrode recovered from full cells with different aging times denoted by color.

C 1s peaks. A good fit could not be achieved without this sharper graphitic peak unless many more Gaussian peaks were added. The anode additionally had a peak identified at ~283.3 eV and assigned to $\underline{C}$-Li, which does not normally appear in a delithiated anode. The most likely explanation is that there is some electrically isolated material due to the growth of a thick SEI. Additional peaks were also identified and assigned using literature data where possible. C 1s peaks for the anode and the cathode are listed in **Table 5-1**. Peaks related to the porous organic layer (e.g.: $ROCO_2Li$) and compact inorganic layer (e.g.: Li_2CO_3) constituting the heterogeneous SEI were identified. As aging proceeds, more and more lithium ends up being trapped in the SEI on the negative electrode resulting in decreased capacity of the cell. Several peaks related to graphitic carbon and binder material show an apparent decrease in composition with aging. With increasing aging, the graphite peak first diminishes and then disappears, followed by a steady decrease in the PVDF $\underline{C}$-

CF$_2$ and $\underline{C}$-F$_2$ peaks. This behavior is likely due to the increasing growth of the SEI on the electrode surface. As the thickness of the surface layer on the electrodes increases, these species are covered and no longer detected by XPS. The fact that this occurs first on the anode shows that the surface layer is thicker on the anode, as expected.

Table 5-1. Percent atomic composition of XPS C1s peaks from anodes and cathodes after the formation cycle (fresh), after 1600 hours, and 3200 hours of aging at 75 ºC.

Approximate BE (eV)	Name	Anode			Cathode		
		Fresh	1600 hr	3200 hr	Fresh	1600 hr	3200 hr
283.3	C1s C-Li	-	2	5	-	-	-
284.8	C1s graphite	1.4	-	-	9.7	5	0
285	C1s C-C sp3	19	9.8	19	12.1	24.1	20.6
286.2	C1s C-CF$_2$	8.3	1.7	0.2	10.8	11	4.5
287.3	C1s C-O$_2$	4.2	2.8	5.4	3.5	4.6	7.4
289	C1s ROCO$_2$Li	1.7	0.9	0.9	1.4	4.1	4
290	C1s Li$_2$CO$_3$	-	0.2	4.8	-	-	-
290.5	C1s C-F$_2$	6.5	1.1	0.2	8.3	7.4	4.5

Depth profile investigations on the positive and negative electrode surface with aging were performed using TOF-SIMS analysis. The sputter rate for depth profile was measured using a SiO$_2$/Si standard. The ion beam etching/sputtering on the composite porous electrode such as NCM does not remove the electrode material uniformly due to the electrode consisting of individual particles with pores rather than a flat thin film. This results in broad elemental distributions in SIMS profiles instead of sharp interfaces. Furthermore, different elements have variable TOF-SIMS sensitivity and detection limits. The ionization efficiency in dynamic SIMS depends on the surface composition and

structure [21]. Thus, the sputter time taken during SIMS analysis of composite porous electrodes may be indicative of not only the true sputter depth or electrode thickness but also of longer sputtering period due to an artifact of the sputtering process.

Results for this analysis on the positive electrode are presented in **Figure 5-12**. The intensities or counts presented in the figures were normalized to one, so that the count at the bulk of the material is one. Presence of surface species related to the SEI formed on graphite negative electrodes were also verified by TOF-SIMS on the negative electrode. Since the SEI formed on the negative electrode was covered in the XPS discussion, it is not repeated here. Species of interest for organic and inorganic SEI compounds were selected based on intensity of the peaks and variation with respect to depth and the strongest peak for each fragment series (Ex: $C_2H_3^+$ *vs* $C_2H_4^+$, and $C_4H_6^+$) was chosen. The species and their respective masses include Li_2^+ (14.03 Da), $C_2H_3^+$ (27.02 Da), CH_3O^+ (31.03 Da), and $C_2H_2Li^+$ (33.03 Da) while the transition metals were also selected Ni^+ (57.93 Da), Mn^+ (54.94 Da), and Co^+ (58.93 Da). **Figure 5-12 (a)** shows the growth of an SEI-like surface layer on the cathode as seen from the increasing FWHM of the $C_2H_2Li^+$ species from 0.5 to 5.2 nm FWHM after 3200 h. This cathode surface layer has been observed in different electrode materials in the literature and is known as the solid permeable interface [6]. The thickness of the solid permeable interface on cathodes can increase significantly with increasing temperatures [6]. The high temperature and state of charge in this study likely contributed significantly to the growth of this layer as the total amount of electrochemical
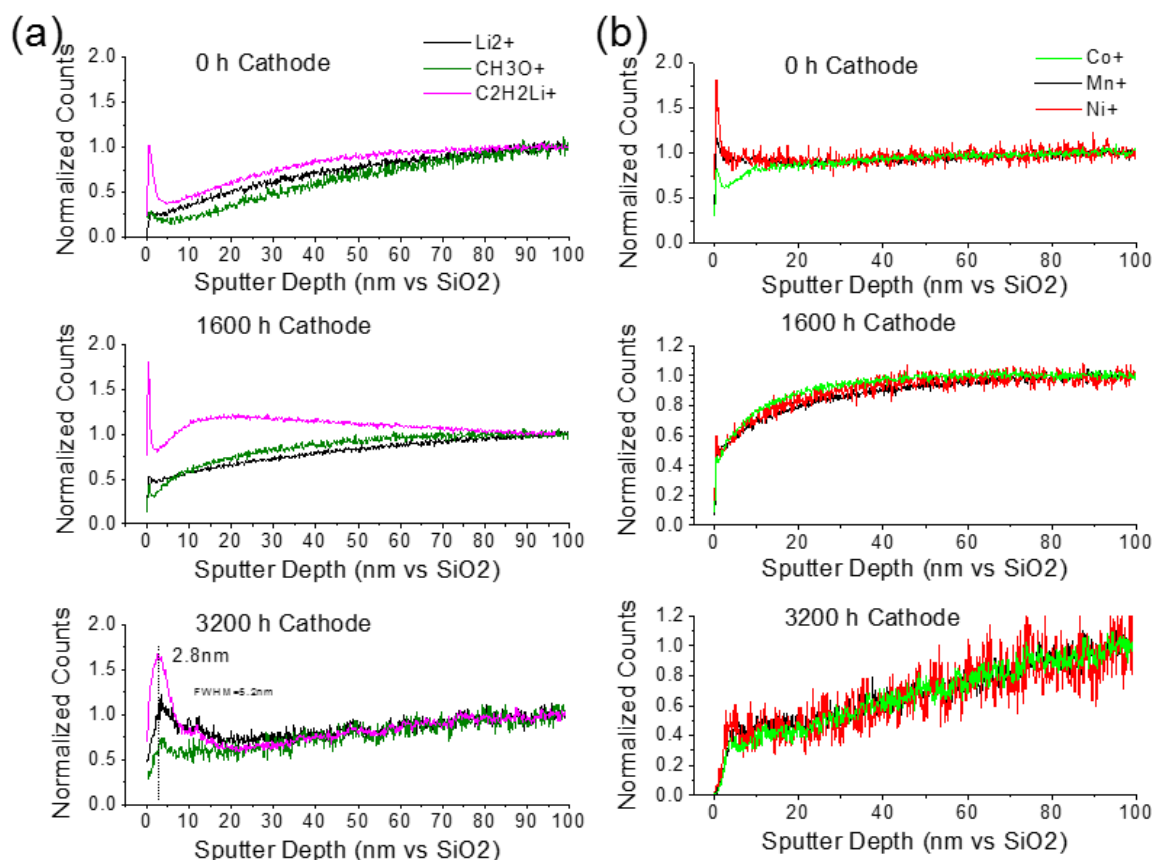
Figure 5-12. SIMS depth profile showing **(a)** left three figures surface layer formation on the positive electrode and **(b)** right three figures rate of active material dissolution increases in aged positive electrode. The counts were normalized so that the count at the bulk of the electrode is one. The sputter rate was measured with respect to a SiO_2/Si standard.

cycling was very low. In **Figure 5-12** (**b**), the surface composition of transition metal species constituting the positive electrode is shown. As aging proceeds, these species appear to be further removed from the surface as shown by a gradually increasing depletion layer which eventually flattens into a linear depletion layer for the electrode from the cell aged for 3200h. This process is more substantial than the film formation as evident by the depth/thickness observed (100 nm *vs.* 5 nm for the cathode surface layers) and is likely due to the increased dissolution and loss of the materials from the cathode. Transition metal dissolution is known to occur in NCM electrodes, and dissolution is exacerbated at high

temperatures and high potentials [20, 21]. Aging the cell for an extended duration at a potential above 4 V (at 90 % SOC) at 75 °C likely led to the removal of transition metal species from the positive electrode surface and increased dissolution with aging time.

TEM was used to analyze the cathode surfaces and directly observe the surface layer, as differences were not identifiable by FIB/SEM. The cathodes were immersed in DMC and sonicated to disperse the powders and drop casted onto a grid. For all samples, multiple particles were investigated to ensure reproducibility. **Figure 5-13** shows high resolution TEM images of fresh, 1600 hours and 3200 hours cathode samples. The surface of fresh and 1600 hours cathode samples (**Figure 5-13** (**a**), (**b**),(**d**), and (**e**) were very clean and the same crystalline structure is discernible up to the edge of the particle. Additionally, XPS and SIMS show surface layers for both 1600 and 3200 h samples so it is likely that some of the surface layer observed in XPS and SIMS was removed during sonication/sample preparation. However, a lighter shaded amorphous layer is clearly visible on the surface of the 3200 hour aged cathode in **Figure 5-13** (**c**) and (**f**). Since the surface layer coatings of fresh and 1600 hours aged cathode samples were negligible, this amorphous layer is not PVDF binder. A more plausible explanation is that this layer observed in TEM is an inorganic amorphous surface layer formed by the degradation of active material. Changes on the positive electrode caused by the surface layer formation and dissolution likely led to increased mass transport losses in the cell as the aging time increased [22].
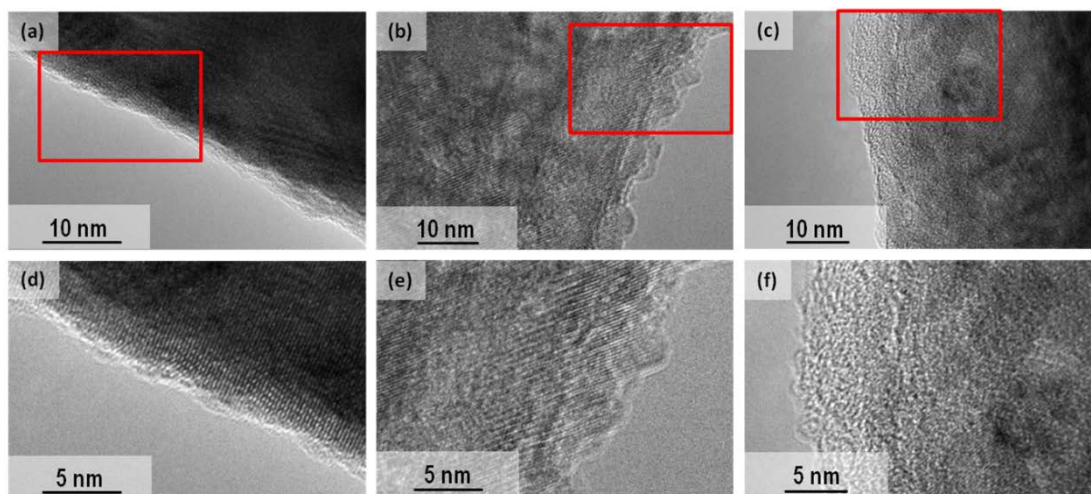
Figure 5-13. High resolution TEM images of positive electrodes samples recovered from cells after aging **(a)** 0 Hours, **(b)** 1600 Hours, and **(c)** 3200 Hours and their magnified images **(d, e, f)**.

In order to understand the capacity fade mechanism, cell charge resistance and capacities with aging are re-plotted in **Figure 5-14**. In previous reports on capacity fade, mainly SEI growth and the corresponding loss of cyclable lithium are implicated for cell degradation with aging and cycling [3, 7, 26]. This degradation mode is often described by a parabolic growth of the SEI and follows a linear decrease of capacity with the square root of time [10]. In **Figure 5-14** (**a**), capacity and resistance are plotted against the
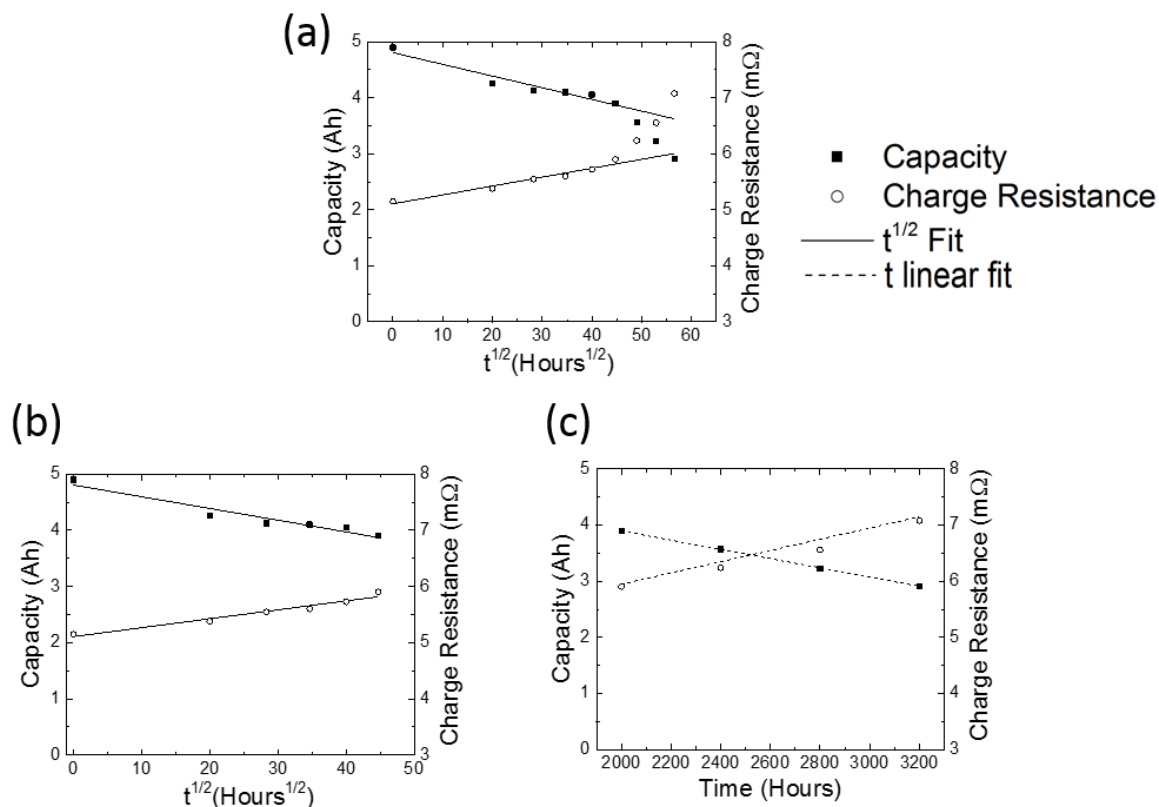
Figure 5-14. Capacity fade over time can be divided into two regimes: first the capacity fade is dominated by loss of lithium inventory in the SEI in anode; later the capacity fade is dominated by the material loss from cathode. The difference in mechanism is represented by plotting losses as a function of $t^{1/2}$ in the beginning of aging **(a)** and as a function of t in the latter stages of aging **(b)**.

square root of aging time. Both capacity and resistance display parabolic decay/growth in the beginning, and is consistent with previous degradation studies [7, 9, 10]. However, after 2000 hours, both capacity and resistance deviate from the trend, suggesting a different degradation mechanism. Imaging of the anode cross-section via FIB/SEM highlighted an increased SEI, and XPS results showed surface layer growth on both the anode and cathode. As SEI growth continued in the beginning of aging, more lithium was lost irreversibly in the anode and contributed to capacity loss. The storage conditions used in

this study (75 °C and 90% SOC) are extremely conducive to solvent reduction/SEI growth on anode. Hence, the degradation through this mechanism is accelerated.

The resistance increase and capacity fade in the later stages of aging follows a linear trend with time. This change in behavior indicates a difference in degradation mechanism compared to the earlier stage where lithium loss in the SEI dominated degradation behavior. This varied mechanism may be explained by the material loss from the positive electrode as evidenced by the transition metal depletion shown in the SIMS results. The rate of material loss seems to have been expedited after 1600 hours. Furthermore, TEM results show that the positive electrode surface loses its crystallinity. This may be explained by the active material loss and formation of a surface layer on the cathode. Active material loss from the positive electrode may also explain the increased internal resistance and diffusional resistance as seen in EIS.

5.4 Conclusions

In this study, cell resistance increase and capacity fade occurring in commercial prismatic cells were studied using electrochemical and post-mortem analyses. Accelerated calendar aging was achieved by storing cells at a high temperature of 75 °C. Cell resistance and capacity were mainly influenced by the degradation occurring in the negative electrode due to SEI growth in the beginning stages of aging. Loss of cyclable lithium in the SEI contributed to increased cell resistance and capacity fade. In later stages of aging, changes occurring in the positive electrode became the dominant mode of degradation. Active material dissolution and surface layer formation of cathode contributed to an increased rate of cell performance degradation with aging. It may be possible to limit capacity and power

fade in these types of cells by addressing the mode by which degradation proceeds: namely SEI growth and cathode active material degradation. It may be possible to limit the solvent reduction and SEI growth on the negative electrode by adding some SEI-forming additives in the electrolyte solution [11]. Furthermore, mechanisms of performance degradation due to active material dissolution and surface layer formation on NCM positive electrodes need further investigation to understand how this occurs and delay the accelerated decline in power and capacity.

5.5 References

1.   Arora, P., R.E. White, and M. Doyle, *Capacity fade mechanisms and side reactions in lithium-ion batteries.* Journal of the Electrochemical Society, 1998. **145**(10): p. 3647-3667.

2.   Dubarry, M., et al., *Capacity and power fading mechanism identification from a commercial cell evaluation.* Journal of Power Sources, 2007. **165**(2): p. 566-572.

3.   Zhang, Q. and R.E. White, *Calendar life study of Li-ion pouch cells.* Journal of Power Sources, 2007. **173**(2): p. 990-997.

4.   Ecker, M., et al., *Calendar and cycle life study of Li(NiMnCo)O2-based 18650 lithium-ion batteries.* Journal of Power Sources, 2014. **248**(0): p. 839-851.

5.   Bloom, I., et al., *Effect of cathode composition on impedance rise in high-power lithium-ion cells: Long-term aging results.* Journal of Power Sources, 2006. **155**(2): p. 415-419.

6.   Edström, K., T. Gustafsson, and J.O. Thomas, *The cathode–electrolyte interface in the Li-ion battery.* Electrochimica Acta, 2004. **50**(2–3): p. 397-403.

7.   Broussely, M., et al., *Aging mechanism in Li ion cells and calendar life predictions.* Journal of Power Sources, 2001. **97–98**(0): p. 13-21.

8.   Zheng, H.H., et al., *Correlation between dissolution behavior and electrochemical cycling performance for LiNi1/3Co1/3Mn1/3O2-based cells.* Journal of Power Sources, 2012. **207**: p. 134-140.

9.   Wright, R.B., et al., *Calendar- and cycle-life studies of advanced technology development program generation 1 lithium-ion batteries.* Journal of Power Sources, 2002. **110**(2): p. 445-470.

10.   Ploehn, H.J., P. Ramadass, and R.E. White, *Solvent diffusion model for aging of lithium-ion battery cells.* Journal of the Electrochemical Society, 2004. **151**(3): p. A456-A462.

11.   Eom, K., et al., *The design of a Li-ion full cell battery using a nano silicon and nano multi-layer graphene composite anode.* Journal of Power Sources, 2014. **249**(0): p. 118-124.

12.   Dubarry, M., et al., *Evaluation of commercial lithium-ion cells based on composite positive electrode for plug-in hybrid electric vehicle applications. Part I: Initial characterizations.* Journal of Power Sources, 2011. **196**(23): p. 10328-10335.

13.   Jung, S.K., et al., *Understanding the Degradation Mechanisms of LiNi0.5Co0.2Mn0.3O2 Cathode Material in Lithium Ion Batteries.* Advanced Energy Materials, 2014. **4**(1).

14.   Stiaszny, B., et al., *Electrochemical characterization and post-mortem analysis of aged LiMn2O4–NMC/graphite lithium ion batteries part II: Calendar aging.* Journal of Power Sources, 2014. **258**(0): p. 61-75.

15.   Wang, J., et al., *Degradation of lithium ion batteries employing graphite negatives and nickel–cobalt–manganese oxide + spinel manganese oxide positives: Part 1, aging mechanisms and life estimation.* Journal of Power Sources, 2014. **269**(0): p. 937-948.

16.   Joshi, T., et al., *Effects of Dissolved Transition Metals on the Electrochemical Performance and SEI Growth in Lithium-Ion Batteries.* Journal of the Electrochemical Society, 2014. **161**(12): p. A1915-A1921.

17.   Bandhauer, T.M., S. Garimella, and T.F. Fuller, *A Critical Review of Thermal Issues in Lithium-Ion Batteries.* Journal of The Electrochemical Society, 2011. **158**(3): p. R1-R25.

18.   Zhang, X., A.M. Sastry, and W. Shyy, *Intercalation-Induced Stress and Heat Generation within Single Lithium-Ion Battery Cathode Particles.* Journal of The Electrochemical Society, 2008. **155**(7): p. A542-A552.

19.   Bard, A.J. and L.R. Faulkner, *Electrochemical Methods: Fundamentals and Applications*. 2000: Wiley.

20.   Jang, D.H., Y.J. Shin, and S.M. Oh, *Dissolution of spinel oxides and capacity losses in 4V Li/LixMn2O4 coils.* Journal of the Electrochemical Society, 1996. **143**(7): p. 2204-2211.

21.   Abraham, D.P., et al., *Evidence of Transition-Metal Accumulation on Aged Graphite Anodes by SIMS.* Electrochemical and Solid State Letters, 2008. **11**(12): p. A226-A228.

22.   Julien, C., et al., *Comparative Issues of Cathode Materials for Li-Ion Batteries.* Inorganics, 2014. **2**(1): p. 132.

23.   Mellgren, N., et al., *Impedance as a tool for investigating aging in lithium-ion porous electrodes.* Journal of the Electrochemical Society, 2008. **155**(4): p. A304-A319.

24.   Zhang, S.S., K. Xu, and T.R. Jow, *Electrochemical impedance study on the low temperature of Li-ion batteries.* Electrochimica Acta, 2004. **49**(7): p. 1057-1061.

25.   Herstedt, M., et al., *X-ray photoelectron spectroscopy of negative electrodes from high-power lithium-ion cells showing various levels of power fade.* Electrochimica Acta, 2004. **49**(28): p. 5097-5110.

26.   Lee, J.T., et al., *Comparative study of the solid electrolyte interphase on graphite in full Li-ion battery cells using X-ray photoelectron spectroscopy, secondary ion mass spectrometry, and electron microscopy.* Carbon, 2013. **52**: p. 388-397.

CHAPTER 6

ON CAPACITY AND POWER FADE RESULTING FROM LITHIUM LOSS IN THE SEI

6.1 Introduction

Lithium-ion batteries are excellent candidates for hybrid electric vehicles (HEV). Lithium-ion batteries used in HEVs can provide power to the vehicle and replenish the charge during regenerative braking. HEVs employ two power sources: (i) a primary power source such as an internal combustion engine (ICE) which supplies steady power to the vehicle most of the time at maximum efficiency and (ii) an auxiliary source such as batteries that can supply and absorb short-busts of high power. In power-assist hybrids, the batteries are relatively small and are only used on a demand basis for dynamic power during events like acceleration, deceleration, and climbing up and down grades. To accomplish large power requirements, these batteries must be capable of providing and absorbing large currents while operating in a narrow state of charge (SOC) window. Batteries normally operate near 50 % SOC in HEVs, and the change in SOC is minimal during operation. Since these types of applications don't use the batteries for electric-only propulsion, the energy (capacity) requirements are low for the batteries. However, the batteries help propel the vehicles when high power is needed during acceleration and hill-climbing. They need to provide instantaneous power as required and thus, power capability is more important than capacity.

Power capability in lithium-ion batteries can be evaluated by applying a pulse current to a cell at equilibrium. There are many variations in techniques that are used to measure power capability and cell resistance. One variation of such technique is the approach that was used in **Chapter 5**. A more commonly used technique is the hybrid pulse power characterization (HPPC) test developed by the US Department of Energy (USDOE) Advanced Technology Development (ATD) Program [1]. Despite slight variations, all techniques are similar in that a current pulse is applied to a cell at equilibrium, and power capability and cell resistance are measured from the potential drop caused by the pulse current.

A significant impediment to batteries used in power-assist hybrids is that the batteries lose their power capability after repeated use or prolonged storage. The power capability loss is higher at elevated temperatures [2]. This loss of power capability of batteries is commonly referred to as power fade. Lithium-ion batteries are prone to degradation that results in the loss of capacity and power. Losses occurring through undesirable side reactions, such as electrolyte reduction to form the solid electrolyte interphase (SEI), are major contributing factors to the performance decay in batteries [3].

SEI growth has been implicated in the reduction of cell capacity. With the formation of the SEI, lithium that is normally cycled between electrodes is consumed forming the SEI. Lower cell capacities in aged cells, commonly called capacity fade, is attributed to the loss of cyclable lithium in the SEI. For a cell operating within fixed charge and discharge voltage limits, cell capacity is largely determined by how much cyclable lithium is shuttled back and forth between the positive and negative electrodes during

charge and discharge. Thus, any loss in total cyclable lithium leads to decreased cell capacity.

Additionally, SEI growth has been implicated in cell power fade—which is the reduction in cell power in aged or cycled cells. Though highly simplified, we can think of the SEI as an additional resistance in series with the lithium insertion/deinsertion reactions. The additional iR associated with SEI growth causes the cell resistance to increase, which results in lower power capability. The cell potential and peak power for an ohmically limited cell during a constant current discharge are given by

$$V_{\text{cell}} = V_{\text{ocv}}^{d} - IR_{\text{cell}}^{d} \qquad [6\text{-}1]$$

and

$$P_{max} = \frac{\left(V_{\text{ocv}}^{d}\right)^{2}}{4R_{cell}^{d}} \qquad [6\text{-}2]$$

where V_{ocv}^{d} is the open-circuit potential and R_{cell}^{d} is the cell resistance during discharge. The importance of resistance of the cell and power capability is obvious. It is likely that that the voltage limits on charge and discharge are met before the maximum power given by **Equation [6-2]** is reached. For an ohmically limited cell, the maximum power is $I_{\text{cell}}[V_{\text{ocv}} - I_{\text{cell}}R_{\text{cell}}]$. Regardless, the formation and growth of the SEI leads to an increase in ohmic resistance and a decrease in power capabilities in lithium-ion batteries.

The results for the commercial cell studied in **Chapter 5** do not support this simplistic view, and the increased cell resistance cannot solely be attributed to increased ohmic resistance. First, even with a fresh cell with no degradation due to high temperature aging, the ohmic resistance is relatively small compared to concentration polarizations. Second, the increase in ohmic resistance with aging is not significant. On the other hand,

the increase in concentration polarization with aging is important. While power fade due to ohmic resistance increase for the cell is ruled out, the root cause for power fade is not clear. We have previously discussed how the loss of cyclable lithium in the cell results in capacity fade. Here, we want to consider how the loss of cyclable lithium affects power fade. The starting point of the power capability test is a fixed cell potential. At a fixed potential, the amount of lithium in each electrode changes as cyclable lithium is lost. The hypothesis is that this change in the lithium content can in part explain the power fade data.

Although some previous studies have looked at capacity fade and lithium loss in the SEI, the relationship between lithium loss in the SEI and power fade occurring in cells is less clear. Zhang *et al*. studied degradation in LiFePO4/graphite cells subject to cycling. They attributed capacity fade to the loss of cyclable lithium in the SEI and power fade to the increased surface resistance related to the SEI [4]. Although their results show an increase in diffusional impedance with cycling, they do not explain the contributions of increased diffusional impedance on power fade. Furthermore, they failed to look at the contributions of lithium loss on power fade. Capacity and power fade in lithium-ion cells are related, and they are primarily caused due to the loss of cyclable lithium in the SEI. There is a lack of studies done to understand the effect of lithium loss in the SEI on power capability of cell. Understanding the role of lithium loss in the SEI is important to address the losses in performance related to capacity and power. A better understanding of the role of the SEI and lithium loss on capacity and power capability of cell enables better cell design to abate cell performance degradation.

Performance degradation in lithium-ion cells can occur from many different mechanisms as was described in **Chapter 2**. Multiple degradation mechanisms may occur

simultaneously in cells. As a result, it is difficult to isolate a single degradation mechanism and analyze the contributions of that degradation mechanism on overall cell capacity and power. A physics-based model helps to solve this problem. By using a physics-based model that describes cell performance accurately, it is possible to investigate the effects of any degradation mechanism on cell performance. Specific degradation modes such as SEI growth can be added to the model and comparisons can be made to understand the limitations on performance due to such mechanisms.

In this chapter, the effects of cyclable lithium loss in the SEI on the capacity and power fade of lithium-ion batteries is studied. Lithium loss from the formation of the SEI in most commonly used lithium-ion cells today is inevitable. We intend to illustrate and quantify the losses including capacity and power fade occurring in lithium-ion cells due to lithium loss in the SEI. In this study, we focus on these losses occurring in full cells containing commonly used electrode materials. Simulations are based on graphite negative electrodes and $LiNi_{1/3}Co_{1/3}Mn_{1/3}O_2$ (NCM) positive electrodes.

6.2 Model Development

A schematic of a cell with graphite composite electrode/separator/NCM composite electrode is shown in **Figure 6-1**. A macro-homogeneous approach is used with concentrated solution theory to model the dual lithium-ion cell sandwich. The model used in this work is based on the model developed by Fuller *et al.* [5-7]. Open-circuit potential functions of the electrodes and review of this model are presented in **Appendix A** and **B** respectively.
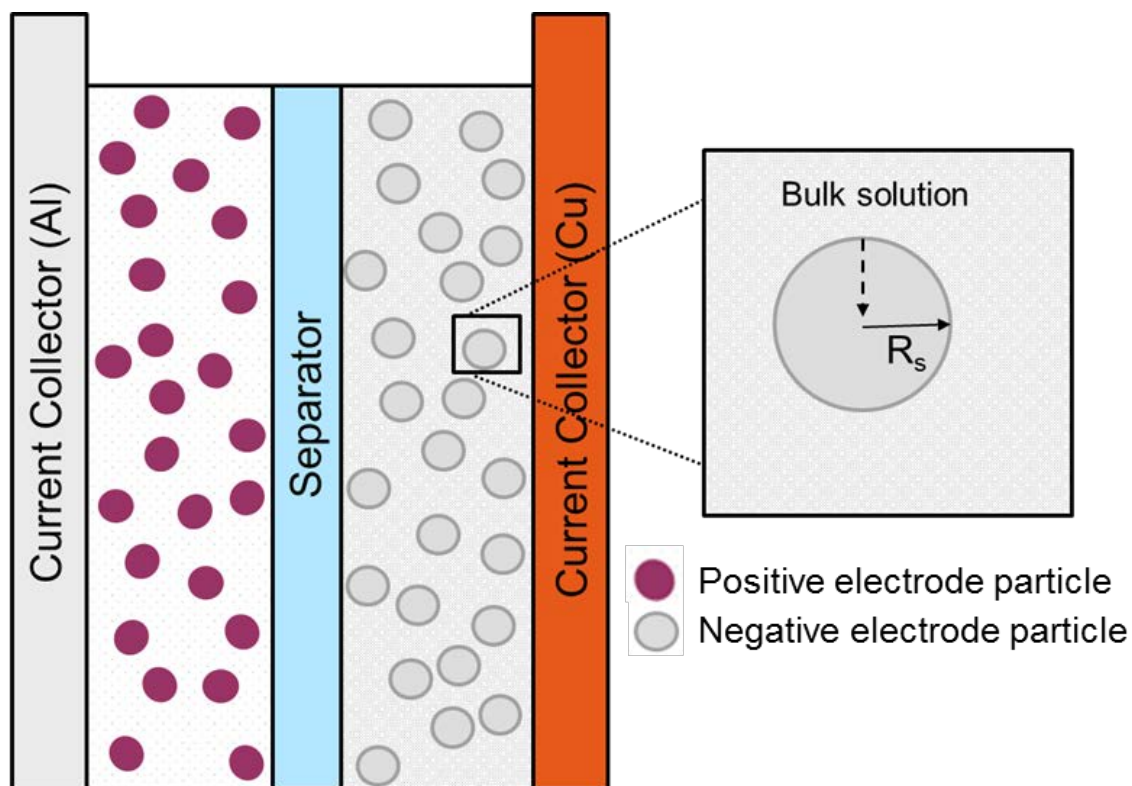
Figure 6-1. Schematic of a full cell with composite graphite/separator/composite NCM electrode.

     Figure 6-2 illustrates the approach used to solve the model. In this model, transport of lithium ions in the solution phase between the electrodes through the separator is treated as one-dimensional in the axial direction. The transport within the electrodes is treated as two-dimensional in both the axial and radial directions.
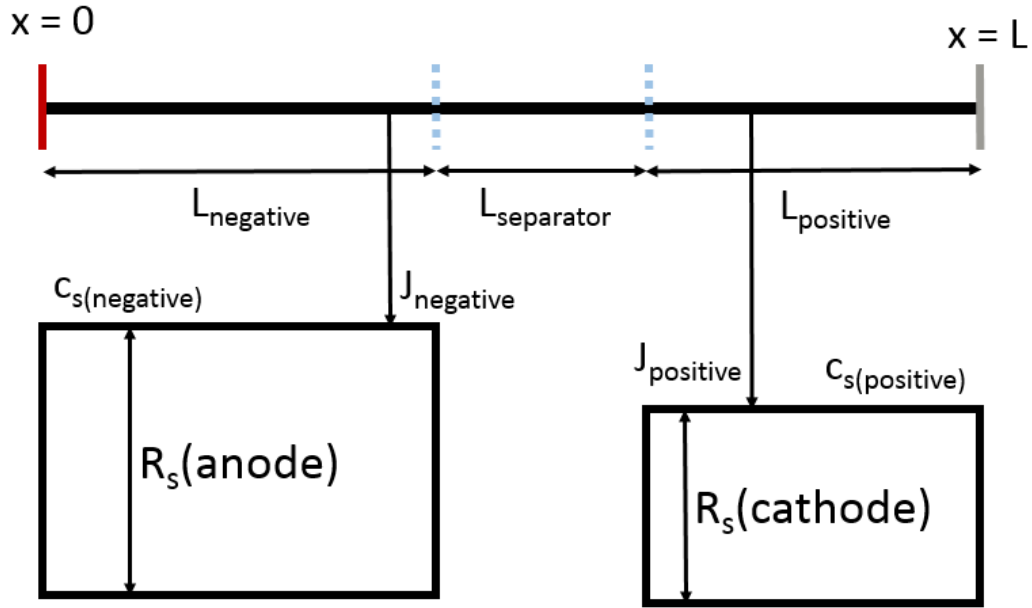
Figure 6-2. Model dimensional topology. Lithium transport in the solid phase within the electrodes is considered 2D and the transport in the solution phase between electrodes through the separator is considered 1D.

The governing equations and boundary conditions used are summarized in **Table 1**. The open-circuit potential functions for the two composite electrodes were obtained by fitting the discharge curves from half cells constructed from electrodes harvested from the battery. Parameters used in the model are listed in **Table 2**. Parameters were measured experimentally for the cell, whenever possible. After that, estimations were made based on known values for the cell. In order to fit the simulated results with the experimental data, some parameters were manually adjusted within the acceptable range of values available in the literature to make the simulation results match the experimental data. The set of equations in **Table 1** was solved as 1D-2D coupled model for the three domains (negative electrode/separator/positive electrode) using COMSOL multiphysics finite element

software (version 4.4). The mesh sizes and tolerances were adjusted to enable model convergence.

Table 6-1. List of equations and boundary conditions used in the model.

Equations	Boundary Conditions
Li transport in active material: $$\frac{\partial c_s}{\partial t} = \frac{1}{r^2}\frac{\partial}{\partial r}\left(r^2\left(D_s\frac{\partial c_s}{\partial r}\right)\right)$$	$\frac{\partial c_s}{\partial r} = 0$; at r = 0 (center of the particle) $j_n = -D_s\frac{\partial c_s}{\partial r}$; at r = R_s (particle surface)
Li transport in solution phase: $$\varepsilon\frac{\partial c}{\partial t} = \nabla\cdot(D_{eff}\nabla c) - \frac{i_2\cdot\nabla t_+^0}{F} + aj_n(1-t_+^0)$$	$\nabla c = 0$; at x = 0 and x = L (current collector/electrode interface)
Solid phase potential: $$i_1 = -\sigma_{eff}\nabla\phi_1$$	$\phi_1 = 0$; at x = 0 $\nabla\phi_1 = -I/\sigma_{eff}$; at x = L
Solution phase potential: $$i_2 = -\kappa_{eff}\nabla\phi_2 + \frac{2\kappa_{eff}RT}{F}\left(1+\frac{\partial\ln f_A}{\partial\ln c}\right)(1-t_+^0)\nabla\ln c$$	$\nabla\phi_2 = 0$; at x = 0 and x = L
Li intercalation: $$i_{int} = kFc^{\alpha_a}(c_{max}-c_s)^{\alpha_a}c_s^{\alpha_c}\left\{\exp\left(\frac{\alpha_a F\eta}{RT}\right) - \exp\left(\frac{\alpha_c F\eta}{RT}\right)\right\}$$ $$\eta = \phi_1 - \phi_2 - U$$	

The SEI formation on graphite electrodes has been studied by Aurbach *et al.* for common solvents used in Li-ion system such as ethylene carbonate (EC) and diethylene carbonate (DEC) [8]. Based on these common solvents and the reduction products formed, the irreversible SEI forming reaction can be represented by

$$S + 2Li^+ + 2e^- \rightarrow P \qquad\qquad [6\text{-}1]$$

where S is the species being reduced. The reduced species combines with lithium to form salt products P and precipitates to form the SEI. The SEI is believed to consist of two layers: an inner dense layer and an outer porous layer [9, 10]. The inner dense layer is mainly composed of inorganic lithium salts like lithium carbonate, lithium fluoride, and lithium oxides whereas the outer porous layer is mainly composed of organic lithium salts such as alkyl carbonates and other polymeric species. The dense layer is thin and its thickness is determined by the maximum length required for electron-tunneling [11]. Regardless of the mechanism, the growth rate of the SEI is dependent on the side-reaction current density (i_s) through

$$\frac{d\delta}{dt} = -\frac{i_s}{2F}\left(\frac{M_{out}(1-\varepsilon_{out})}{\rho_{out}} + \frac{M_{in}(1-\varepsilon_{in})}{\rho_{in}}\right) \qquad\qquad [6\text{-}2]$$

where M, ρ, and ε are respectively the molecular weight, density, and porosity. In the equation above, subscripts *out* and *in* refer to the outer porous and inner dense layers of the SEI. After the formation period, the thickness of the compact layer is assumed to be constant and SEI growth is believed to be limited by the solvent transport through the porous layer [12, 13]. We assumed the initial thickness of the SEI after formation period to be 5 nm. Ploehn *et al*. solved the case where solvent diffusion through the porous layer limited the SEI growth [12]. The porous layer was assumed to have a constant porosity and the concentration of solvent in the SEI was assumed to be negligible compared to the concentration of reduction products forming the SEI. The thickness of the porous layer is given by

$$\delta_{out} = 2\lambda\sqrt{D_{sol}t} \qquad\qquad [6\text{-}3]$$

where D_{sol} is the effective diffusivity of the solvent in the SEI and λ is given by the solution to

$$\lambda = \frac{c_{eq}}{\sqrt{\pi} c_p} \frac{\exp\left(-\lambda^2\right)}{\operatorname{erf}\left(\lambda\right)} \qquad [6\text{-}4]$$

where c_{eq} is the equilibrium concentration of the solvent in the SEI and c_p is the concentration of the reduction products forming the SEI. Ploehn *et al.* used λ values of 0.21 and 0.27 to fit experimental capacity fade results for different cell types.

The total lithium in the cell is fixed and is limited by the amount of lithium in the positive electrode during cell assembly. For this section, we assume SEI formation on the negative electrode as the only degradation mechanism occurring in the cell. As the cell goes through charge/discharge cycles, lithium is shuttled between the positive electrode and the negative electrode. When the SEI forms, a small fraction of the lithium that is being shuttled between electrodes reacts irreversibly to form a solid product. The lithium that goes to form the SEI is no longer available for further charge/discharge and is said to be "lost". This situation is represented by a simple lithium balance

$$n_{Li,total} = n_{Li,p} + n_{Li,n} + n_{Li,SEI} \qquad [6\text{-}5]$$

$$n_{Li,tot} = \left(\frac{C_s L \varepsilon_1 \rho}{F}\right)_p \qquad [6\text{-}6]$$

$$n_{Li,p} = y \left(\frac{C_s L \varepsilon_1 \rho}{F}\right)_p \qquad [6\text{-}7]$$

$$n_{Li,n} = x \left(\frac{C_s L \varepsilon_1 \rho}{F}\right)_n \qquad [6\text{-}8]$$

$$n_{Li,SEI} = \left(\frac{\delta a L \rho}{M}\right)_n \qquad [6\text{-}9]$$

where C_s is the specific capacity of the electrode; L is the length of electrode; $n_{Li,tot}$ is the total lithium in the cell, which is dictated by the lithium available in the positive electrode during cell assembly; $n_{Li,p}$ is the lithium in the positive electrode during cell operation; $n_{Li,n}$ is the lithium in the negative electrode, excluding the lithium in the SEI; and $n_{Li,SEI}$ is the lithium lost in the SEI. Subscript p and n refer to positive and negative electrodes; x and y refer to the dimensionless lithium concentration in the negative and positive electrodes (x in Li_xC_6 for the negative electrode and y in $Li_yNi_aCo_bMn_cO_2$ for the positive electrode); ε denoted the volume fraction and subscripts 1 and 2 refer to solid and solution phase, respectively.

The conservation equation for lithium in the cell in **Equation [6-5]** can also be written as

$$\left[c_{max}L(1-\varepsilon_1-\varepsilon_2)\right]_p = x\left[c_{max}L(1-\varepsilon_1-\varepsilon_2)\right]_n + y\left[c_{max}L(1-\varepsilon_1-\varepsilon_2)\right]_p + \left(\frac{\delta aL\rho}{M}\right)_n \qquad [6\text{-}10]$$

where c_{max} is the maximum lithium concentration inside the active material.

Table 6-2. List of parameters used in the model.

Symbol	Units	Negative Electrode (Graphite)	Separator/ Electrolyte	Positive Electrode (NCM)
R_s	m	10 x 10^{-6} m		1 x 10^{-6} m
c_{max}	mol/m^3	28442 [e]		28356 [e]
L	m	35 x 10^{-6} m	25 x 10^{-6} m	30 x 10^{-6} m
k	mol/(m^{2}s(mol/m^3)$^{1.5}$)	1 x 10^{-8} [ad]		1.2 x 10^{-9} [ad]
α_a		0.5 [a]		0.5 [a]
α_c		0.5 [a]		0.5 [a]
D	m^2/s		7 x 10^{-11} [a]	
	mol/m^3		1200 [m]	

D_s	m^2/s	1.7×10^{-14} [ad]		1.1×10^{-15} [ad]
ε_1		0.39 [e]		0.47 [e]
ε_2		0.59 [e]	0.5 [a]	0.50 [e]
T	K		298	
κ	S/m		0.89 [m]	
σ	S/m	100 [ad]		100 [ad]

SEI Parameters:	
D_{sol} (m^2/s)	3.7×10^{-19}
λ	(Ref.[14])
M (kg/mol)	0.27 (Ref.[12])
ρ (kg/m^3)	0.162 (Ref.[14])
	1710[a]

a = assumed; ad = adjusted; e = estimated; m = measured experimentally

In our discussion earlier, we noted that power capability is of utmost importance in batteries designed for power assist HEVs, where the battery is operated in charge sustaining mode. High power capability is achieved in these cells by making the electrodes very thin. Slower kinetics at the electrode-electrolyte interface can lead to higher interfacial overpotentials. Decrease in electronic conductivity of the electrode due to loss of particle contact with the current collector can lead to higher kinetic resistance. Similarly, mass-transfer of electrolyte species can cause concentration overpotentials, mainly through diffusion processes. These higher overpotentials contribute directly to cell resistance. In turn, resistance increases due to degradation mechanisms lead to decreased power capabilities in cells. Cell resistance and power capability can be determined by employing different types of pulse profiles and testing procedures. In this work, cell resistance and power capability were evaluated by following the HPPC test as described in the FreedomCAR battery test manual [1]. HPPC test profiles prescribed by the DOE provides

a common benchmark to determine dynamic power capability using a test profile that incorporates both discharge and charge current pulses.

HPPC test protocol uses constant current pulses for discharge and charge with a rest period in between. Here, charging is meant to simulate energy recovery during braking. The characterization profile is shown in **Figure 6-3**. First, a 10-s discharge pulse is applied. Then, a 40-s rest period follows to allow the system to relax at open circuit. Finally, a 10-s charge pulse is used at 75 % of the current used for discharge pulse. The FreedomCAR test manual provides guidelines for these tests and the 10 s pulse current to be used in these tests is determined experimentally based on the maximum pulse current rated by the battery manufacturer. The pulse current used in this work was determined by simulating discharges at 50 % SOC and increasing the discharge current until the voltage limit for discharge for the cell (2.4 V) was met. The pulse current for charge was set at 75 % of the discharge current according to the HPPC protocol. Pulse characterization simulations were performed at a voltage of 3.7 V (corresponding to 50 % SOC) to calculate resistance and power. Based on this profile, the pulse resistance is calculated for discharge and charge

$$\text{Discharge Resistance } (R_{cell}^d) = \frac{\Delta V_{\text{discharge}}}{\Delta I_{\text{discharge}}} = \frac{V_{t1} - V_{t0}}{I_{t0} - I_{t1}} \qquad [6\text{-}11]$$

$$\text{Charge Resistance } (R_{cell}^c) = \frac{\Delta V_{\text{charge}}}{\Delta I_{\text{charge}}} = \frac{V_{t3} - V_{t2}}{I_{t2} - I_{t3}} \qquad [6\text{-}12]$$

From the resistance, we can calculate pulse power capability for discharge and charge by using the equations provided in the FreedomCAR manual [1]

$$\text{Discharge Pulse Power Capability } \left(P_{\max}^d \right) = \frac{V_{\min}(V_{\text{ocv}}^d - V_{\min})}{R_{cell}^d} \qquad [6\text{-}13]$$

133

$$\text{Charge Pulse Power Capability} \left(P_{max}^c \right) = \frac{V_{max} \left(V_{max} - V_{ocv}^c \right)}{R_{cell}^c} \qquad [6\text{-}14]$$

where V_{min} and V_{max} are cutoff potentials for discharge and charge as recommended by the manufacturer, and V_{ocv} is the open-circuit voltage before the application of discharge or charge pulse.
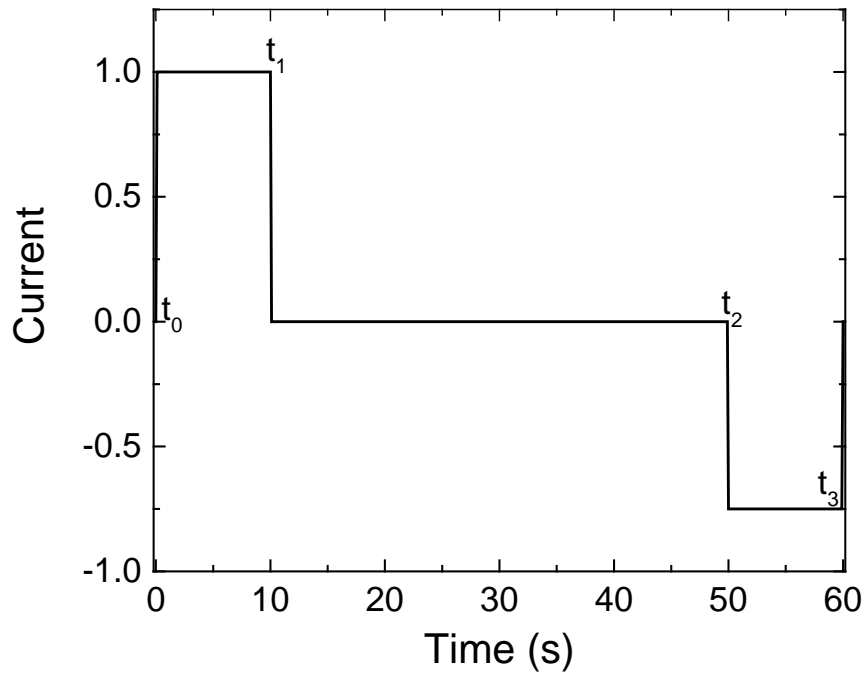

Figure 6-3. Hybrid pulse power characterization test profile.

6.3 Results and Discussion

Model simulations were run and comparisons were made to the experimental results to check the accuracy of the model. The objective was to get general behavior from the simulation to match the experimental data and use the model for exploring the hypothesis.

134

The goal of these comparisons was not model validation—this validation of cell parameters is an on-going investigation and it will be continued by other group members. In **Figure 6-4**, simulated results at different rates are compared to experimental results. Experimental results are for a fresh cell as received from the manufacturer with no further cycling degradation. We define a fresh cell as a cell that not undergone any aging or cycling degradation besides the formation cycles. This cell has gone through formation cycles completed by the battery manufacturer, and the initial SEI is already formed. The thickness of the SEI was assumed to be 5 nm for fresh cell. The cell was discharged from 4.2 V to 2.4 V at 1C based on manufacturer's rated capacity for the cell. The experimental cell was kept in an environmental chamber at 25 °C. Simulated results are represented by lines and experimental results are represented by solid markers. This convention is used in all subsequent plots. The simulation shows a good fit with experimental results, with the exception towards the end of the discharge, where a slight variation between simulation results and experimental data is seen. This deviation is likely caused due to the inaccuracy of the assumed transport properties in the model. In order to simplify the model, we used constant values of parameters including diffusivities and electrolyte conductivity in the model. Using a constant diffusion coefficient and changing the values has a minor effect at low rates. We fail to accurately account for the diffusional limitations occurring in the solid and solution phase at higher rates by using constant diffusivity values for the solid phase diffusion in the electrode and solution phase diffusion in the electrolyte at all discharge rates. As a result, a constant diffusion coefficient value providing a good fit at one rate may over-predict or under-predict the cell performance at other rates. Similarly, electrolyte transport properties are concentration dependent. Data for the composition

dependence of diffusivity and ionic conductivity are needed to better match the experimental data. Furthermore, OCV functions were derived from half-cells made from electrodes that were recovered from full cell due to lack of availability of fresh electrodes. Slight deviation of simulation results from experimental data may be improved by addressing these factors.
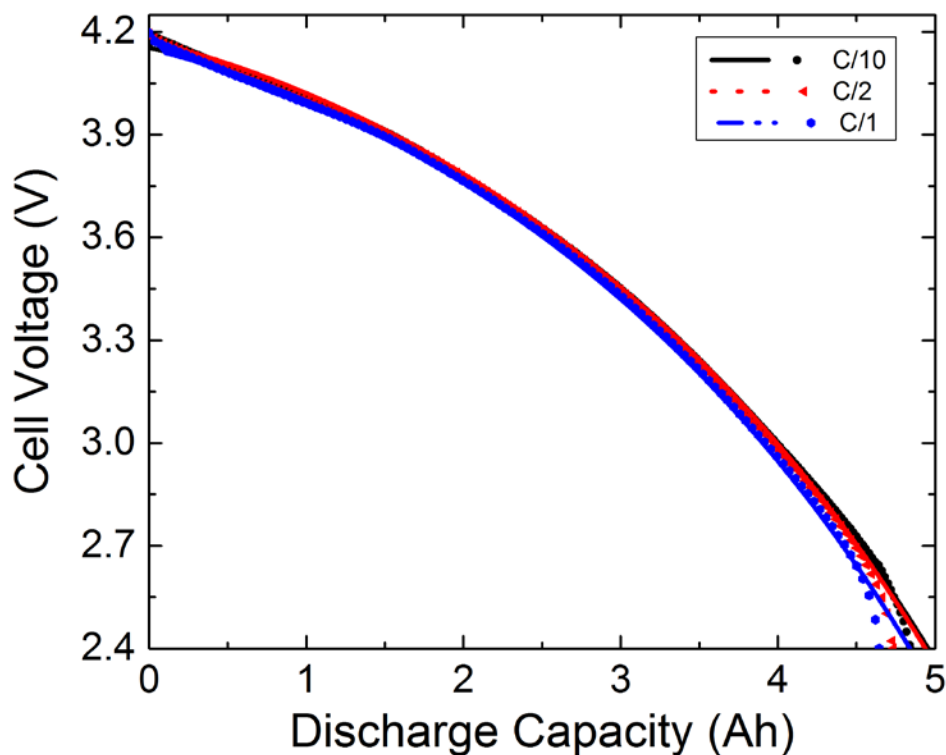

Figure 6-4. Comparison of simulated discharge from the model with experimental results at different rates.

The growth of the SEI porous layer is assumed to follow the model developed by Ploehn *et al.*, where growth is limited by diffusion of the solvent. As discussed in the previous section, SEI growth in the negative electrode was assumed as the only source of

degradation. The predicted growth of the SEI on the negative electrode at 25 °C with time

is shown in **Figure 6-5**. Properties of the SEI vary from one system to another and it can

be difficult to analyze the SEI quantitatively. Hence, we rely on previous studies to get

parameters of the SEI and assume values based on the ranges used in literature for various

SEI compounds [12, 14, 15]. The amount of lithium lost in the SEI increases with

increasing thickness as presented in **Equation 6-9**. This relationship of increased lithium

loss with increasing SEI thickness is shown in **Figure 6-5**.
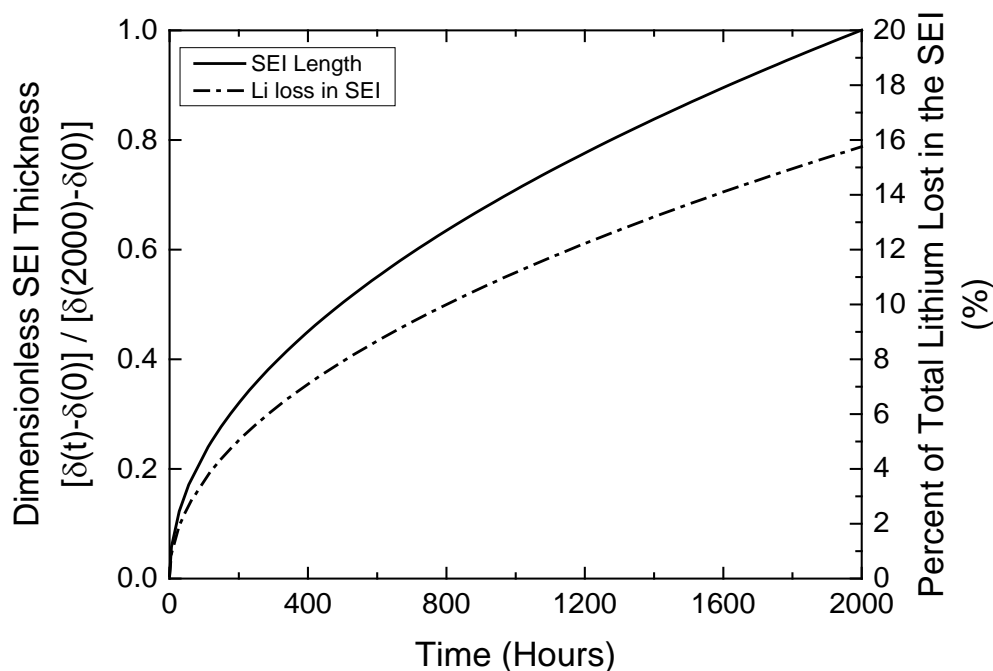

Figure 6-5. SEI growth over time limited by solvent diffusion. Lithium loss in the SEI is also shown.

In **Chapter 5**, we reported and discussed capacity fade of EH4 cell stored at 75 °C.

By assuming the cell degradation to occur via lithium loss mechanism in the SEI, we are

able to estimate lithium loss as presented in **Figure 6-5**. Simulated results are represented

by open markers and experimental data are represented by solid markers. In order to evaluate cell capacity, discharge simulations were run for a fully charged cell at different values of lithium loss. Simulated cell capacity for EH4 cell at different times during high temperature aging is shown in **Figure 6-6**. Cell capacity was measured at a rate of 1C by discharging the cells from 4.2 V to 2.4 V. All other parameters were kept constant besides the amount of reversible Li loss in the cell. Comparison with experimental data for capacity fade in EH4 cell is also presented.

Simulated cell capacity follows a linear trend with square root of time, which is expected based on the parabolic SEI growth mechanism. In the experimental study conducted in **Chapter 5**, we were able to identify SEI growth and lithium loss as the main degradation mechanism in the cell during the first 2000 hours of aging. By incorporating SEI growth and lithium loss into our model, we are able to simulate capacity fade and compare simulation results with experimental data. Close agreement of simulation results with experimental data provides further evidence to support the conclusions made in **Chapter 5** about cell degradation due to SEI growth and lithium loss mechanism. As the experimental results suggest, most of the lithium loss may be attributable to the growth of the SEI on the negative electrode. These results support our conclusion that lithium loss is the major factor for capacity fade observed in EH4 cells.
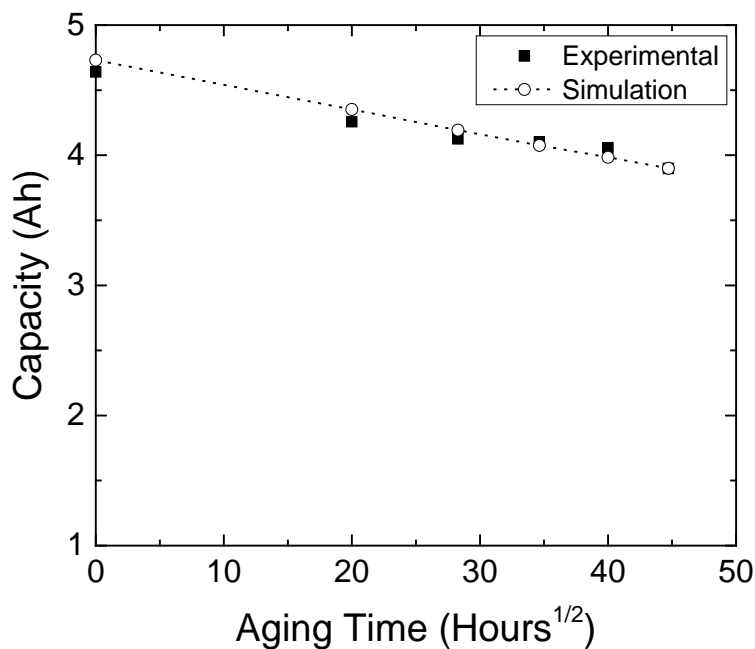
Figure 6-6. Cell capacity due to irreversible lithium loss in the SEI in the negative electrode. Simulations were run at 1C from 4.2V to 2.4 V.

The concept of cell resistance was described in previous chapters. In summary, when current is flowing in a cell, the resulting voltage depends on the open-circuit potential of the electrodes and the ohmic losses as well as polarizations in the cell. As measured with these pulse power tests, the cell resistance is a measure of the ohmic losses as well as the kinetic and mass transfer polarizations in the cell. **Figure 6-7** shows the voltage response of EH4 cell during discharge at different C-rates. Discharge currents at different rates were applied for 30 s to a cell at rest. After 30 s discharge, charge current was applied at C/10 to recharge the cell. The cell voltage deviates increasingly from the open-circuit voltage at higher currents. Large concentration polarizations present in the cell is evident at high discharge rates.
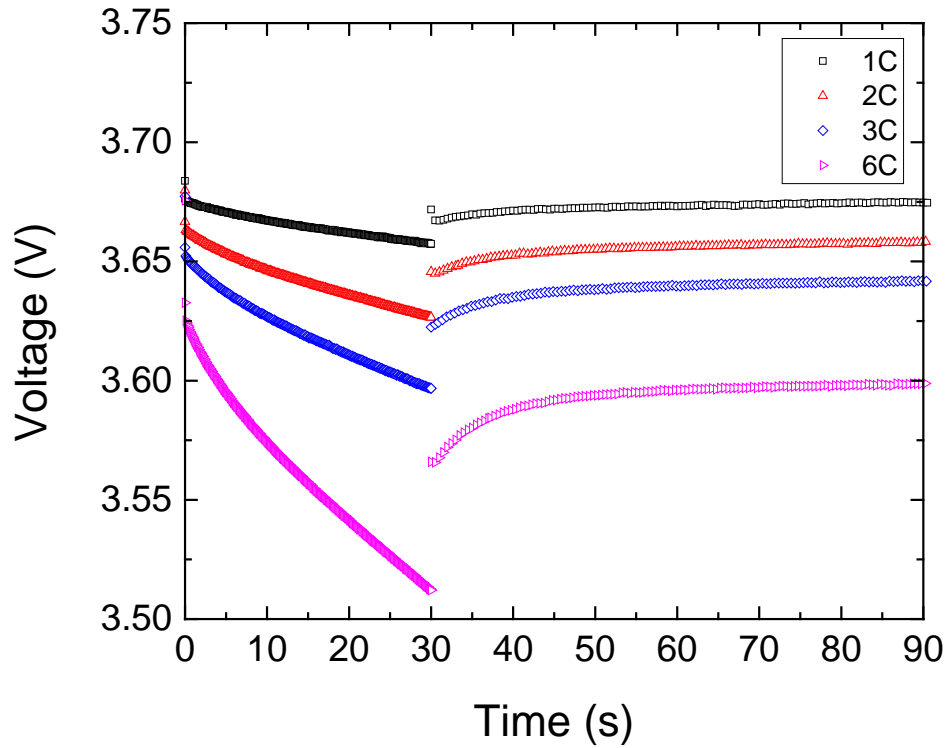
Figure 6-7. The voltage response of a cell during discharge at different C-rates. Discharge was carried out for 30 s at different rates. After 30 s discharge, cell was recharged at C/10.

Simulated discharge and charge resistances as a function of aging time of the cell at 3.7 V are shown in **Figure 6-8**. The increase in discharge resistance for the most degraded case compared to un-degraded case is around 32 %. Similarly, the increase in charge resistance from the un-degraded to most degraded case after 2000 hours is 27 %. The discharge resistance is greater than the charge resistance as shown in **Figure 6-8**. In our experimental results, we found the discharge resistance to be greater than the charge resistance as well. The charge-delivery and charge-acceptance characteristics of batteries are determined by the thermodynamic properties of the electrodes and vary with SOC. The large difference between the charge and discharge resistance of the cell is likely due to the

current profile used in the HPPC test. High current used to discharge the cell in the beginning of the HPPC profile results in over 12 % change in the SOC of the cell. As a result, even though the test starts at around 50 % SOC, the SOC of the cell before the application of the charge pulse is significantly lower. Apart from this, the kinetics for charge-delivery and charge-acceptance are different. The charge resistance of the cell is thus different than the discharge resistance.

The model captures the trend seen in the experimental cell for charge and discharge resistance and the increase in cell resistance with aging. Simulation results are most sensitive to the radius of the active materials and the solid phase diffusivities of lithium. The radii of the active materials were determined by taking scanning electron microscopy (SEM) images and an average was used as a constant radius for the electrode particles. The diffusivities of lithium in the solid phase were adjusted to fit the discharge behavior of the experimental cell at low rates. The values of diffusivities used are similar to those available in the literature [16, 17]. It may be useful to identify these parameters experimentally, including the dependence of the lithium diffusivity on the extent of lithiation or delithiation.

Pulse power capability simulated for charge and discharge at 3.7 V are shown in **Figure 6-9** with increasing aging time. Cell resistance and power capability were determined by using the maximum pulse currents for which the discharge limits for the cell were satisfied, as described earlier. Cell resistance and power capability decrease linearly with square root of time similar to the capacity fade. The same lithium loss mechanism is responsible for capacity and power fade and the cell performance deterioration is similar with increasing aging time. The loss of power capability for discharge and charge for

degraded condition after 2000 hours aging are 25 % and 15 %, respectively. Cell resistance during discharge increases at a greater rate and power capability during discharge decreases at a greater rate compared to charge with increasing aging time. In HPPC profile, the charge current is lower compared to the discharge current. Similarly, discharge pulse is applied before the charge pulse with the cell at 50 % SOC, whereas the charge pulse is applied when the cell is at a lower SOC because of resulting discharge from the discharge pulse. Cell overpotentials and transport limitations are greater during the discharge process as higher current is used.
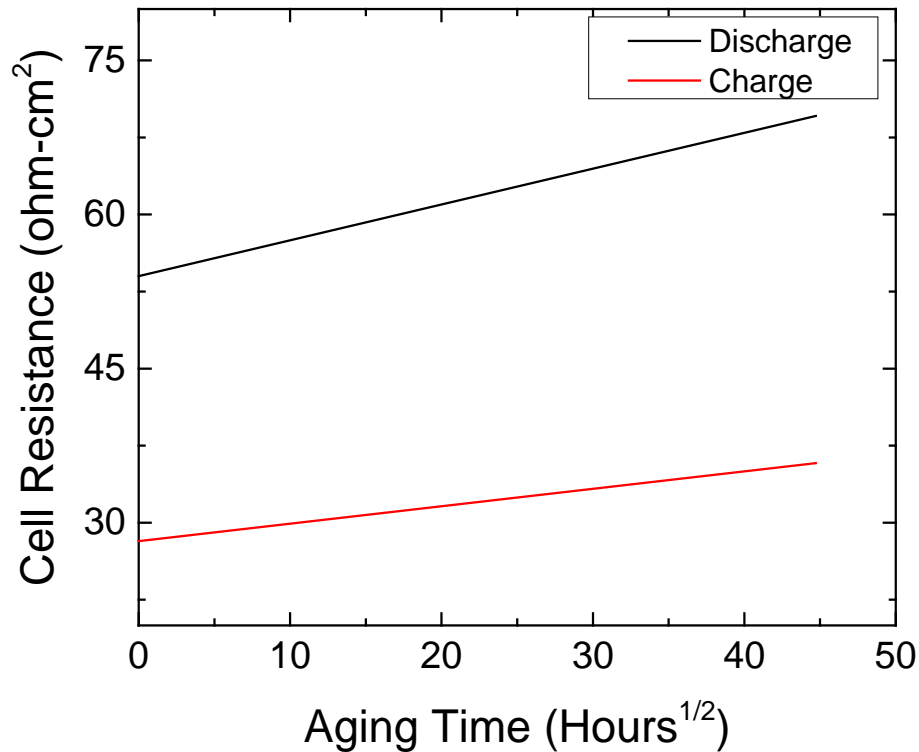

Figure 6-8. Simulated charge and discharge cell resistance increase due to reversible lithium loss in the SEI in the negative electrode. 10 s discharge and charge pulses were simulated at 3.7 V.
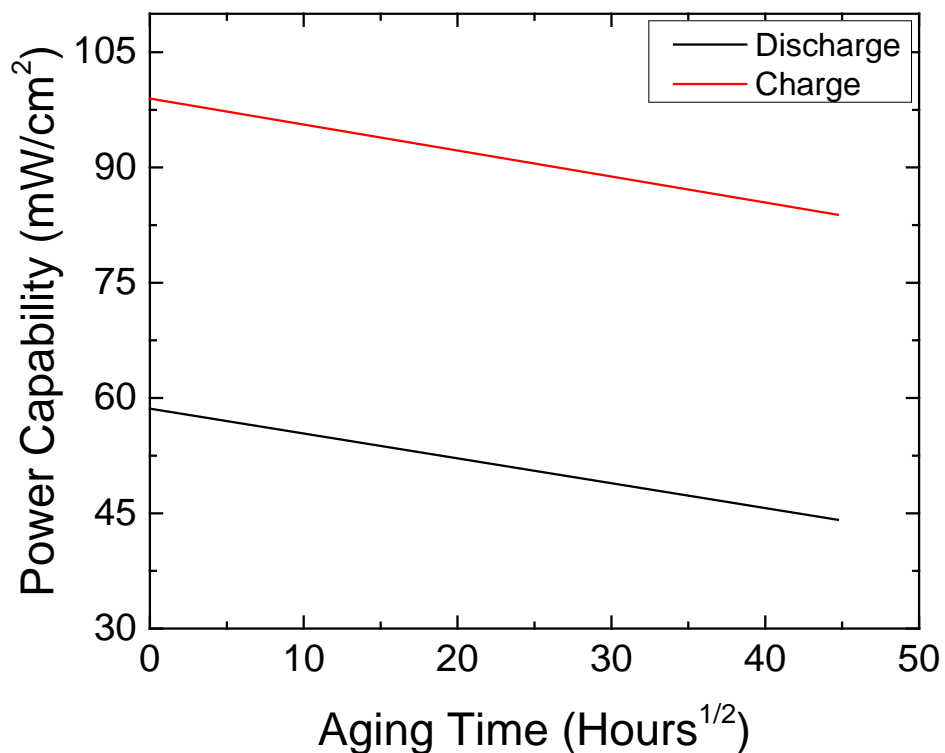
Figure 6-9. Simulated power capability of cell for charge and discharge at different amounts of lithium loss in the SEI.

Negative effects of the role of cyclable lithium loss in the SEI on cell resistance and power capability is clear from **Figures 6-8** and **6-9**. The only degradation mechanism considered in the model was the cyclable lithium loss in the SEI which contributed to the decrease in cell performance with increasing aging time. The ohmic resistance in the cell with increasing aging time is shown in **Figure 6-10**. Ohmic resistance was estimated by using the change in cell potential after the application of pulse current ($\Delta V/\Delta I$) for the cell

143

following a rest period. Data were taken every 100 ms, so the ohmic resistance thus measured also includes some kinetic polarizations in the cell. The ohmic resistance for charge was found to be greater than that for discharge, suggesting that the kinetics for insertion and de-insertion are different. In HPPC tests, the discharge is carried out initially for the cell at equilibrium. A charge pulse is applied after a rest period of 40 s following discharge. The SOC of the cell is different compared to before discharge step. Additionally, the rest period may not be sufficient for the cell to equilibrate before the application of charge pulse. The cell is polarized and at a different SOC before the charge step. Thus, ohmic resistance measured for the cell for charge is different than that for discharge. The contribution of the ohmic resistance to the total cell resistance in **Figure 6-8** is less than 7 % in all cases during aging for charge and discharge. Thus, ohmic losses in the cell do not contribute significantly to the performance loss. Most significant contribution to the cell resistance increase and power capability decrease in the cell is due to increase in losses related to mass transfer.
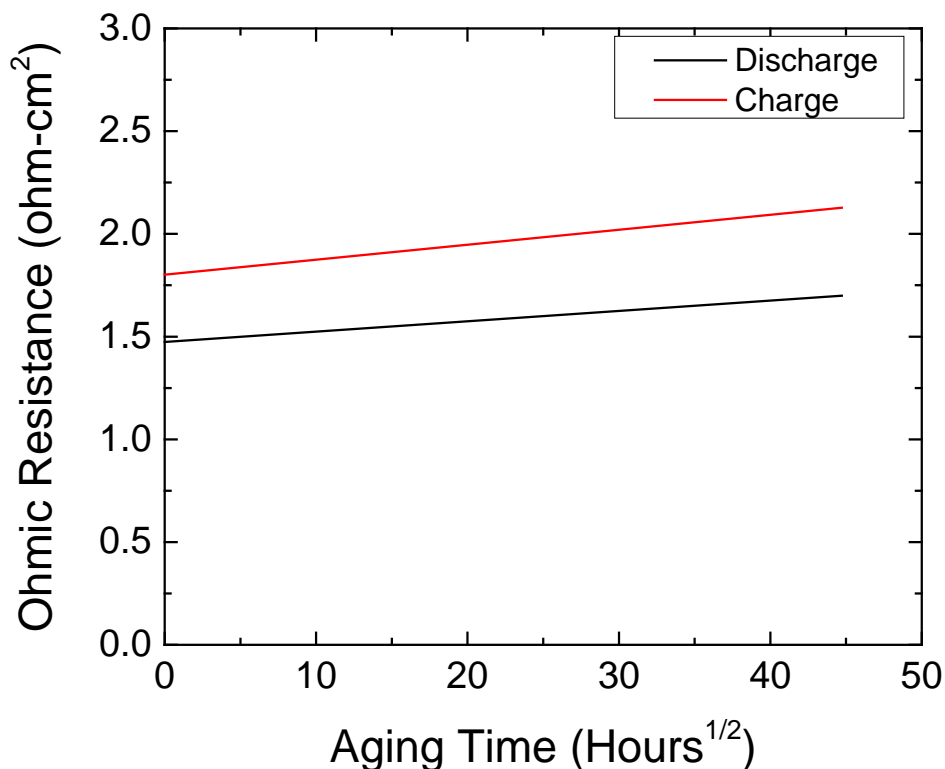
Figure 6-10. Simulated increase in ohmic resistance in the cell with increasing aging time.

We recognized that the contributions to cell resistance from ohmic resistance are not significant. We observed similar behavior from the resistance analysis of the experimental cell. The ohmic resistance also includes kinetic polarizations as described previously. Thus, concentration polarizations are primarily responsible for cell resistance. Concentration polarizations may occur due to limitations occurring in the solution phase or in the solid phase. Different factors including the salt diffusion coefficient, transference number, porosity, and tortuosity affect the lithium concentration in the solution phase. Lithium concentration in the solution phase varies with time and position along the length

of the cell during passage of current. The lithium concentration in the solution phase during

the discharge portion of the HPPC test is shown in **Figure 6-11** for a fresh cell. As

discharge time increases, concentration gradients develop in the cell. The solution phase

concentration during the same discharge for the aged cell did not show any change

compared to the fresh cell. The concentration polarization is the electrolyte phase thus

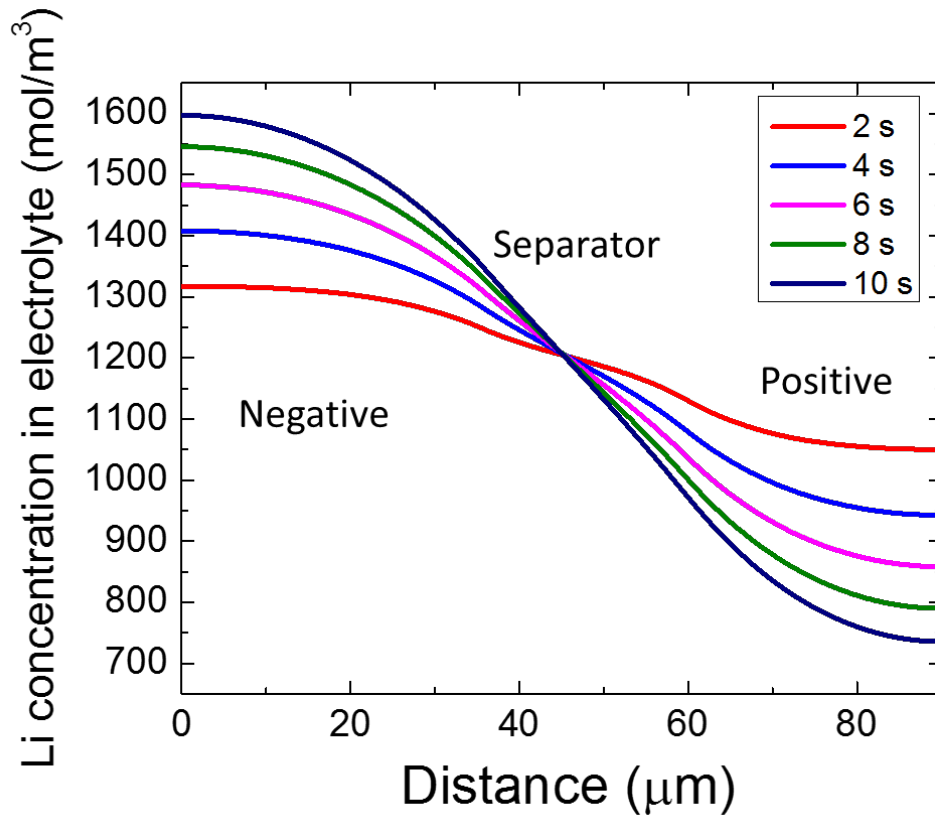remains unchanged between the fresh and aged cell.

Figure 6-11. Lithium concentration profiles across the cell at various times during the
pulse discharge during HPPC test.

The time constant for diffusion of lithium in the solid phase in the spherical active

material particle is 900 s for the positive electrode based on the parameters used in the

model. The ideal discharge time for a complete discharge at 4C rate is 900 s. Thus, solid phase diffusion limitations exist in the positive electrode at rates higher than 4C. The time constant for diffusion of lithium in the negative electrode particle is 6.5 times than that for the positive electrode and therefore the diffusion limitations are greater in the negative electrode. Because of these limitations, solid phase lithium concentration at the surface of the active material particle is different compared to the concentration at center of the particle. The average concentration of lithium in the solid phase at the surface of the active material particle is shown in **Figure 6-12** for the aged cell with the largest degradation. This concentration is the average of the concentrations at the surface of the active material particle along the length of the electrode. For the negative electrode, the average concentration at the surface approaches zero at the end of the discharge. The concentration at the center of the electrode remains essentially unchanged during the discharge period. Diffusion limitations, primarily in the negative electrode, lead to lithium depletion at the surface of the electrode and contribute to large concentration polarizations.
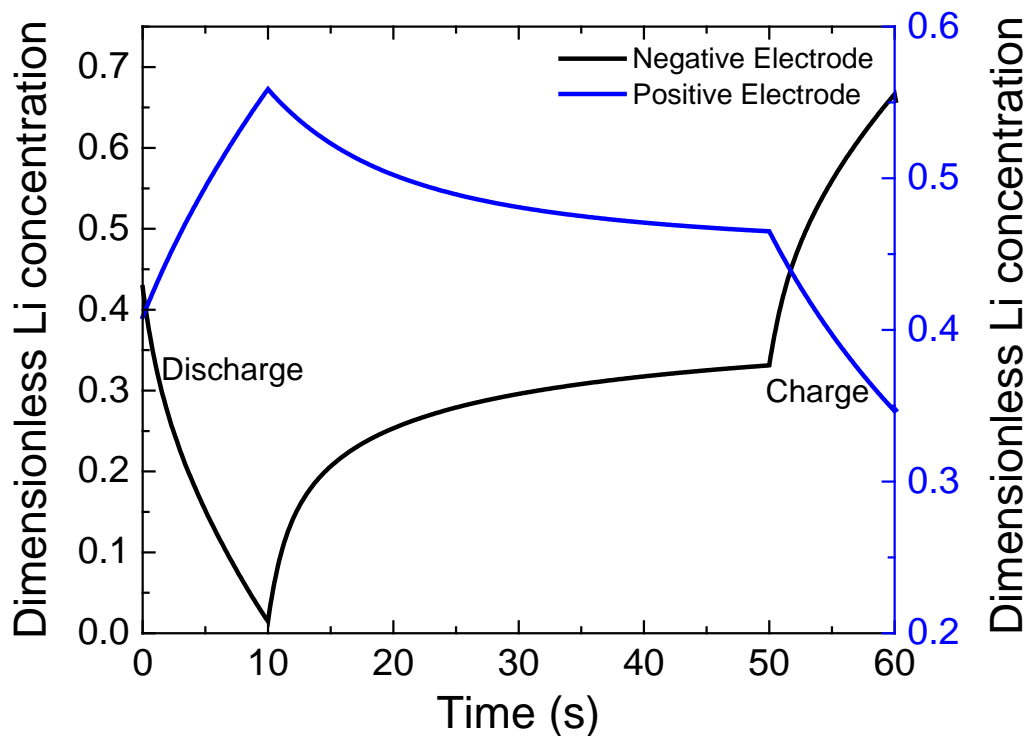
Figure 6-12. Average dimensionless lithium concentration in the solid phase at the surface of the particle of active material with increasing time during HPPS test for the aged cell with greatest amount of degradation.

Degradation due to lithium loss in the SEI is marked by the loss of cyclable lithium in the cell, which is lost to form the SEI. If the cell potential (positive minus negative) is held constant, the concentrations of lithium in each electrode will decrease as a result of irreversible lithium loss. Decreasing lithium concentrations in each electrode at charged state (V_{cell}=4.2 V) with increased lithium loss is shown in **Figure 6-13**. Similarly, at a fixed cell potential of 3.7 V—the potential at which cell resistance is measured, as irreversible lithium loss in the cell increases, less lithium is available in each electrode. The lost lithium in the cell due to degradation caused by the SEI decreases cell capacity and power

capability. The reaction rate at the surface of the electrodes may be affected when the concentration of lithium at the surfaces decreases. The thermodynamic open-circuit potential of the electrodes as well as the exchange-current density for the charge-transfer reaction at the electrode-electrolyte interface depend on the lithium concentration at the electrode surface. Limitations in mass transfer can lead to large cell overpotentials and contribute to cell performance losses.
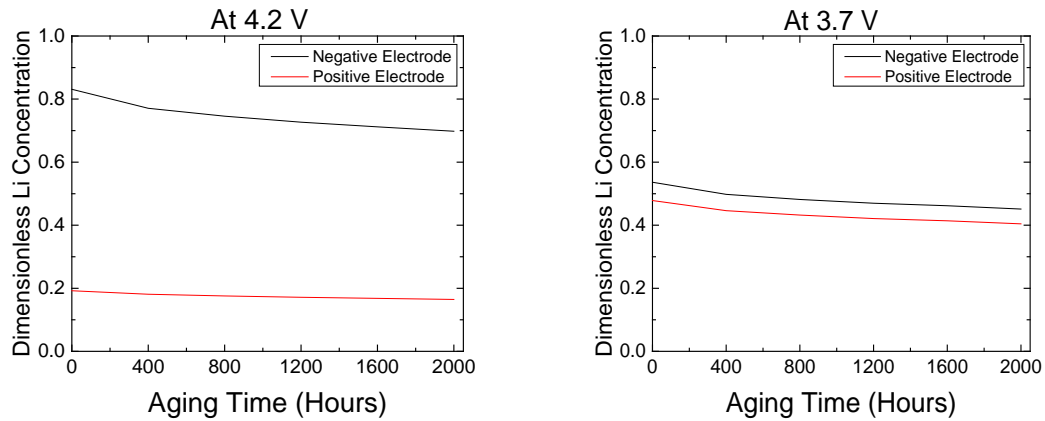
Figure 6-13. Loss of dimensionless lithium concentration (*x* and *y* for negative and positive electrodes, respectively) in each electrode as a result of increasing lithium loss in the SEI. Lithium concentrations in positive and negative electrodes at 4.2 V and 3.7 V are shown.

Lithium loss in the cell due to the growth of the SEI was the only degradation mode considered in this section. As we noticed, cell capacity and power were affected adversely by increasing lithium loss. In addition, lithium loss had a greater impact on cell resistance and power capability compared to the discharge capacity of the cell. SEI growth limits performance in lithium-ion batteries via other mechanisms in addition to the reversible lithium loss in SEI. Growth of the SEI also affects cell capacity and power via means of

increased resistance and potential drop across the SEI [14, 18]. Increase in cell resistance and decrease in pulse power capability is further magnified if we include the effect of increased potential drop across thicker SEI. Increased resistance of the SEI leads to power fade as well as incomplete charge and discharge of the cell, which diminishes cell capacity [19]. Thus, SEI growth has a much more severe effect on capacity fade and power fade due to losses occurring as a result of reversible lithium loss and increased resistance.

6.4 Conclusions

It is essential to maintain cyclable lithium inventory in the cell for the useful duration of the cell in order to maintain performance goals for capacity as well as power. In this work, we have shown that loss of cyclable lithium has a major effect on power fade. Cell resistance increases with reversible lithium loss in the SEI. Power capability predictions are likely to be inaccurate if lithium loss in the SEI is not included in power fade models. Similarly, contributions of other cell degradation modes to cell resistance may inadvertently be magnified by ignoring the contribution due to cyclable lithium loss in the SEI. It is essential to monitor the SOC of the batteries accurately in order to prevent overcharge and over-discharge conditions for HEV applications. Power demands are high for HEV applications and any loss mechanism must be well-understood and incorporated into prediction models used for the battery management systems (BMS) to ensure that the batteries stay within the desired voltage range while meeting the high power needs. This loss mechanism must be accounted while evaluating the power capability of batteries for long-term applications accurately.

6.5 References

1. INEEL, *FreedomCAR Battery Test Manual for Power-Assist Hybrid Electric Vechicles*. 2003, Prepared for the U.S. Department of Energy.

2. Liaw, B.Y., et al., *Correlation of Arrhenius behaviors in power and capacity fades with cell impedance and heat generation in cylindrical lithium-ion cells.* Journal of Power Sources, 2003. **119**: p. 874-886.

3. Arora, P., R.E. White, and M. Doyle, *Capacity fade mechanisms and side reactions in lithium-ion batteries.* Journal of the Electrochemical Society, 1998. **145**(10): p. 3647-3667.

4. Zhang, Y., C.-Y. Wang, and X. Tang, *Cycling degradation of an automotive LiFePO4 lithium-ion battery.* Journal of Power Sources, 2011. **196**(3): p. 1513-1520.

5. Fuller, T.F., M. Doyle, and J. Newman, *Simulation and Optimization of the Dual Lithium Ion Insertion Cell.* Journal of the Electrochemical Society, 1994. **141**(1): p. 1-10.

6. Fuller, T.F., M. Doyle, and J. Newman, *Relaxation Phenomena in Lithium-Ion-Insertion Cells.* Journal of the Electrochemical Society, 1994. **141**(4): p. 982-990.

7. Doyle, M., T.F. Fuller, and J. Newman, *Modeling of Galvanostatic Charge and Discharge of the Lithium Polymer Insertion Cell.* Journal of the Electrochemical Society, 1993. **140**(6): p. 1526-1533.

8. Aurbach, D., et al., *The Study of Electrolyte Solutions Based on Ethylene and Diethyl Carbonates for Rechargeable Li Batteries: II . Graphite Electrodes.* Journal of The Electrochemical Society, 1995. **142**(9): p. 2882-2890.

9. Tang, M., S.D. Lu, and J. Newman, *Experimental and Theoretical Investigation of Solid-Electrolyte-Interphase Formation Mechanisms on Glassy Carbon.* Journal of the Electrochemical Society, 2012. **159**(11): p. A1775-A1785.

10. Verma, P., P. Maire, and P. Novak, *A review of the features and analyses of the solid electrolyte interphase in Li-ion batteries.* Electrochimica Acta, 2010. **55**(22): p. 6332-6341.

11. Tang, M. and J. Newman, *Transient Characterization of Solid-Electrolyte-Interphase Using Ferrocene.* Journal of The Electrochemical Society, 2012. **159**(3): p. A281-A289.

12. Ploehn, H.J., P. Ramadass, and R.E. White, *Solvent diffusion model for aging of lithium-ion battery cells.* Journal of the Electrochemical Society, 2004. **151**(3): p. A456-A462.

13. Joshi, T., et al., *Effects of Dissolved Transition Metals on the Electrochemical Performance and SEI Growth in Lithium-Ion Batteries.* Journal of the Electrochemical Society, 2014. **161**(12): p. A1915-A1921.

14. Safari, M., et al., *Multimodal Physics-Based Aging Model for Life Prediction of Li-Ion Batteries.* Journal of the Electrochemical Society, 2009. **156**(3): p. A145-A153.

15. Ramadass, P., et al., *Development of first principles capacity fade model for Li-ion cells.* Journal of the Electrochemical Society, 2004. **151**(2): p. A196-A203.

16. Stewart, S.G., V. Srinivasan, and J. Newman, *Modeling the performance of lithium-ion batteries and capacitors during hybrid-electric-vehicle operation.* Journal of the Electrochemical Society, 2008. **155**(9): p. A664-A671.

17. Chandrasekaran, R., *Quantification of contributions to the cell overpotential during galvanostatic discharge of a lithium-ion cell.* Journal of Power Sources, 2014. **262**: p. 501-513.

18. Christensen, J. and J. Newman, *A mathematical model for the lithium-ion negative electrode solid electrolyte interphase.* Journal of the Electrochemical Society, 2004. **151**(11): p. A1977-A1988.

19. Christensen, J. and J. Newman, *Effect of anode film resistance on the charge/discharge capacity of a lithium-ion battery.* Journal of the Electrochemical Society, 2003. **150**(11): p. A1416-A1420.

CHAPTER 7

SUMMARY AND RECOMMENDATIONS

In this dissertation, we combined experimental and modeling techniques to study degradation mechanisms in lithium-ion batteries. We observed that transition metal dissolution accelerates the growth of the solid electrolyte interphase (SEI) on the negative electrode. We identified SEI growth and lithium loss in the SEI to be the main factors leading to capacity and power fade in high power commercial lithium-ion cells. By using modeling techniques, we investigated the effects of lithium loss in the SEI and determined the capacity and power fade caused by lithium loss.

In **Chapter 4**, accelerated testing was employed in lab-made coin cells in order to obtain a better understanding of the role of the transition metals in the electrolytes on cell capacity and cyclability. Reduction of transition metals on the negative electrode resulted in increased thickness and resistance of the SEI. Cell capacity and cyclability were decreased due to transition metals in the electrolyte. A mechanism for SEI growth due to transition metals in the electrolyte was presented.

We observed noise in the capacity fade data in our study. The cells were tested at room temperature where fluctuations in temperature may be responsible for the noise the cell performance. It is recommended that cell testing be carried out in a temperature chamber to reduce variability caused by changes in ambient temperature. 30 mM concentration of transition metal salts used in the experiments in **Chapter 4** represented a highly degraded condition. Future work should focus on identifying the relationship between transition metal concentration and capacity fade by using a set of different

concentrations of transition metal salts. Furthermore, in our study we used all constituent transition metals (Ni, Co, and Mn) in the same concentration. It is possible that the influence of each dissolved metal species is variable in practical full cells. A more complete study can be conducted in the future in order to identify the contribution of each transition metal species on SEI growth and capacity fade.

In **Chapter 5**, we studied degradation in commercial cells used in high-power applications where accelerated degradation was achieved by high temperature aging at 75 °C. We found that cell resistance increase and capacity fade is mainly caused by the limitations occurring in the negative electrode in the beginning stages of aging. SEI growth in the negative electrode led to loss of cyclable lithium in the cell resulting in cell capacity fade and resistance increase. In the latter stages of aging, active material dissolution and surface layer formation on the positive electrode dominated the cell performance deterioration.

We recommend extending the aging degradation in this study by incorporating cycling profile along with high temperature aging. FreedomCAR battery test manual has defined cycling profile for charge-sustaining hybrids [1]. Including such a cycling profile in degradation study will help make a better idea about cell performance decline while operating cell in realistic cycling condition intended for hybrid applications. Although high temperature accelerated degradation is beneficial in reducing experimental time needed for such studies, the 75 °C temperature used in our study is extremely high when compared to normal cell operating conditions. It is important to extend this study to lower temperatures and add cycling profile as well to assess the capacity and power fade in these cells occurring at conditions similar to their intended applications.

A physics-based model of a lithium-ion cell containing a graphite composite electrode and an NCM composite electrode was developed in **Chapter 6** to study the capacity and power fade due to lithium loss caused by the SEI growth. Modeling results were compared with experimental data at various discharge rates. SEI growth and corresponding lithium loss were evaluated for the cell as aging time increased. Capacity fade simulations were performed at different times as aging proceeded and results were compared to the experimental capacity fade data. Cell resistance and power capability were evaluated by using the high performance power characterization (HPPC) testing protocol [1]. Irreversible loss of cyclable lithium loss in the SEI contributed significantly to diminished cell capacity and power capability.

High rate pulse currents up to 23C were used in simulation studies for HPPC tests. It was not possible to experimentally carry out these tests requiring high currents due to current limitations of our laboratory battery cycler. Simulation results at high rates of charge and discharge can be compared to experimental data at those rates to improve the fidelity of the model. We used a constant value for the ionic conductivity of the electrolyte measured at a constant concentration. It is recommended that the ionic conductivity be measured at different salt concentrations to obtain an accurate relationship between salt concentration and ionic conductivity to use in the model. In our model, parameters such as solid phase diffusion coefficient of lithium in both electrodes and the kinetic parameters for charge transfer reaction were adjusted to fit the experimental data. In future work, it is recommended to experimentally determine these parameters in order to study the influence of these parameters on cell performance.

7.1 References

1. INEEL, *FreedomCAR Battery Test Manual for Power-Assist Hybrid Electric Vechicles*. 2003, Prepared for the U.S. Department of Energy.

APPENDIX A

EQUILIBRUIM POTENTIAL DATA

Open Circuit Potential Data for Insertion Materials

Open-circuit potential for graphite electrode is given by

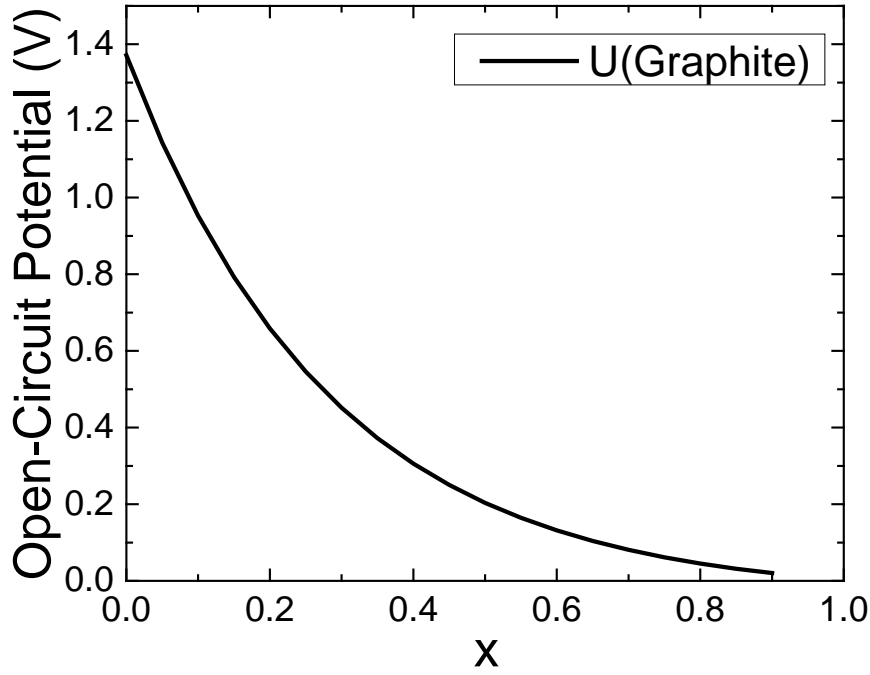$$U = -0.176 + 1.588\exp(-3.357x) \qquad \text{[A-1]}$$

Figure A- 1. The open-circuit potential of graphite as a function of Li concentration.

For the NCM electrode, the open-circuit potential is given by

$$U = 4.59 - 2.07y + 1.2y^2 - 6.77 \cdot 10^{-26} \cdot e^{(58.19y)} \qquad \text{[A-2]}$$
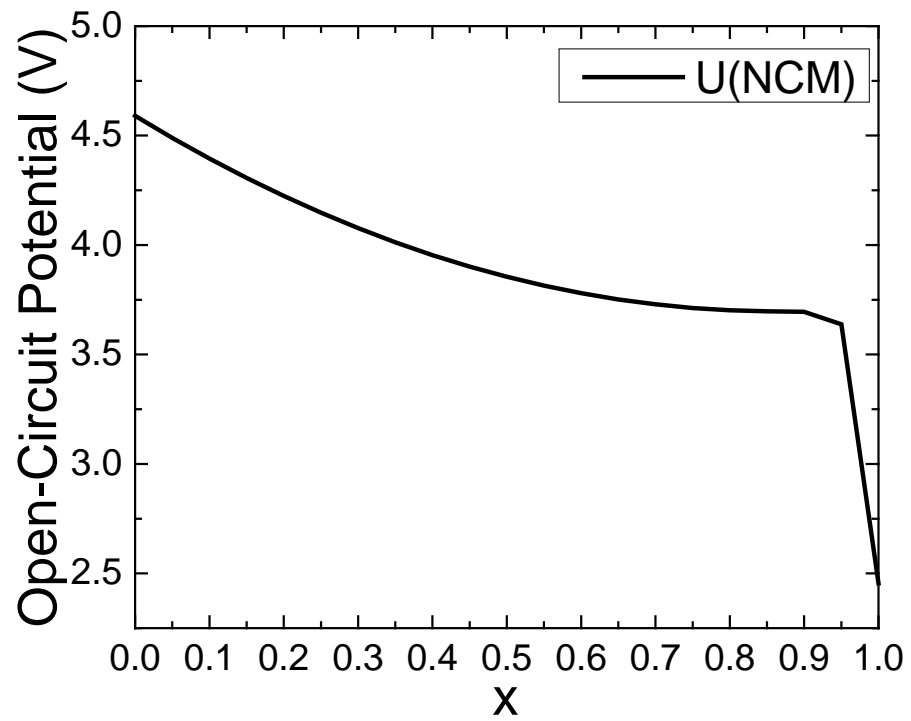
Figure A- 2. The open-circuit potential of NCM as a function of Li concentration.

APPENDIX B

GOVERNING EQUATIONS

GOVERNING EQUATIONS

The electrodes are assumed to consist of identical spherical particles with a fixed radius. The transport of lithium ions within the particles is given by Fick's law.

$$\frac{\partial c_s}{\partial t} = \frac{1}{r^2}\frac{\partial}{\partial r}\left(r^2\left(D_s\frac{\partial c_s}{\partial r}\right)\right) \tag{B-1}$$

where c_s is the concentration of lithium in the solid phase. All variables used are described in the list of variables. The first boundary condition for above equation is derived from symmetry

$$\frac{\partial c_s}{\partial r} = 0 \quad \text{at r} = 0, \tag{B-2}$$

and the second boundary condition is obtained by relating the rate of diffusion of lithium into the electrode and the pore-wall flux across the interface.

$$j_n = -D_s\frac{\partial c_s}{\partial r} \quad \text{at r} = R_s. \tag{B-3}$$

The material balance on the solution phase for this system is given by

$$\varepsilon\frac{\partial c}{\partial t} = \nabla\cdot(D_{eff}\nabla c) - \frac{i_2\cdot\nabla t_+^0}{F} + aj_n(1-t_+^0) \tag{B-4}$$

where c is the concentration of the electrolyte and ε is the volume fraction of the electrolyte phase. We use constant porosities and transference number (t_+^0) in this work. The specific interfacial area (a) for spherical particles is

$$a = 3\frac{(1-\varepsilon)}{R_s} \qquad \text{[B-5]}$$

Using Faraday's law, we can relate the pore-wall flux across the interface between the electrolyte and the active material, j_n, and the divergence of the current flow in the electrolyte phase

$$aj_n = -\frac{as_i}{nF}i_n = -\frac{s_i}{nF}\nabla \cdot i_2 \qquad \text{[B-6]}$$

The total superficial current density (I) flows either through the solution phase (i_2) or through the matrix phase of the composite electrodes (i_1), and is conserved.

$$I = i_1 + i_2 \qquad \text{[B-7]}$$

The current flowing in the solid matrix phase is governed by Ohm's law.

$$i_1 = -\sigma_{eff}\nabla\phi_1 \qquad \text{[B-8]}$$

and the variation of potential in the solution phase is given by

$$i_2 = -\kappa_{eff}\nabla\phi_2 + \frac{2\kappa_{eff}RT}{F}\left(1 + \frac{\partial \ln f_A}{\partial \ln c}\right)(1 - t_+^0)\nabla \ln c \qquad \text{[B-9]}$$

The solution phase potential (Φ_2) is measured with a lithium reference electrode in solution. We did not incorporate non-ideality in the electrolyte, and hence, the salt activity coefficient (f_A) is taken as 1.

The effective transport properties must be used in case of porous media to account for the actual path length of transport and the reduced area for transport. These modified transport properties used in this study are

$$D_{eff} = D\varepsilon^{0.5} \qquad\qquad\qquad \text{[B-10]}$$

$$\sigma_{eff} = \sigma(1-\varepsilon)^{1.5} \qquad\qquad\qquad \text{[B-11]}$$

$$\kappa_{eff} = \kappa\varepsilon^{1.5} \qquad\qquad\qquad \text{[B-12]}$$

The flux density of each species must be zero at the ends of the cell. This gives the boundary conditions required for Eq. 4.

$$\nabla c = 0 \quad \text{at x = 0 and x = L.} \qquad\qquad\qquad \text{[B-13]}$$

At the two boundaries of the cell, the solution current is zero. Hence, the above boundary conditions also give boundary conditions required for Eq. 8 and 9.

$$\nabla\phi_1 = -I/\sigma_{eff} \quad \text{at x = 0 and x = L} \qquad\qquad\qquad \text{[B-14]}$$

$$\nabla\phi_2 = 0 \quad \text{at x = 0 and x = L} \qquad\qquad\qquad \text{[B-15]}$$

Since we are only concerned about the potential differences, we arbitrarily fix the solid phase potential at the current collector/negative electrode boundary to zero.

The insertion/deinsertion in the active material follows Butler-Volmer kinetics. The charge transfer process occurring across the electrolyte/electrode interface is represented by

$$Li^+ + e^- + \theta \Leftrightarrow Li - \theta \qquad \text{[B-16]}$$

where θ represents an active site in the solid insertion electrodes. The related expression for Butler-Volmer kinetics is

$$i_{int} = kFc^{\alpha_a}(c_{max} - c_s)^{\alpha_a} c_s^{\alpha_c} \left\{ \exp\left(\frac{\alpha_a F\eta}{RT}\right) - \exp\left(\frac{\alpha_c F\eta}{RT}\right) \right\} \qquad \text{[B-17]}$$

In above expression, k is the net reaction rate constant and the overpotential (η) is defined as

$$\eta = \phi_1 - \phi_2 - U - \phi_{SEI} \qquad \text{[B-18]}$$